



POLITECNICO
MILANO 1863

Department of Aerospace Science and Technology
Launch Systems
Academic Year 2024/2025

Conceptual design of an airborne space launcher with first stage reusability



Team: Make It More Pointy

Person Code	Surname	Name	E-mail
10704425	Bianchini	Giulia	giulia1.bianchini@mail.polimi.it
10796659	Ceglie	Francesco	francesco.ceglie@mail.polimi.it
11012590	De Carli	Matteo	matteo.decarli@mail.polimi.it
10618489	Mapelli	Michele	michele2.mapelli@mail.polimi.it
10723157	Paniz	Alberto	alberto.paniz@mail.polimi.it
10722865	Piemonte	Francesco	francescoantonio.piemonte@mail.polimi.it
10765924	Piraccini	Mattia	mattia1.piraccini@mail.polimi.it
10766648	Portantiolo	Matteo	matteo.portantiolo@mail.polimi.it
10730703	Proserpio	Andrea	andrea2.proserpio@mail.polimi.it

Abstract

This report presents the conceptual design of an airborne space launcher aimed at deploying payloads into Low Earth Orbit (LEO). The study focuses on innovative solutions to enhance the recovery and reusability of the launch vehicle first stage, addressing critical challenges in cost reduction, operational efficiency, and environmental sustainability.

The proposed system leverages an airborne platform to launch the rocket from a high-altitude, low-drag environment, minimizing fuel requirements and improving payload weight capacity. Particular attention is given to the design of the first stage, incorporating aerodynamic surfaces and descent mechanisms for safe recovery and refurbishment. Comparative analysis with traditional ground-based launch systems highlights significant potential in economic and performance metrics.

This work integrates multidisciplinary approaches, combining aerodynamics, propulsion, structural engineering, and systems integration, to propose a feasible and scalable solution for next-generation orbital launch systems. The findings contribute to ongoing efforts in commercial space exploration, emphasizing reusability as key drivers for future development.

Nomenclature

A				
α	Angle of attack	[deg]	δ	Thrust gimbal deflection angle [deg]
a	Speed of sound	[m/s]	δ_{LE}	Leading edge aperture angle [deg]
A_c	Chamber cross-sectional area	[m ²]	D	Drag [N]
A_f	Fairing surface area	[m ²]	d_c	Chamber Diameter [mm]
A_t	Throat cross-sectional area	[m ²]	d_{ds}	Shoulder downstream diameter [m]
A_b	Launcher base area	[m ²]	d_{par}	Parachute diameter [m]
A_{env}	Non pressurized structures surface area	[m ²]	d_{ref}	Reference diameter [m]
A_{fin}	Surface area of a single fin	[m ²]	d_t	Throat Diameter [mm]
A_{LOX}	LOX tanks surface area	[m ²]	d_{us}	Shoulder upstream diameter [m]
A_p	Launcher planar area	[m ²]	E	
A_{ref}	Launcher reference area	[m ²]	η	Cross flow drag proportionality factor [-]
A	Area	[m ²]	η_{drogue}	Drogue porosity [-]
AR	Wing aspect ratio	[$-$]	ε	Nozzle expansion ratio [-]
B			ε_{s1}	Structural index stage 1 [-]
β	Prandtl-Galwert compressibility factor	[$-$]	ε_{s2}	Structural index stage 2 [-]
b	Wing span	[m]	E	Young's Modulus [GPa]
b_T	Thrust lever arm	[m]	F	
b_{c_p}	Center of pressure lever arm	[m]	f	Darcy friction factor [-]
C			f	Fineness ratio ratio [-]
χ	Spherical angle	[rad]	G	
c^*	Characteristic Velocity	[m/s]	$\dot{\gamma}$	Flight path angle rate [deg /s]
C_A	Axial coefficient	[$-$]	γ	Flight path angle [deg]
C_a	Aerodynamic axial coefficient	[$-$]	g_0	Gravitational acceleration on Earth [$\frac{m}{s^2}$]
C_D	Drag coefficient	[$-$]	H	
C_f	Skin friction coefficient	[$-$]	h	Convective coefficient [W/(m ² ·K)]
c_g	Center of gravity position from nose	[m]	I	
C_L	Lift coefficient	[$-$]	I	Inertia matrix [kg· m ²]
c_m	Mean aerodynamic chord	[m]	I_{sp}	Specific impulse [s]
C_N	Normal coefficient	[$-$]	K	
C_n	Aerodynamic normal coefficient	[$-$]	k	Ratio of specific heats [-]
C_p	Pressure coefficient	[$-$]	K_p	cost factor [-]
c_p	Center of pressure position from nose	[m]	k_{th}	thermal coefficient [-]
D			L	
ΔT	Temperature difference	[K]	Λ_{LE}	Leading edge sweep angle [deg]
ΔV	Manoeuvre cost	[m/s]	L	Lift [N]
			l	Launcher body length [m]
			L^*	Characteristic Length [m]

M					
\dot{m}	Mass flow rate	[kg/s]	$Q_{hg,w}$	Heat flux from hot gas to the wall	[W/m ²]
μ	Dynamic viscosity	[Pa·s]	$Q_{w,c}$	Heat flux from the wall to the coolant	[W/m ²]
M	Mach number	[–]	R		
m	Mass	[kg]	ρ	Density	[kg/m ³]
m_1	First stage mass	[kg]	r	Recovery factor	[–]
m_2	Second stage mass	[kg]	R_n	Nose radius	[cm]
M_t	Torque	[Nm]	R_\oplus	Radius of the Earth	[km]
m_{01}	First stack mass	[kg]	Re	Reynolds number	[–]
m_{02}	Second stack mass	[kg]	S		
m_{p1}	First stage propellant mass	[kg]	σ	Bartz correction factor	[–]
m_{p2}	Second stage propellant mass	[kg]	σ_0	Stefan-Boltzmann constant	[W/(m ² K ⁴)]
m_{pay}	Payload mass	[kg]	σ_u	Ultimate Strength	[MPa]
M_{tot}	Total mass	[kg]	σ_y	Yield Strength	[MPa]
N			T		
ν	Poisson's ratio	[–]	T	Thrust	[N]
N_{eng}	Number of engines	[–]	t	Thickness	[mm]
N_{fins}	Fins normal aerodynamic force	[N]	T_w	Wall temperature at the hot-gas side	[K]
N_{nose}	Nose normal aerodynamic force	[N]	T_{0g}	Hot gas stagnation temperature	[K]
N_{skt}	Interstage skirt normal aerodynamic force	[N]	T_{aw}	Adiabatic wall temperature	[K]
Nu	Nusselt number	[–]	t_{double}	Time-to-double	[s]
O			t_{max}	Airfoil maximum thickness	[m]
ω	Bartz exponent parameter	[–]	T_{wg}	Hot side wall temperature	[K]
O/F	Oxidizer-to-Fuel ratio	[–]	TW_1	First stage thrust over weight	[–]
P			TW_2	Second stage thrust over weight	[–]
P	Power	[W]	V		
p	Pressure	[Pa]	V	Volume	[m ³]
P_c	Chamber Pressure	[bar]	v	Speed	[m/s]
p_{Hein}	Initial He pressure	[Pa]	v_c	Carrier velocity	[m ³]
Pr	Prandtl number	[–]	v_\oplus	Rotating velocity of the Earth	[m/s]
Q			v_{wind}	Wind speed	[m/s]
\dot{Q}	Heat flux	[W]	W		
\dot{Q}''	Heat flux per unit area	[W/m ²]	W	Weight	[N]
Q_w	Heat flux through the wall	[W/m ²]	X		
q_∞	Free-stream dynamic pressure	[kPa]	ξ_{const}	Reefing factor	[–]

Acronyms

2STO	Two Stage To Orbit	LEO	Low Earth Orbit
3STO	Three Stage To Orbit	LH₂	Liquid Hydrogen
AOA	Angle of Attack	LRR	Launch Readiness Review
AR	Aspect Ratio	LOX	Liquid Oxygen
BSM	Booster Separation Motor	LOX.St₁	Tank LOX stage 1
CEA	Chemical Equilibrium with Applications (software)	LOX.St₂	Tank LOX stage 1
CDR	Critical Design Review	MECO	Main Engine Cut-Off
COTS	Commercial Off-The-Shelf (products available for general purchase)	MER	Mass Estimation Relations
CTEs	Critical Technology Elements	ORR	Operational Readiness Review
DGB	Disk Gap Band	PDR	Preliminary Design Review
DOF	Degree of freedom	PRR	Preliminary Requirements Review
DRL	DownRange Landing	QR	Qualification Review
ECI	Earth Centred Inertial reference frame	RP1	Refined Petroleum-1 (a kerosene-based rocket fuel)
EH	Elliptical Hemispherical	RP1.St₁	Tank RP1 stage 1
EOM	Equation Of Motion	RP1.St₂	Tank RP1 stage 2
FALCon	Formation flight for in-Air Launcher 1st stage Capturing demONstration	ROI	Return of investment
FB	Fly-Back	RTLS	Return To Launch Site
FRR	Flight-Readiness Review	S/C	Spacecraft
FS	Factory of safety	SRR	System Requirements Review
F.S.	Forward Skirt	SLS	Space Launch System
GLOM	Gross lift off mass	SSO	Sun Sincronous Orbit
HoQ	House of Quality	S.St₁	Skirt stage 1
HS	Hemispherical	S.St₂	Skirt stage 2
IAC	In-Air Capturing	TBC	Thermal Barrier Coating, a coating that reduces heat load and protects substrate materials
ID	Identification	TRL	Technology Readiness Level
Int	Interstage	TVC	Thrust vectoring control
KKPs	Key Performance Parameters		

Contents

Abstract	I
Acronyms	IV
List of Figures	IX
List of Tables	X
1 Project management	1
1.1 House of Quality	1
1.2 Requirements	1
1.3 Functional analysis	1
1.4 Iterative process	2
1.5 Cost analysis	2
1.6 Launch platform selection	3
2 Main iteration	4
2.1 Energetic budget	4
2.2 Engine implementation	5
2.2.1 Engine and Rao nozzle sizing	5
2.2.2 Regenerative cooling and engine performance	6
2.2.3 COTS engine and TRL qualification	6
2.3 Trajectory propagation	7
2.3.1 Nominal design	7
2.3.2 Off design payload case	10
2.4 Recovery solutions	10
2.4.1 Landing strategies and constraints	10
2.4.2 Boost-back	11
2.4.3 Parachute sizing and opening sequence	12
2.4.4 Upper stage re-entry and stage separation motor	14
2.5 Launcher configuration	14
2.5.1 Design choices	15
2.5.2 Length and mass estimation	16
2.5.3 Launcher discretization	16
2.6 Structures	17
2.6.1 Critical loads conditions	17
2.6.2 Analysis at max $q\alpha$	19
2.6.3 Structural analysis	19
2.7 Aerodynamics	21
2.7.1 Nose	21
2.7.2 Aerodynamic coefficients	22
2.7.3 Tail fins	23
2.8 Static stability and control	24

2.8.1	Static stability margin	25
2.8.2	Equilibrium and stability assessment	25
2.8.3	Free-fall pitch-turn	26
3	Sensitivity analysis	27
3.1	Uncertainty population	27
3.2	Orbit insertion accuracy	27
4	Further developments	28
4.1	Trajectory advancement	28
4.2	Thermal analysis during Re-entry phase	28
4.3	Re-entry	29
4.4	Aerodynamics and control	29
5	Conclusion	30
5.1	Criticalities	30
5.2	Requirements satisfaction	30
Authorship declaration		i
Appendix		ii
A	House of Quality	ii
B	System level requirements	iii
C	Functional tree	v
D	Regenerative Cooling	vi
D.1	Thermal Barrier Coating	viii
E	TRL Roadmap and Gantt chart	ix
E.1	Year 1: Preliminary Development (TRL 1-3)	ix
E.2	Year 2: Component and Subsystem Validation (TRL 4-5)	x
E.3	Year 3: Prototype Development and System Integration (TRL 5-6)	x
E.4	Year 4: Flight-Ready Qualification (TRL 7-8)	xi
F	Detailed model ruling the trajectory	xiii
F.1	Optimization approach	xiii
G	Trajectory with updated payload mass	xiv
H	Re-entry	xv
I	MER and LV discretization results	xvii
J	Loads computations results	xviii
K	Wind modeling	xx

L Material Analysis	xxi
M Mathematical procedure for calculating wall thickness	xxii
N Aerodynamic coefficients	xxiv
N.1 Axial force coefficient	xxiv
N.2 Body normal force coefficient	xxvi
N.3 Fins coefficient	xxvii
N.4 Fins geometry	xxix
O Equilibrium equations	xxx
P Thermal Analysis during the re-entry phase	xxxi
Bibliography	xxxiii

List of Figures

1	Functional tree	1
2	Flowcharts of the iterations	2
3	Cost analysis	3
4	Stage 1 engine nozzle	6
5	Stage 2 engine nozzle	6
7	Evolution of the states of the system	9
8	Main loads acting during the trajectory	10
9	Boostback re-entry trajectory, thrust profile and tangential acceleration.	12
10	Parachute re-entry trajectory and tangential acceleration	13
11	Upperstage re-entry trajectory, tangential acceleration and dynamic pressure	14
12	LV configuration ¹	15
13	Load analysis results @ $\max q$	19
14	C_{D0} comparison	23
15	C_L comparison	23
16	Comparison in first and second iteration results	24
17	Center of mass and static margin shift over atmospheric flight	25
18	State parameters variation during the free-fall	26
19	Monte Carlo energetic analysis results	27
20	Monte Carlo generals analysis results	28
21	House of Quality	ii
22	Launch operations functional tree	v
23	Recovery operations functional tree	v
24	Temperature profiles along the engine axis	viii
25	Gantt Chart Engine TRL Qualification	xii
26	Trajectory with 400 kg payload mass	xiv
27	Main loads acting during the trajectory with 400 kg payload mass	xiv
28	Development Roadmap major system demonstrations for “In-Air-Capturing” [60].	xv
29	Boostback re-entry trajectory	xvi
30	Parachute re-entry trajectory	xvi
31	Load analysis @ $\max q\alpha$	xviii
32	Load analysis @ clamping	xviii
33	Axial load @ <i>meco</i>	xix
34	Axial load @ Recovery	xix
35	Evolution of $q\alpha$	xx
36	AOA and wind speed	xx
37	Axial force coefficient	xxv
38	Axial coefficient components	xxvi
39	Normal force coefficient	xxvii
40	Wing planar section	xxvii
41	Fin’s surfaces identification as of Reference [44]	xxviii
42	Fin C_D	xxix
43	Tail fin geometry	xxix

44	Launcher free-body diagram	xxx
45	Heat flux at different trajectory points on two evaluation locations [66]	xxxi
46	Change of maximum wall temperature over time for selected wall thicknesses [66]	xxxii
47	Three types of retro-propulsion modes [67]	xxxii

List of Tables

1	High-level requirements	1
2	Cost comparison between different staging solution	3
3	First ΔV budget estimation	4
4	First draft of the LV mass	4
5	First stage engine performance	6
6	Second stage engine performance	6
7	Boundaries for the optimization problem	8
8	Output parameters of the optimization process	8
9	Insertion errors	9
10	Updated insertion errors	10
11	ΔV contribution	11
12	Boostback parameters and thruster configuration	11
13	Parachute Sizing	13
14	Parachute Opening Sequence	13
15	Stage separation motor contribution	14
16	Discretize segment length	16
17	Data @ max q	18
18	Data @ $\max q\alpha$	19
19	Mechanical properties of Al-Li 2195	20
20	Launcher wall thickness	20
21	Mass of the primary structure calculated using MER and preliminary design	21
22	Initial estimate of the structural index and the calculated value with preliminary design	21
23	Envelope volume to payload mass ratio of existing launch vehicles [9, 10]	22
24	Equilibrium values for gimbal tilt angles and angles of attack	25
25	Perturbed AOA and relative δ required to avoid rotation with associated time-to-double	26
26	Standard deviations expressed as a percentage of the mean value	27
27	Requirements satisfaction	30
28	System level requirements	iv
29	MER results	xvii
30	C_g^i and m_i @ different flight conditions	xvii
31	LV wall thickness with respect to phase	xxiii
32	Retro-propulsion trajectory points.	xxxi

1 Project management

The conceptual design of the launcher begins with the House of Quality, from which the customer requirements and needed performance are retrieved. Then, from the given specifications, consistent functional requirements are inferred. These parameters are needed to evaluate the effectiveness of the output design. Throughout the design process, feasibility issues are addressed.

1.1 House of Quality

The House of Quality is presented in Appendix A and the main consequent remarks are:

- Recoverability of the first stage is the most important customer requirement, together with keeping safe operations for people on ground.
- The payload mass and the diameter are the most influential parameters.
- From the competitor analysis, the recoverability of the first stage has been confirmed the main innovation.

As already treated in the competitor analysis, Pegasus XL and Launcher One have been selected as baseline for the design. All data taken as reference are shown afterwards for each subsystem.

1.2 Requirements

From the customer requests, the high-level requirements are defined in Table 1:

Req ID	High-level requirement
F-0001	Stage recoverability and reusability shall be considered for the first stage.
F-0002	Launcher shall be capable of bringing payload to LEO orbit.
F-0003	The system shall be airborne from civil aircraft.
F-0004	The launcher shall be in a tandem configuration.
F-0005	The operations shall be safe for people on ground.
F-0006	The system shall include technologies that allow acceptable time to market (target time of 4 years).
F-0007	The system shall include technologies that allow acceptable number of reuses to breakeven.

Table 1: High-level requirements

A more accurate requirement selection with an insight into subsystem-level requirements is presented in Appendix B.

1.3 Functional analysis

The functional tree is divided into two main branches as reported in Figure 1:

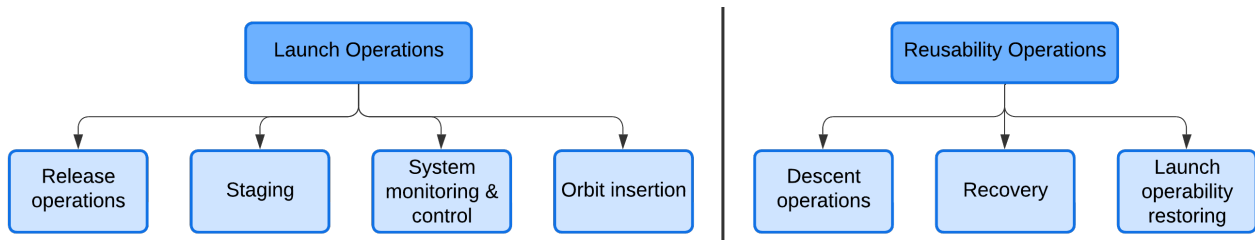


Figure 1: Functional tree

A more detailed functional tree, with each single operation explained in a more specific way, is presented in Appendix C.

1.4 Iterative process

The global design has been divided into segments: staging, engine, trajectory, recovery, structures, aerodynamics, and stability. For each subsystem, an independent MatLab® function has been developed and the results have been compared with the references data. Then, progressively, a general code has been created integrating all the subsystems. The general work flow is shown below in Figure 2:

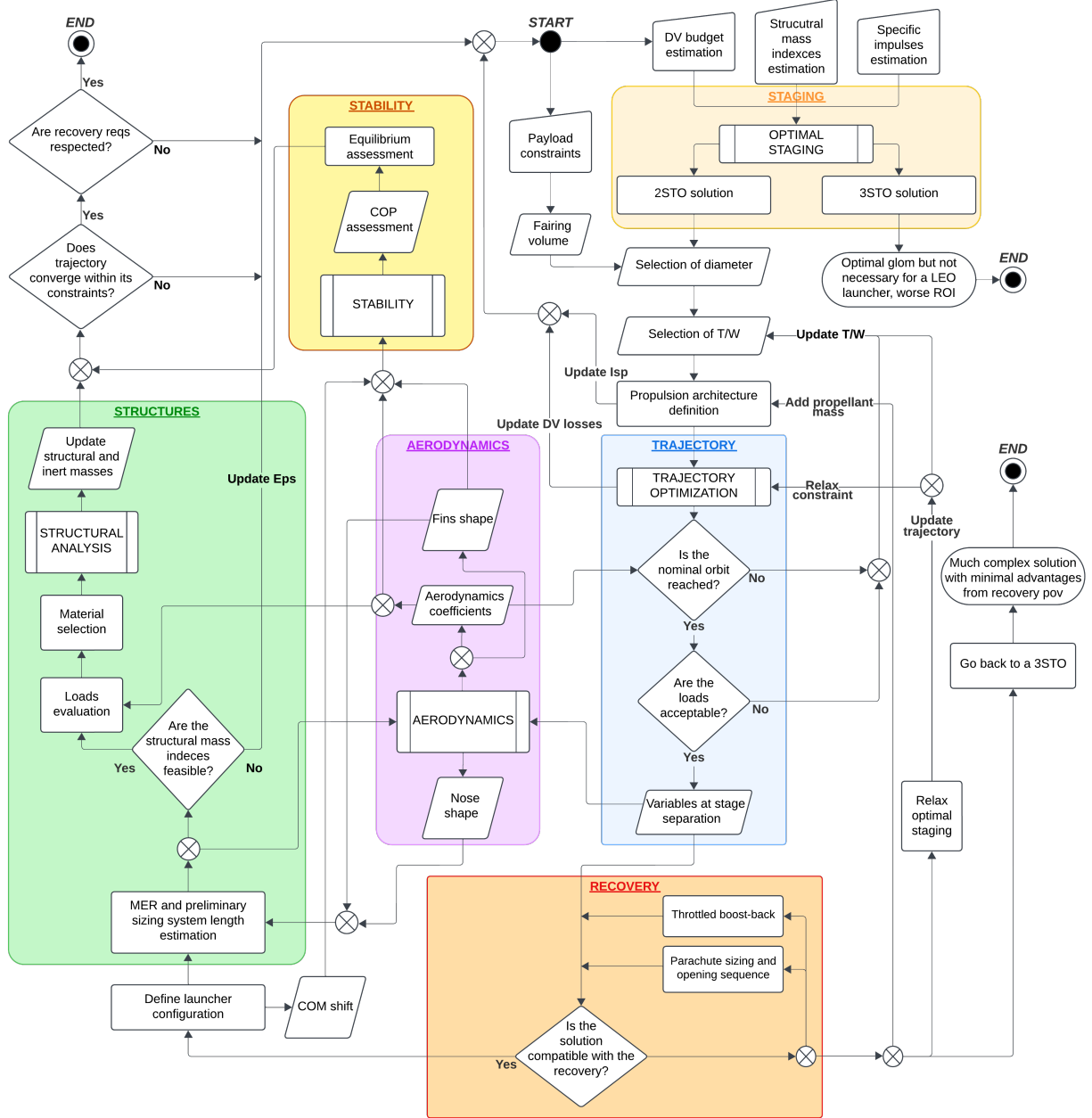


Figure 2: Flowcharts of the iterations

1.5 Cost analysis

To make a trade-off between the different possible technological solutions, a cost analysis has been performed to better understand the context of the mission.

First of all, a comparison with the Launcher One mission has been performed [1] and its cost has been scaled to this specific scenario, considering the different altitude (from 500km to 400km) and payload mass (from 300kg to 250kg). The scaled cost results to be 6.67 M\$, instead of the 10 M\$ of the Launcher One. Then, the cost of each single stage, in the case of 3STO and 2STO, has been computed by distributing the total cost depending on the dry mass as reported in Table 2.

	First stage [M\$]	Second stage [M\$]	Third stage [M\$]
3STO	4.49	1.66	0.51
2STO	5.72	0.94	-

Table 2: Cost comparison between different staging solution

The latter can be considered the cost of the system if the launcher were fully expendable like Launcher One. In order to take reusability into account, two simple rules have been applied:

- The production cost of a reusable stage is increased by a penalty factor K_p . The more complex the technological challenge of the recovery the higher the penalty.
- The refurbishment cost is estimated to be 1/3 of the production cost. This ratio is aligned with what has been noticed from the falcon 9 cost analysis [2].

Using these simple rules it is possible to easily estimate the cost of the entire launch system depending on its configuration. To estimate the revenue of the mission it has been considered that, similarly to Launcher One, the cost for kg of payload is 20 k\$ [1]. In Figure 3 are reported the costs and gains per launch in the case of a 2STO ($K_p = 1.45$) and 3STO ($K_p = 1.30$) where only the first stage is recovered and reused. The penalty factor applied to the 2STO is higher than the one used for the 3STO since the first stage is much heavier and the recovery can be considered more challenging. Other scenarios considering the recovery of the upper stages have been excluded due to technological limitations.

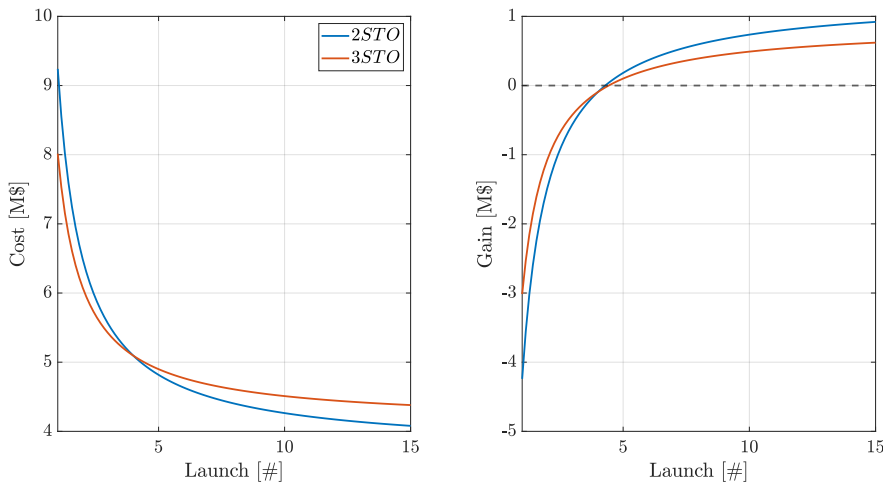


Figure 3: Cost analysis

As shown in the preceding analysis, it's clear that a 2STO will guarantee a better ROI with respect to a 3STO. Given a fixed budget to allocate across all stages, increasing the investment on reusable components results in higher initial costs but greater long-term benefits. This concept has been exploited to guide the design process.

1.6 Launch platform selection

The chosen carrier is a Boeing 767, as it is well-suited for air-launch systems due to its robust aluminium structure which allows for relatively straightforward modifications, such as strengthening the wing or fuselage for payload attachment. Its proven history as a cargo carrier (767-300F) demonstrates its capacity to handle heavy loads [3], making it ideal for supporting a 20000 kg rocket without extensive redesign. Unlike the Boeing 787, which relies heavily on composite materials [4] that are harder and costlier to modify, the 767 metal frame ensures adaptability while maintaining cost-effectiveness. Compared to the 747, the 767 offers lower fuel consumption and sufficient payload capacity. Moreover, it avoids the operational inefficiency associated with larger aircraft like the Stratolaunch platform.

Finally, to account for safe launch and recoverability operations, and for a minor counter-contribution of Earth rotating velocity, the Glasgow airport has been selected. In fact, its strategic position allows all the operations to be executed above the ocean and its longitude ($55^{\circ}52'19''\text{N}$) guarantees a low v_{\oplus} .

2 Main iteration

2.1 Energetic budget

The energetic budget of the mission has been derived starting from the high level requirement of bringing 250 kg payload mass into a 400 km 98° SSO. The gross ΔV budget computation had initially taken into account only the ascent trajectory, but it has been refined after some iterations, when it was clear that a boost-back fire was necessary to guarantee the survivability of the structure during re-entry. The rationale behind the first guess of the required ΔV of 9.2 km/s is explained briefly in Table 3.

Contribution	Rationale	ΔV
Orbit insertion velocity	Nominal ΔV : It coincides with the velocity of a 400 km radius circular orbit [5]	7.67
Earth rotation	Depends on the launch site latitude. It's an undesired contribution that need to be cancelled out since the nominal orbit is a 98° retrograde. The worst case scenario equatorial launch has been considered	0.4
Launch speed	Depends on the maximum allowable speed of the carrier [3]	-0.2
Steering losses	Expected to be performed by aerodynamic surfaces, thus neglected	0
Drag loss estimation	Strongly influenced by the trajectory design and related optimization process. A typical value has been assumed for the first iteration [6]	0.05
Gravity losses	Again strongly correlated with the trajectory optimization and on the gamma angle along the flight. At first estimated inside typical values [6]	1.3

Table 3: First ΔV budget estimation

For the estimated ΔV budget, the optimal staging solution has been pursued in order to obtain a first draft of the LV configuration. The optimization process has been implemented as described in reference [6] and has the aim of minimizing the GLOM of the system. A first guess of specific impulses, structural mass indexes and payload mass are required. Given the chosen propellant couple as explained in Section 2.2, typical values of I_{sp} can be retrieved from the literature [7] and then refined with the actual ones, output of the engine sizing process. The structural mass indexes have been estimated taking into account the size of the LV and kind of propulsive technology. Numerous data can be found in the literature for LOX-RP1 LV capable of launching tons of payload into orbit [6, 7, 8] which indicate an approximate ε_s for the first stage of about 0.09, which is similar to the one of the Pegasus XL [9]. The structural mass indexes values are strongly correlated with the payload mass that the LV can bring to orbit, thus with its size. Even if a lot of data scattering is present, in reference [6] it's clear that for LV with propellant mass in the order of 10000 Kg, as expected for this LV [9, 10], the values of ε_s tend toward 0.12, with greater dispersion for second stage values, up to 0.16. For this specific reasons, it has been decided to set $\varepsilon_{s1} = 0.12$ and $\varepsilon_{s2} = 0.14$. The first draft of the system is visible in Table 4 as output of the 2STO optimal staging.

GLOM [kg]	m_1 [kg]	m_2 [kg]	m_{p1} [kg]	m_{p2} [kg]
14974	13135	1589	11558	1367

Table 4: First draft of the LV mass

The mission energy budget has then been revised through multiple iterations to ensure sufficient propellant is available for both the ascent trajectory and the boost-back re-entry. As stated in Section 2.3 the implemented propagator does not include a rotating Earth model. The mathematical framework will then ignore the contribution of a rotating earth and it will not be considered in the energetic budget. For this specific reason the total budget for the mission is estimated to be 8.83 km/s for the ascent, and 1.69 km/s for the boostback re-entry, resulting in a total velocity requirement of 10.52 km/s. The final mass of the LV is reported in Section 2.6. The proposed solution will then require to be successively refined, with an updated energetic budget to counteract Earth rotational speed.

2.2 Engine implementation

In the preliminary design of a biliquid rocket engine, the decision to develop the propulsion subsystem internally rather than procuring an off-the-shelf solution has been driven by the availability of an unlimited budget for the design of the project. This approach enables complete control over the development process, ensuring that the engine is precisely engineered to meet the specific mission requirements. It is possible to optimize performance parameters, such as thrust and specific impulse, and to size the nozzles suitable for the mission profile. In fact, internal development allows for iterative testing and refinement, ensuring a higher degree of reliability and alignment with system-level objectives.

The biliquid rocket engine is designed to be used in both the first and second stages of the launch vehicle. This decision was taken to reduce costs, simplify development, for an easier and faster qualification processes. By maintaining the same core engine design for both stages, the Technology Readiness Level (TRL) qualification is required for only one engine, significantly saving time and resources. The primary distinction between the two configurations lies in the nozzle design: the first-stage nozzle is optimized for operations at the rocket's release height of approximately 11 km, while the second-stage nozzle is optimized for vacuum conditions. Both designs also account for dimensional constraints to ensure seamless integration with the overall rocket geometry. The first stage requires 12 engines to achieve the necessary thrust imposed by the mission, whereas the second stage is powered by a single engine. Additionally, a very preliminary sizing of the regenerative cooling cycle has been conducted to validate the feasibility of cooling the engine during operation. While the regenerative cycle design remains an approximation, and the cooling channels have not yet been sized, these initial analyses confirm the feasibility of this approach within the scope of the preliminary design.

The chosen propellant combination is RP1-LOX, selected for its excellent performance characteristics. However, this choice comes with drawbacks, including environmental impact and the complexity of handling liquid oxygen as a cryogenic fluid. While RP1-LOX is not classified as a toxic propellant [11, 12], it does not qualify as a green propellant combination. LH2-LOX was also evaluated due to its high performance and environmentally friendly nature. However, it was ultimately discarded due to the low density of liquid hydrogen implying larger storage volumes within the rocket, and it also shares the complexity of handling two cryogenic fluids. Solid motor technology was discarded due to incompatibility with reusability constraints and lack of flexibility required by the profile mission.

2.2.1 Engine and Rao nozzle sizing

Chamber pressure is fixed at 160 bar, balancing efficiency with material and structural limitations. The optimal oxidizer-to-fuel (O/F) ratio is then computed at the given chamber pressure using outputs from Chemical Equilibrium with Applications (CEA) software, considering only a convergent nozzle to eliminate any dependency on nozzle geometry. The optimal O/F is identified as the ratio that provides the highest specific impulse.

With the optimal O/F, an initial sizing of the nozzle can be performed to determine the expansion ratio. Using the nozzle's expansion ratio, the engine's performance is characterized through CEA, yielding the specific impulse and the characteristic velocity.

For the sizing of the combustion chamber, the mass flow rates are computed based on the required thrust and specific impulse.

With a characteristic length of 1.2 m [13] and the c^* of the engine, the geometry values of the nozzle are determined. The contraction ratio is calculated using the experimental Relation 1 [14]:

$$\frac{A_c}{A_t} = 8 \cdot (d_{\text{throat}} \cdot 100)^{-0.6} + 1.25 \quad (1)$$

All the geometry values of the combustion chamber are derived based on these calculations.

A Rao nozzle shape is selected to achieve higher performance compared to a conical nozzle while remaining more compact than a bell-shaped nozzle. With the throat diameter, chamber diameter, expansion ratio, and relative length with respect to a 15° conical nozzle, the geometry of the nozzle's divergent section can be determined. The Rao angles are obtained from literature tables [7].

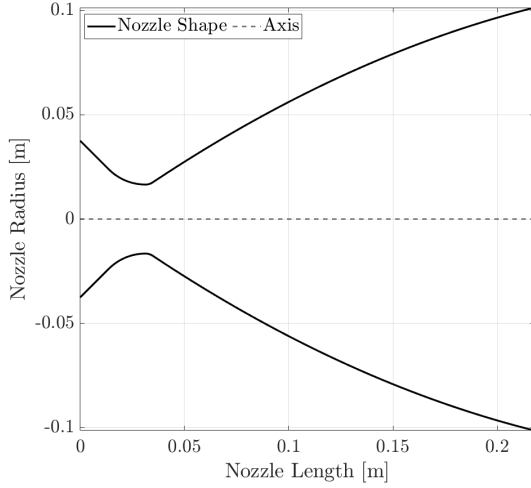


Figure 4: Stage 1 engine nozzle

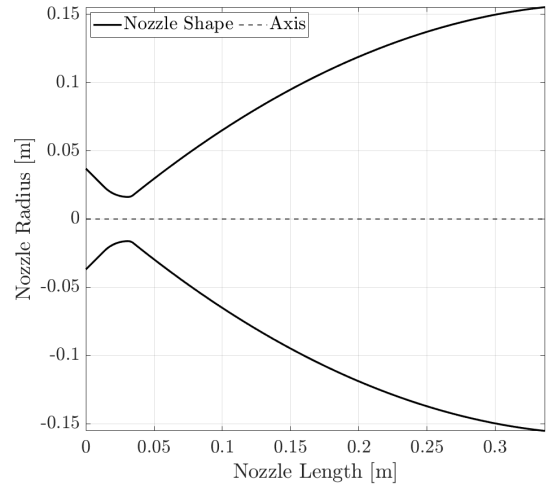


Figure 5: Stage 2 engine nozzle

2.2.2 Regenerative cooling and engine performance

The preliminary regenerative cooling analysis confirms its feasibility, ensuring effective heat management in critical engine areas. To enhance reusability, the combustion chamber is constructed from Inconel, known for its high-temperature durability, and coated with a thermal barrier. This coating significantly reduces thermal stress, protects against oxidation, and minimizes material degradation, allowing the engine to withstand repeated thermal cycles and extend its operational lifespan, making it ideal for multiple launches and cost-effective operations. In Appendix D are reported all the sizing procedures, models and approximations assumed and the design choices.

In Tables 5 and 6 is reported a summary of main engine performance and dimensions. The two engines are almost identical, the differences are given by the different nozzles.

Parameter	Value	Unit
Chamber Pressure	160	bar
Optimal O/F Ratio	2.14	-
Specific Impulse	323	s
Thrust per Engine	24.41	kN
Mass Flow Rate	7.7	kg/s
Expansion Ratio	37.53	-
Throat Diameter	33.12	mm
Exit Diameter	202.87	mm
Chamber Diameter	75.15	mm
Chamber Length	233.01	mm
Chamber Volume	1.0336	L

Table 5: First stage engine performance

Parameter	Value	Unit
Chamber Pressure	160	bar
Optimal O/F Ratio	2.14	-
Specific Impulse	336	s
Thrust per Engine	24.33	kN
Mass Flow Rate	7.4	kg/s
Expansion Ratio	91.85	-
Throat Diameter	32.41	mm
Exit Diameter	310.6	mm
Chamber Diameter	73.91	mm
Chamber Length	230.73	mm
Chamber Volume	0.9899	L

Table 6: Second stage engine performance

2.2.3 COTS engine and TRL qualification

The Rutherford commercial-off-the-shelf (COTS) rocket engine [15] meets the required specifications. However, developing an engine in-house provides greater benefits. With no budget constraints, it is possible to fully optimize performance, tailor designs to unique needs, and gain valuable expertise. Internal development also ensures better integration with existing systems and improve reusability, since the engine is designed for this specific mission. Purchasing the Rutherford engine would sacrifice these advantages. It would only be beneficial if internal development couldn't qualify an engine within four years (requirement F-0006), where a proven solution would guarantee timely product launch. Otherwise, internal development remains the more strategic and advantageous choice.

Although regenerative rocket engines are well-established in the industry, the roadmap and Gantt chart reported in Appendix E assumes starting from a very low TRL and progresses through a structured

four-year development cycle. During Year 1, preliminary designs and conceptual studies define Critical Technology Elements and validate basic principles through small-scale experiments, culminating in a Preliminary Design Review. In Year 2, breadboard and then brassboard components are tested under increasingly realistic conditions to refine designs and address life-limiting mechanisms, leading to a Critical Design Review. By Year 3, high-fidelity prototypes undergo hot-fire tests and scaling evaluations, verified through a Pre-Qualification Review, before system-level integration. Finally, Year 4 focuses on operational, flight-like testing to ensure durability, environmental resilience, and alignment with mission requirements, concluding with a Flight-Readiness Review and subsequent qualification testing. This systematic approach ensures that by the end of the process, the engine reaches TRL 9, so fully flight-proven and ready for serial production.

Four years may be short for moving a low-TRL engine to flight readiness, but it's still achievable with careful planning and focused development. To mitigate schedule risks, the option of purchasing a proven COTS engine was also considered as a backup.

2.3 Trajectory propagation

2.3.1 Nominal design

Assumptions The trajectory is designed following a 2-DOF point mass model assumption with a frame of reference set to be coincident with the centre of a non-rotating windless Earth. The detailed equations are reported in Appendix F. Additional hypotheses considered in the equations describing the dynamics are outlined below:

- **Thrust profile:** the force is considered aligned with the velocity and it is kept at a constant level, disregarding the change in the static term as an initial modelling assumption. This approximation holds true for the second stage since the variation of the external pressure is negligible above a certain altitude where the upper stage is expected to be operated. On the other hand, the first stage performances are underestimated at this design phase since the actual epsilon of the nozzle might vary in future iterations.
- **Angle of attack :** the lift and drag components are computed considering a zero AOA. Following this assumption, the coefficient C_L is considered null for a symmetric body shape, while C_D is fixed to 0.2 as a first average estimation. This simplification allows for a lower computation time by avoiding to interpolate precise data from the aerodynamic model at each time instant, which is not a viable alternative during the optimization process at this stage of the project.
- **Density model:** an exponential model is adopted with a scale height $H = 7500\text{m}$.
- **Gravitational acceleration:** varies according to the distance from the centre of the Earth, considered as a spherical body.
- **Control policy:** an ideal control system is assumed to maintain a moderate but steady $\dot{\gamma}$ during the first-stage ascent phase, while being disabled for the remaining trajectory to allow for a natural gravity turn.
- **Earth rotational contribution:** the initial velocity is assumed to be aligned with the target orbital plane inclination, counteracting a small portion of the Earth rotational term. The actual problem cannot be modelled with a planar assumption, therefore it is not possible to simulate a correction of the cross plane initial velocity. As previously mentioned in the Section 2.1, the energetic contribution required to perform such correction is accounted for in the initial mass budget, however it is not in the case of the updated mass for the re-entry constraints.

Optimization The operations begin with the release from the carrier, followed by a free-fall lasting a few seconds, which are not directly part of the optimization since it would require a more detailed modelling to capture the aerodynamic forces enacting of the body and characterizing the dynamics. Nevertheless, the presence of such initial sequence is taken into account in the lower and upper thresholds of the set of variables in order to be feasible starting conditions. Furthermore, a 3-DOFs dynamic stability analysis during this free-fall phase is performed in Section 2.8.3.

The trajectory is subdivided into three parts: the first leg, a coasting phase and then a second leg. The first leg starts from the end of the free-fall, when the ignition of the engines of the first stage takes place, up to stage separation. The coasting phase provides greater flexibility to the solver, allows time to complete detachment operations, and exploits the acquired inertia to gain additional altitude at the expense of velocity. The second portion of the trajectory is performed only by the upper stage until orbit insertion is reached. It might be completed with the engines turned off since the burning time is not set to coincide with that of the second leg.

The optimization is applied to the release conditions after the free-fall manoeuvre, the time duration of the different sections of the trajectory, the variation of the flight path angle during the first leg and an additional propellant mass applied on the second stage. In order to achieve a feasible solution, upper and lower boundaries are applied to the current set of variables, as explained in Table 7.

Bounds	v_0 [m/s]	γ_0 [deg]	h_0 [km]	t_{b1} [s]	t_{off} [s]	t_{b2} [s]	$\Delta\gamma$ [deg]	Δm_{prop2} [kg]
Lower	180	0.001	9	50	1	150	1	10
Upper	v_c^1	15	12	160	300	480	37.5	$1 \cdot 10^4$

Table 7: Boundaries for the optimization problem

In this framework, the minimization was initially carried out on the Δv_{loss} to lower the GLOM, but in a successive iterate it was then set to be exactly a weighted sum of the insertion errors. The motivation behind this choice was to refine the solution in the vicinity of a local minimum, which seemed to hardly match the constraints imposed on the solver. This issue is likely due to the highly non-linear dynamics involved. Furthermore, this is also reflected in the significant variation in the method's ability to converge on a good solution depending on the initial guess. In addition to the target function, a set of non-linear constraints are defined to fully complete the statement of the problem. The equality ones determine the target final values (v_f, h_f, γ_f) of a circular orbit at the required altitude. The inequality constraints are instead set to limit the height and velocity at the stage separation to increase the chance of matching recovery requirements. A more detailed mathematical explanation of the optimization is presented in Appendix F.

Results During the refinement process, from the recovery point of view, a substantial amount of propellant was lacking to perform a partial boost-back which seemed necessary to avoid critical loads during the re-entry leg. The problem was addressed by adding, from this constraint, an amount of propellant to the first stage and carefully adjusting this quantity to avoid adding excessive mass, which could compromise the primary mission of delivering the satellite into its predetermined orbit. Accordingly, a total of 3700 kg are added to the propellant mass of the first stage defined previously in Section 2.1.

The outcome of such optimization is a set of initial conditions and other parameters, visible in Table 8, required to integrate the equation of motion giving rise to the actual trajectory represented in Figure 7 with a value of $\Delta v_{losses} = 1.38 \cdot 10^3$ m/s, where $\Delta v_{gravity} = 1.26 \cdot 10^3$ m/s and $\Delta v_{drag} = 0.12 \cdot 10^3$ m/s.

v_0 [m/s]	γ_0 [deg]	h_0 [km]	t_{b1} [s]	t_{off} [s]	t_{b2} [s]	$\Delta\gamma$ [deg]	Δm_{prop2} [kg]
226	1.7	10.8	144.7	4.8	415.9	33.2	1683.6

Table 8: Output parameters of the optimization process

It's important to emphasise that the initial GLOM is increased with respect to the one obtained from the optimal staging, by the sum of newly added propellant on both stages and by the structural mass adjusted to maintain the initial supposed structural mass index. The rocket with an updated GLOM of 20593 kg achieves a correct orbit insertion still granting staging conditions below the defined limit: $v_{staging} = 2904$ m/s and $h_{staging} = 87.3$ km. All the left over propellant on the first stage amounts to 1567 kg and will be used in the re-entry phase. As a final remark, it is evident that the coasting phase is reduced almost to the minimum to avoid losing velocity which seemed to be a pivoting problem.

¹The maximum allowed initial velocity of the LV is set to be coincident with the actual release velocity of Pegasus XL [9]: $v_c = 234$ m/s.

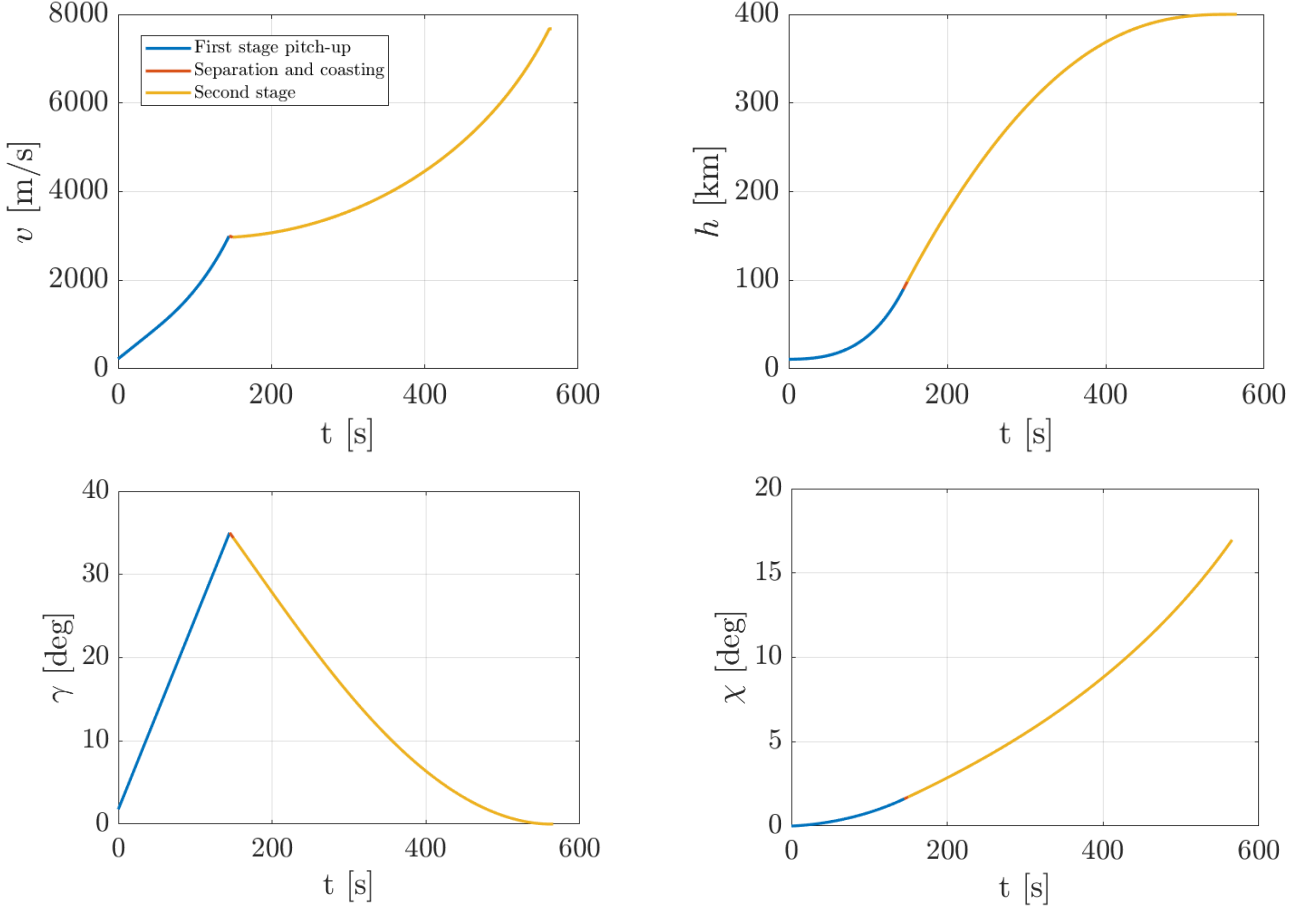


Figure 7: Evolution of the states of the system

The discrepancy with respect to the target final conditions is within reasonable margins as reported in Table 9, demonstrating the ability of the model to converge to a solution inside the given mathematical framework .

err_v [m/s]	err_γ [deg]	err_h [m]
+6.0	$-4.2 \cdot 10^{-3}$	+9.3

Table 9: Insertion errors

A further manipulation of the states of the system allows to estimate important forces and accelerations enacting on the launcher during its trajectory:

- **Acceleration profile:** the reported trace (Figure 8a) is well below typical limitations [6], even though it is missing the contribution of a normal acceleration which is of minor relevance with respect to the tangential one. It is worth noticing that the final leg is substantially longer than the first one to get to the target final velocity with a low T/W without exceeding the maximum allowed acceleration of 5 g, imposed by the requirement D-STR-0008, reported in Appendix B.
- **Dynamic pressure profile:** the peak and its amplitude is slightly higher but comparable to the one experienced by the Pegasus XL [9]. The estimated maximum dynamic pressure within the model assumption is 69.4 kPa at an altitude of 15.59 km. This pressure is considerable and will be part of a further structural analysis in Section 2.6.1 to verify the feasibility.
- **Maximum temperature:** it is estimated to reach a value of 1630 K in the stagnation point following an analysis in which transients are neglected and a simple thermal balance is performed at each time instant (Equation 2) [16]:

$$\dot{Q}'' = k_{th} \cdot (\rho/R_n)^{0.5} \cdot v^3; \quad T_{wall} = \left(\dot{Q}'' / (0.8\sigma_0) \right)^{0.25}; \quad (2)$$

where $R_n = 9.6$ cm and $k_{th} = 1.7415 \cdot 10^{-4}$. This temperature is rather high and will have to be counteracted by choosing a suitable thermal protection on the nose tip.

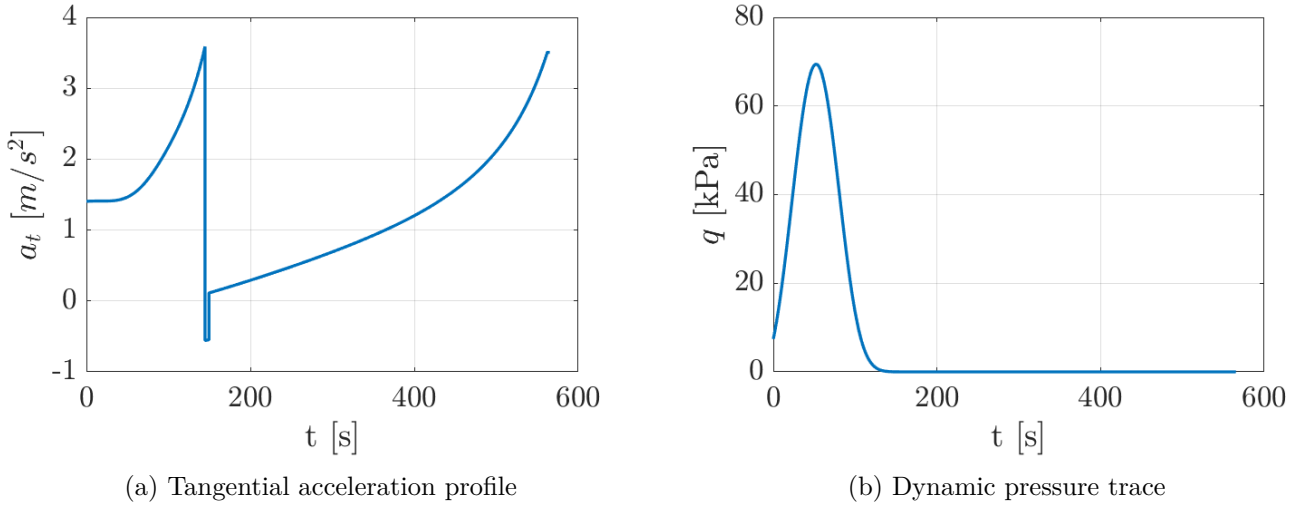


Figure 8: Main loads acting during the trajectory

2.3.2 Off design payload case

In the case of an updated payload mass of 400 kg, the initial conditions previously found are propagated in time defining the trajectory with the newly changed masses and the insertion errors in Table 10.

err_v [m/s]	err_γ [deg]	err_h [km]
-497.3	$-5.52 \cdot 10^{-2}$	-69.05

Table 10: Updated insertion errors

In conclusion, the energetic content of the the rocket is not enough to guarantee both the recovery of the first stage and insertion, nor in the target orbital plane nor at the required height as it is shown in detail in Appendix G. Considering this model of the trajectory, no feasible solutions are found at the current phase of the project. Possible alternatives might include modifying the target conditions to relax the strong constraints imposed on the design:

- **Change of the inclination and launch site:** it would be beneficial to exploit the initial velocity contribution of the Earth and to launch in a prograde orbit near the equator to maximize such gain.
- **Control policy:** to achieve such a low orbit while managing to accelerate to a sufficient circular velocity, it will be required to implement a control system on the flight path angle of the second leg to maintain a slightly positive value, counteracting partially the natural gravity turn.

2.4 Recovery solutions

The return strategy and landing mode are likely among the design choices with the largest impact on the development as specific technology adoption depends on this choice. Recovery was indeed the most constraints demanding subsystem. While a horizontal landing (or take-off) requires wings that allow the vehicle to be safely operated throughout a wide range of Mach numbers, a vertical landing requires a highly reactive throttling capability for its rocket engines, among others. While both recovery approaches are well-established in the American market, European companies still need to acquire or further develop the associated technologies and capabilities.

2.4.1 Landing strategies and constraints

Various strategies for the recovery of reusable first-stage launchers were evaluated, including return to launch site (RTLS), downrange landing (DRL), fly-back (FB), in-air capturing (IAC), and splashdown. Each method offers distinct advantages and challenges, as detailed in Appendix H.

A splashdown solution was selected due to its simplicity, lower components weight, and effectiveness, meeting the constraints provided by the customer. Seawater poses a significant challenge as it causes both corrosion and thermal shock to the exposed components. However, some solutions have been identified in the literature to mitigate this damage [17].

The entire re-entry phase has been meticulously designed to comply with the following requirements:

- **Axial Load on the Structure:** the axial load transmitted to the structure shall not exceed 6 g. Although higher values have been reported in the literature [18], the mission primary objective is the full recovery and reusability of the entire first stage (requirement F-0001), therefore it is essential to minimize the acceleration transmitted to the structure.
- **Load on the Parachute:** based on values reported in the literature, the load transmitted to the parachute shall not exceed 5 g [19]. Although the structure may be designed to handle greater accelerations, the maximum value during the parachute deployment must remain below 5 g, especially during the opening phase, where significant shock loads will be transmitted to the system.
- **Velocity at 13000 m Altitude:** the velocity at an altitude of 13000 m must be less than 440 m/s (equivalent to Mach 1.5). At this altitude, the drogue parachute is expected to be deployed and controlling the velocity is critical to prevent instabilities. While the selected parachute is certified to function at speeds up to Mach 2.7 [20], it is unclear whether this limit reflects tests conducted in wind tunnels or real-world scenarios, so a safety margin has been applied.
- **Touchdown Velocity:** the touchdown velocity must be below 10 m/s (requirement M-STR-0006) to minimize the load upon contact with the water surface [21].

2.4.2 Boost-back

The boost-back strategy consists of two main phases, during which the system generates thrust as follows:

1. **Post-MECO flip manoeuvre:** immediately after MECO, a flip manoeuvre is executed to properly orient the thrusters; although the control thrusters are not designed, values of their weight and burning time are properly scaled and assumed from literature [22].
2. **Initial Boost Phase:** 30 seconds after MECO, the stage is assumed to have completed the flip manoeuvre and is prepared to fire its engine. The first boost is initiated to reduce velocity and lower the maximum apogee altitude.
3. **Engine shutdown:** 46 seconds after MECO, the engine is shut down, transitioning the stage into a ballistic trajectory.
4. **Atmospheric entry boost:** at 370 seconds after MECO, as the stage enters the denser layers of the atmosphere, a second boost is performed to further reduce speed and limit the structural load factor.
5. **Final engine shutdown:** at 410 seconds after MECO, the engine shuts down again, marking the beginning of the final phase of re-entry.

Some relevant data are reported in Table 11 and Table 12:

ΔV_{tot} [m/s]	ΔV_{prop} [m/s]	ΔV_{drag} [m/s]	$\Delta V_{gravity}$ [m/s]
-2537.0	-1693.9	-1297.0	+453.9

Table 11: ΔV contribution

	ΔV [m/s]	m_p [kg]	Engine Configuration
First Boost-back	346.2	357.1	8 external engines at 90%
Second Boost-back	1347.7	1071.3	4 internal engines at 50-100% ²

Table 12: Boostback parameters and thruster configuration

As observed, during the first boostback only 25% of the propellant is consumed, resulting in a relatively small reduction in velocity and apogee altitude. This decision was primarily driven by the observation that the second boost is generally more effective in satisfying the imposed constraints, thus the first boost contribution was intentionally limited to save up more propellant for the second phase.

A key consideration in selecting the engine configuration for the boostback must be addressed: for the first boost, simulated data indicate that a short, intense burst is more effective than a weaker, prolonged

²The throttling varies in time as shown in Figure 9.

one. Consequently, the engine configuration was chosen to deliver the maximum thrust while keeping acceleration below 6 g. The eight external engines fire at 90% capacity, ensuring symmetric thrust. Conversely, during the second boost, it is crucial to reduce thrust as the atmospheric density increases and aerodynamic loads grow. For this reason, only the four internal engines are used, and the throttle is actively controlled to decrease thrust when higher acceleration is detected; even in this case thrust is symmetric. In the simulation, a simple yet effective proportional controller was implemented to manage throttle adjustments. Alternative configurations, as discussed in Section 4.2, could be explored to further mitigate heat flux. In Figure 9 (and Figure 29 in Appendix H) the results of the simulation are presented.

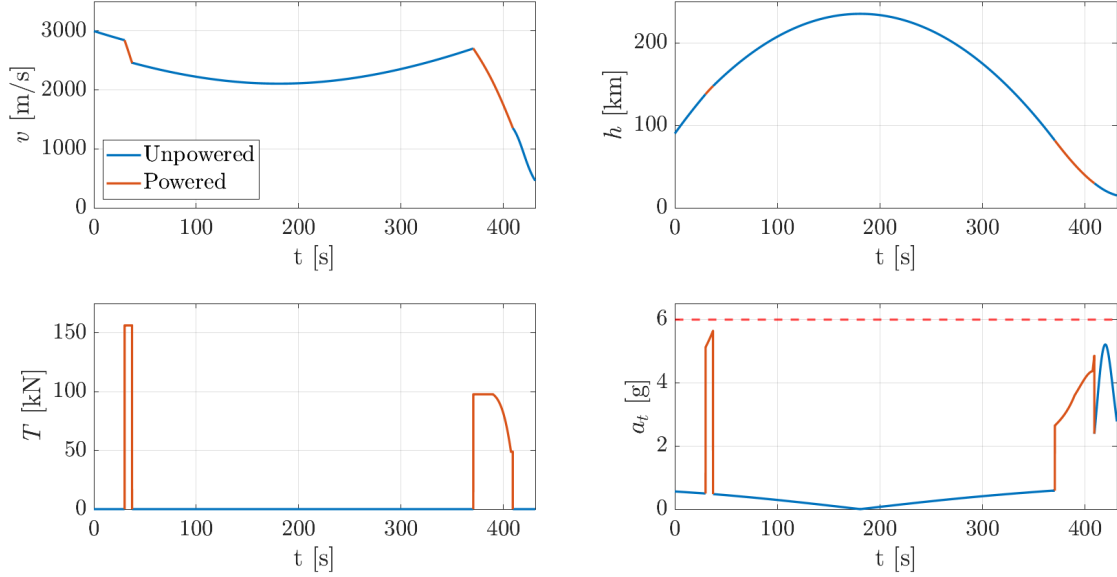


Figure 9: Boostback re-entry trajectory, thrust profile and tangential acceleration.

2.4.3 Parachute sizing and opening sequence

As drogue parachute a Disk-Gap-Band (DGB) has been chosen, which is considered to be simple and effective in both supersonic and subsonic regime [20]. The drag coefficient in supersonic has been estimated using the empirical law in Equation 3 [23]:

$$(C_{D_0})_d = \left[\frac{\eta_{drogue}}{(M^2 - 1) + 0.7} \right]^{0.3} (0.305 \ln \xi_{const} + 1.106)^{2.4} \quad (3)$$

where M is the Mach number, η_{drogue} is the porosity (assumed to be 0.125 according to [23]) and ξ_{const} is the reefing factor. This correlation works properly in supersonic regime while in subsonic conditions the coefficient has been assumed to be the one computed with M=1. The shock factor is assumed to be 1.3 [20]. The approximate weight of the drogue parachute can be estimated from Equation 4 [24]:

$$W_d = 0.12 (C_{D_0} A)_d + (0.28 \times 10^{-3}) q_\infty (C_{D_0} A)_d^{3/2} \quad (4)$$

with $C_D A$ being the the Drag Area and q_∞ the free-stream dynamic pressure. The first term accounts for the canopy weight and the second term accounts for the suspension-line weight. Considering $C_D A = 0.6859 \pi 1.5^2 = 4.8483 \text{ m}^2$ and $q_\infty = 14.8 \text{ kPa}$, the mass of the drogue parachute is estimated to be 4.6 kg. The main is a ring-sail parachute and the drag coefficient has been estimated through Equation 5 [25]:

$$C_{D_0} = 1 - K_l \left[\left(\frac{l}{D_0} \right)^2 - 1.17 \right] \quad (5)$$

where $K_l = 4.5$ and $l/D_0 = 1.4$. The shock factor is assumed to be 1.1 [23]. The formula used to calculate the main parachute mass is reported in Equation 6 [25]:

$$m_c = K_m D_0^2 \quad (6)$$

where $K_m = 0.078$ is a coefficient to correlate experimental data and D_0 the nominal diameter. With these considerations the main parachute mass is 45 kg.

The masses of the control system and the mortar used for parachute deployment are included in the calculations. Average values are derived from the literature and appropriately scaled for both the main and drogue parachutes mass [26]. Taking into account a safety margin of approximately 22%, the total mass is estimated as stated in Equation 7:

$$M_{tot} = m_{drogue} + m_{main} + m_{mortar} + m_{control} + m_{margin} = 4.6 + 45 + 2.3 + 2.9 + 10.9 = 65.7 \text{ kg} \quad (7)$$

After calculating the total masses of the system, the overall volume was determined using the average density of the system [26]: V_{tot} is equal to 0.1 m³. For redundancy, a complete copy of the parachute system is included. As a result, the total mass M_{tot} and the occupied volume V_{tot} double.

The sizing has been performed by considering the limitation on terminal splashdown velocity (< 10 m/s) and on the maximum acceleration allowable (< 5 g). This process led to the configuration presented in Table 13:

Parachute	d_{par} [m]	v_f [m/s]	Reefing ratio	$C_D(t)$	m [kg]	V [m ³]
Drogue	3	80.7 (@ 3.2km)	(1) ³ 40 %	0.299 - 0.686	4.6	0.006
Main	24	9.7 (@ 0.0km)	(2) 10 - 40 %	0.762	45	0.062

Table 13: Parachute Sizing

Each reefed phase is expected to last 10 s. The reefing ratio of the first reefing line applied to the main parachute is very low but similar values have been found in literature [27, 28]. Nevertheless, in a more advanced level of detail, this ratio could be relaxed of 15% or even higher percentage in order to avoid issues during the opening phase. The opening sequence has been defined as in Table 14:

Parachute	Altitude [km]	Velocity [m/s]	Dynamic Pressure [kPa]	Max shock [g]
Drogue	13	335	14.8	4.0
Main	3.2	81.7	2.9	4.8

Table 14: Parachute Opening Sequence

The total downrange distance from the launch site to the landing location is 1029 km, while this value is significant, it should not pose a risk to the population if the trajectory is planned to pass over the ocean (requirement D-0008). In a more advanced design phase, the exact landing location should be carefully determined. The results of the simulation are shown in Figure 10 (and Figure 30 in Appendix H):

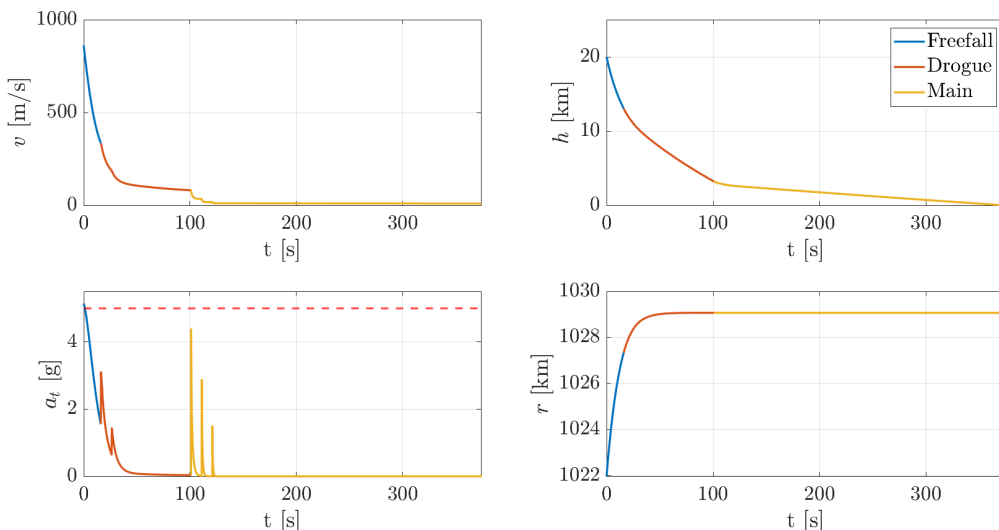


Figure 10: Parachute re-entry trajectory and tangential acceleration

³The drogue parachute contains only 1 reefing line, while the main one contain 2 different reefing line.

2.4.4 Upper stage re-entry and stage separation motor

Although the upper stage will not be recovered, a disposal strategy has been developed. After the payload is released, the re-entry of the second stage is initiated by providing a ΔV using a set of small solid rockets mounted on the nose of the fairing. It has been estimated through a Matlab® simulation that a ΔV of 100 m/s is sufficient to trigger the descent; considering an I_{sp} of 220 s, this requires approximately 21.8 kg of propellant. The covered downrange is approximately 18906 km and the descent must be carefully timed to ensure the system lands in the ocean and avoids passing over populated areas. The results of the simulation are shown in Figure 11:

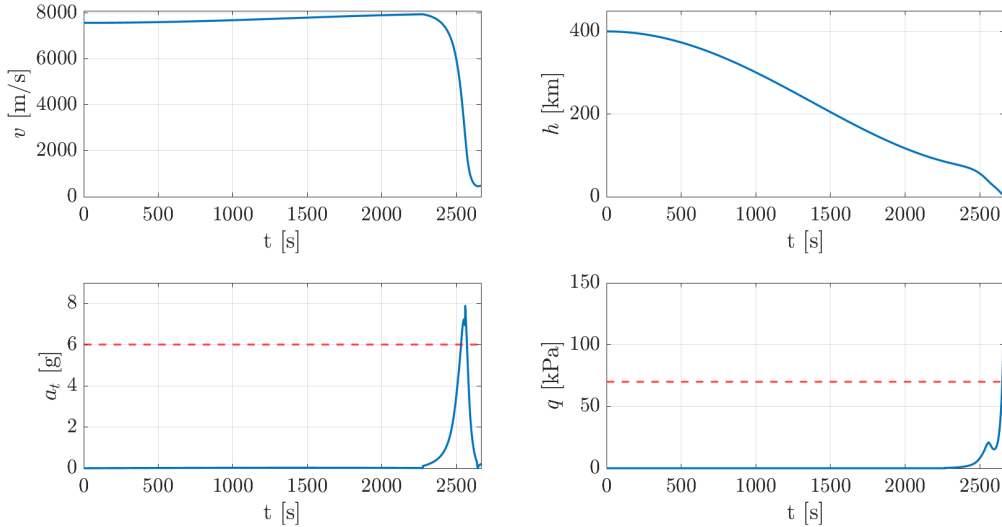


Figure 11: Upperstage re-entry trajectory, tangential acceleration and dynamic pressure

The recovery of the upper stage has been ruled out, primarily due to the significant dynamic pressure the system experiences. To mitigate this pressure, it would be necessary to decelerate the system before entering the denser layers of the atmosphere and this could be achieved by carefully controlling the re-entry trajectory through a skipping or lofting re-entry. However, the feasibility of these solutions requires thorough evaluation, and its implementation would entail an additional attitude control system.

Another potential approach is to conduct a boost-back re-entry, but this would require additional propellant. In either case, the mass of the upper stage would inevitably increase, degrading the overall performance of the system, for these reasons, the recovery of the upper stage has been excluded from the presented iterations.

Ultimately, a set of stage separation motor based on solid propellant has been implemented in order to ensure safe first stage separation and to provide the necessary ΔV to trigger the upper stage re-entry. By taking as reference the BSM used in the SLS system [22], it is possible to estimate a structural mass index of 0.55 and an I_{sp} of 220s. Using these values, the results in Table 15 have been obtained:

Stage	m_{tot} [kg]	m_p [kg]	ΔV [m/s]
First stage	100.0	45.0	28.0
Main	48.4	21.8	100.0

Table 15: Stage separation motor contribution

2.5 Launcher configuration

The refined system configuration has been derived starting from the input received by the trajectory optimization process. Most of the volume and weight in a launcher is attributed to propellant [6] thus tanks-related design choices will have a great influence in the overall length of the LV and stability.

2.5.1 Design choices

A common bulkhead configuration has been selected for both first and second stage propellant tanks. This allows for the tanks walls themselves to carry the primary loads [29] reducing the weight of the system and its total length. On the other hand, the common bulkhead design is critical from the thermal point of view, since LOX-RP1 is a semi-cryogenic couple, thus thermal insulation must be present and correct bonding of the adhesive paste must be guaranteed at low temperatures [6]. An additional criticality is the capability of withstanding the loads, which is strictly correlated to the shape of the dome. Typically an honeycomb structures with fiberglass reinforcement is required [30]. The cylindrical tanks dome shape has been selected as EH, shorter with respect to HS ones. For this specific reason the AR has been set equal to 2 [6], thus some compressive stresses will be present since the aspect ratio is greater than $\sqrt{2}$ [30]. The optimization process of the dome shape is critical in the LV design but it is generally performed in a more advance phase, thus it has not been pursued.

The RP1 tank is placed closer to the engine for both stages. This is advantageous from the thermal point of view, since the cryogenic oxygen is further away from combustion chamber and more importantly it guarantees a C_g which is close to the nose with respect to the case in which the RP1 tank is placed in front of the heavier LOX one. Moreover, the C_g travelling is reduced and this is beneficial from the stability point of view [6]. For further considerations on stability the reader is referred to Figure 17. An issue with the selected configuration are the long LOX internal feeding lines that go through the RP1 tank [6]. Heat transfer could lead the oxidizer to reach too high temperatures.

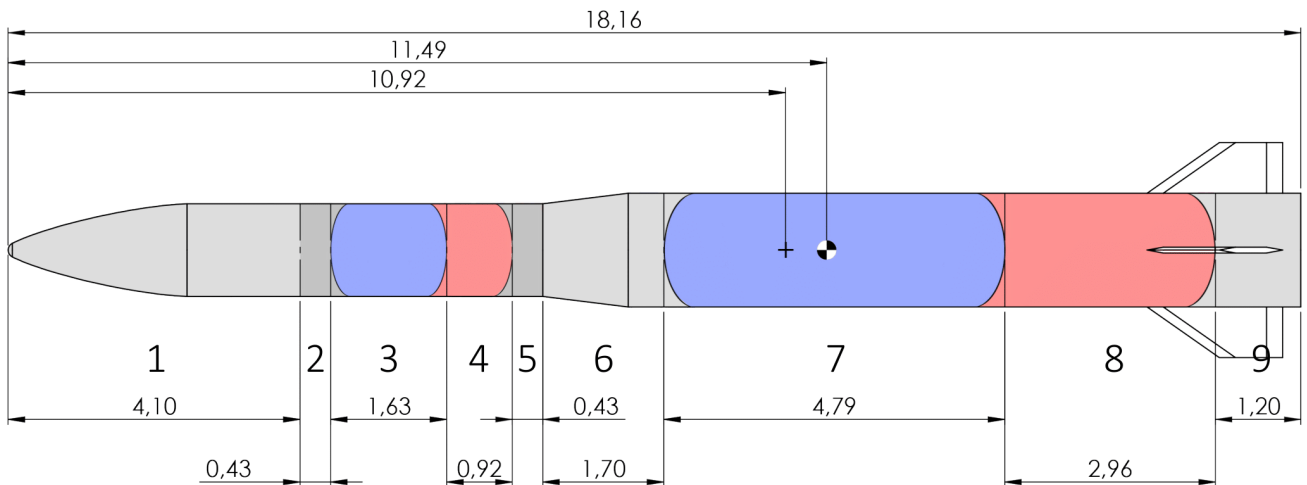


Figure 12: LV configuration⁴

Having fixed the shape, the volume of LOX and RP1 tanks have been computed starting from the propellant masses required by the mission in each stage. A 3% margin has been added to the nominal value for both LOX and RP1 to take into account ullages [6, 7]. The first stage propellant volume is equal to 15.05 m^3 while 3.1 m^3 for the second stage. Consequently a turbopump-based architecture has been chosen for both stages, as it minimize the inert masses with respect to a pressure fed solution [7]. A minimum pressure inside the tanks must be in any case guaranteed for two reasons: to avoid pumps cavitation and to increase buckling resistance [6]. Choosing Helium as pressurizing gas initially at 500 bar pressure [7], preferred with respect to Nitrogen since it reaches a lower temperature at the end of the expansion, the required⁵ amount to maintain 2 bar inside the tanks is 52 kg for the first stage and 11 kg for the second stage. The helium has been distributed into Ti-6Al-4V spheres, with diameter of about 48 cm (first stage), 28 cm (second stage) for the LOX ones and 38 cm (first stage), 24 cm (second stage) for the RP-1 ones, positioned in the skirts and interstage. Titanium alloy has been preferred with respect to aluminium due to an higher index of merit σ/ρ , which allows to minimize the mass. The expansion of the pressurizing gas has been assumed in first approximation isoentropic [7].

In order to have second stage structural tanks, a diameter reduction from 1.6 m of the first stage was

⁴Lengths are expressed in meters.

⁵The followed procedure is explained in Reference [7].

necessary. The selected 1.3 m diameter [10], used for the trajectory computation at first place, allows to exploit also the second stage tanks for structural purposes. This maximum diameter constraint influences the length of the payload fairing, which has to be increased with respect to the typical values [6] to accommodate the maximum expected payload volume. In order to guarantee a proper fairing envelope an additional 1.5 m cylindrical shape has been dedicated for the payload housing. Further explanations about the nose shape and volumes are reported in Section 2.7.1. The overall esteemed payload-dedicated envelope amounts to 3.4 m³ excluding unusable regions of the nose tip from the count respecting the minimum value computed in Section 2.7.1 with a conservative margin.

2.5.2 Length and mass estimation

To estimate the total LV length, suggested dimensions to size the interstage and skirts have been taken as reference [6]. In order to accommodate the parachute and the pressurizing gas spheres for the LOX tank, the first stage length needed to be increased by 50 cm from the top of the LOX tank dome. The configuration of the LV and its division into segment for the structural analysis is reported in Figure 12. The total length is estimated to be 18.16 m, while intermediate results are shown in Table 16:

Segment	S1	S2	S3	S4	S5	S6	S7	S8	S9
Length [m]	4.10	0.43	1.63	0.92	0.43	1.70	4.79	2.96	1.20

Table 16: Discretize segment length

In order to compute the required thickness for the structure to withstand the loads, the LV need to be discretized into segments with homogeneous mass distribution to evaluate stresses along the length of the system [6]. To refine the mass estimation obtained from the structural indexes ε_s , Mass Estimation Relations (MER) can be used in parallel with preliminary sizing of propellant and pressurizing gas tanks. The statistical relations require a first draft of the propulsive architecture, overall system mass and length and configuration choices. The results of the analysis after the iterative process are reported in Table 29 in Appendix I.

The typical mass of the parachute has been retrieved from the literature as reported in Section 2.4, while the fins mass has been estimated considering the average density of an honeycomb structure [31] and typical width and computed surface area. Furthermore, retrorockets are needed to guarantee a safe separation. Their weight has been estimated in Section 2.4.

As mentioned, an additional source of inert mass for the system is the pressurizing gas and the associated tanks. The choice of exploiting spherical shapes was due to multiple reasons: in first place, the sphere is the most efficient shape to withstand the loads while minimizing the mass [6]. Moreover, a single tank of pressurizing gas for each stage would have required to increase the length of the system to fit it, while dividing it into smaller parts allow to exploit the available empty spaces. It's underlined that the expansion behaviour will not be exactly the same as if one tank only will be present, which has been suppose to compute the required Helium mass according to the procedure explained in reference [7], thus refinements will be needed. The required thickness of the spherical tanks has been computed considering a FS of two and ultimate yield strength of the Ti-6Al-4V alloy of 950 Mpa [32] according to Equation 8.

$$t = \frac{P_{Hein} \cdot FS \cdot R_{sphere}}{2 \cdot \sigma_u} \quad (8)$$

The propellant tanks thickness has been initially selected as 1 mm of Al-Li-2195 as result of a preliminary sizing considering 2 bar of internal pressure and hydrostatic contribution supposing the LV under 6 g of axial acceleration [6]. This material guarantees better ROI with respect to Ti-based alloys, being easier to manufacture in large shapes while showing a better behaviour at cryogenic temperatures [32]. It is typically used in LV[6].

2.5.3 Launcher discretization

As visible in Figure 12, the system has been discretized into nine different segments, according to the following logic:

- The wiring mass has been allocated by computing a wire density per unit length [6], while the avionics

mass has been allocated 75% to the 2nd stage and 25% to the 1st stage [6].

- A 100% margin has been allocated to the wiring and avionic of the first stage. Since it has to perform recovery operations, cabling weight is expected to increase with respect to typical values. Moreover, the MER used in Table 29 was quite conservative with respect to other correlations found in the literature [6].
- Primary-structure weight estimated through MER has been added coherently with each segment length and within the context of structural propellant tanks.
- The weight of LRE, thrust structure, gimbal, pressurizing gas spheres associated to the RP1 tank and fins have been placed on the ninth segment.
- The eighth segment comprehends the RP1 tank until the top of the common bulkhead dome. The amount of propellant above that height has been considered anyway in this segment, introducing an additional approximation that slightly shifts C_g to the bottom.
- The LOX tank and insulation masses are instead fully placed in the seventh segment which is tangent to the dome's top.
- The sixth segment includes avionics, retro rockets, parachute mass and the pressurizing gas spheres for LOX.
- Similar considerations can be extended to the second stage segments from five to one.

The C_g of each segment is placed at the middle, supposing a uniform mass distribution [6], except from segment number six, which has been divided into a trapezoidal shape plus a cylindrical one and then the overall C_g has been computed. For segment number one the C_g has been instead retrieved after having divided the shape into a 1.5 m long cylinder plus the nose, approximated as a conical shape. This procedure allows to better approximate the centre of mass position, closer to the payload adapter. The centre of mass of the launcher is not fixed, but shifts in time as the propellant is consumed. The mass and C_g position of each segment is reported in Table 30 in Appendix I for relevant flight conditions. Sloshing of the propellant has not been taken into account. The C_g of the LV can be computed as stated in Equation 9.

$$C_g(t)^{LV} = \frac{1}{M_{tot}(t)} \sum_{i=1}^9 m_i(t) \cdot C_g^i(t) \quad (9)$$

The total mass of the system is estimated to be 20436 kg compared to the output of the trajectory design, of 20593 kg. This value will be further refined in Section 2.6 after a more precise analysis of the LV loads and critical stresses, that will allow to size the primary structure. Comments on the quality of the structural mass indexes assumptions done in the first place are reported in Section 2.6.

2.6 Structures

In order to size the primary structure and the structural tanks, a load analysis must be performed to determine which is the most demanding condition for the launch vehicle, thus sizing the structure accordingly. The most critical loads are the in-flight loads [6]. They are due to multiple causes:

- Thrust force producing acceleration.
- Aerodynamic forces, lateral and axial, proportional to the dynamic pressure.
- Control forces due to the engine gimbaling.
- Wind gauges that produce an angle of attack different from zero.

In addition to this primary loads, also secondary ones can be present, like vibration, thermal and acoustic, but they have not been taken into account for a conceptual design [6]. The loads are assumed to change slowly during the flight, such that the dynamic behaviour can be in first approximation neglected and the loads treated as quasi-static.

2.6.1 Critical loads conditions

The flight conditions that are usually analysed are max q , max $q\alpha$, MECO [6]. In addition, also the first burn during the recovery phase is considered, since the acceleration which the structure is subjected

to is about 6 g as reported in Section 2.4. Moreover, also the condition in which the launch vehicle is attached to the carrier is taken into account since it may be critical from the shears loads view point.

In principle it's not possible to say whether $\max q$ or $\max q\alpha$ is more demanding, thus calculation are done for both conditions. To recover shear, bending and axial loads in different conditions the procedure described in Reference [6] has been followed. The main logical passages are reported for $\max q$ condition:

- First of all, informations about $\max q$ have to be retrieved from the trajectory design. The most important parameter are reported in Table 17.
- The consumed propellant mass has to be computed in order to determine the position of the LV C_g knowing the engine mass flow rate and time of flight at $\max q$. Results can be seen in Appendix I.
- In order to analysed shears and bending moments, the instantaneous angle of attack must be known, thus the gusts speed had to be computed. The employed wind speed model is reported in Reference [6] and it's obtained from experimental data fitting. The proposed procedure supposed horizontal gusts, perpendicular to the launcher axes, in order to size for shears. It has been decided to conservatively assume the speed of upward and downward gusts equal to the horizontal ones, perpendicular to the body axes. This approach will overestimate the AOA. At $\max q$ the value of α is equal to 3.72 degree.
- Given the information in Table 17 and the AOA the values of C_N and C_A have been computed using the developed code, as explained in Section 2.7.2. The centre of pressure for the nose, interstage skirt and fins have also been evaluated.
- The aerodynamic forces can now be computed. Given the small value of α the contribution of the cylindrical shapes has been neglected [6].

h [km]	ρ [kg/m ³]	M [-]	n_x [g_0]	v [m/s]	q [kPa]
15.58	0.176	3.22	1.478	952	69.44

Table 17: Data @ $\max q$

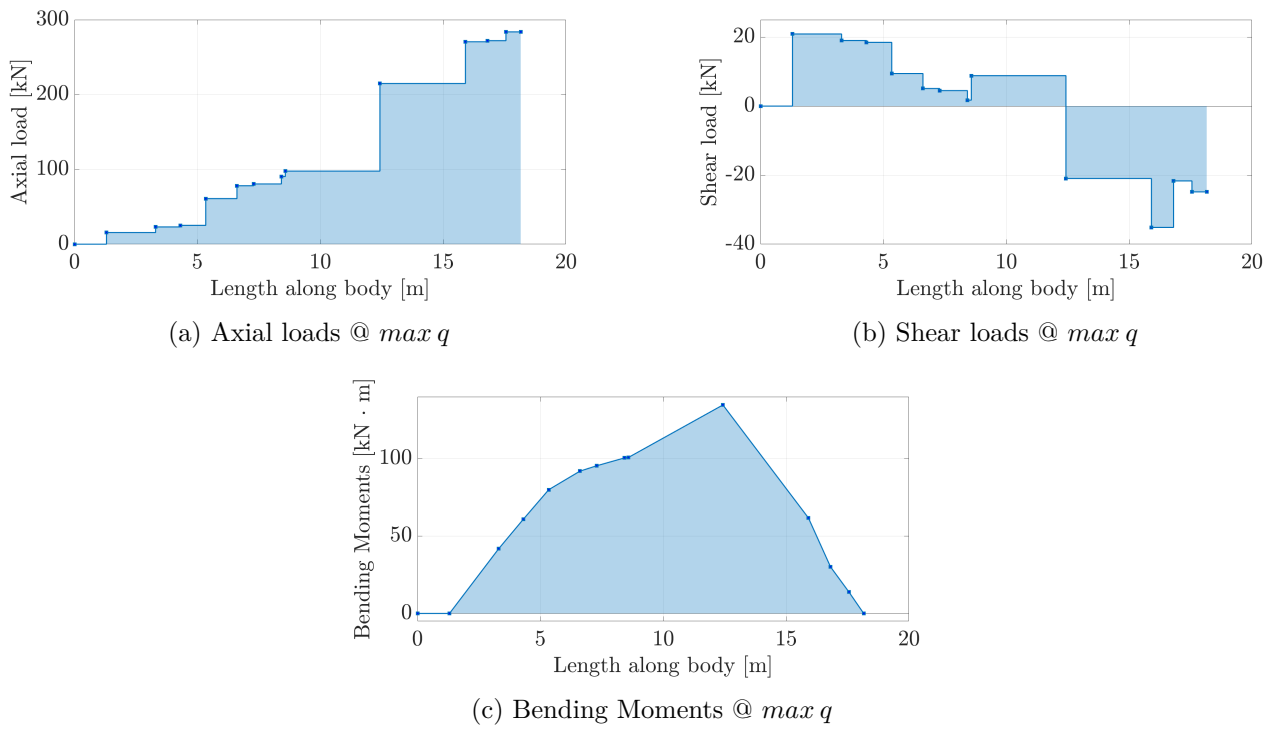
- The main effect of a non-zero angle of attack is the generation of forces perpendicular to the body axes, which require to trim the engine to maintain equilibrium of momentum around the centre of mass. It's clear that the computation of the deflection angle δ of the engine is a refinement with respect to the point mass model used in the trajectory design, which assumed a null angle of attack and neglected any trim problem. Given the centre of pressure and the normal aerodynamic forces, the required δ can be computed according to Equation 10, where the lever arm b_i are expressed with respect to c_g . Consequently to the trim, the thrust perpendicular to the body axes is 24.8 kN.

$$\delta = \arcsin \left(\frac{N_{skt} \cdot b_1 + N_{nose} \cdot b_2 - N_{fins} \cdot b_3}{b_4 \cdot T} \right) = 4.85 \text{ deg} \quad (10)$$

- The lateral acceleration n_z can be retrieved knowing normal aerodynamic forces and gimbal angle [6]. The former is equal to 0.57 g_0 , thus inertia relief forces are expected in the trim configuration.
- Shears loading can be computed starting from the nose [6] and consequently bending moments retrieved. To conclude, axial compression forces are derived, knowing the axial acceleration, thrust, mass distribution and aerodynamic forces. Discontinuities in the graphs are expected since forces are concentrated due to the modelling approach [6].

The results of the procedure⁶ are shown in Figure 13. The axial loads do not match perfectly the nominal thrust of 293 kN, but this is expected since the total system mass estimated with MER was slightly lower than the GLOM considered in the trajectory design. The shear at 18.16 m is -24.8 kN, which is equal to the normal component of the thrust due to the gimbal of the engine. Finally, the moments behaviour results coherent with the shears one, specifically it is zero at the beginning and at the end of the launcher, thus the equilibrium has been correctly enforced through Equation 10. The results can be considered validated when compared with the examples presented in Reference [6].

⁶Further details on the results for all the analysed cases can be found in Appendix J.

Figure 13: Load analysis results @ $\max q$

2.6.2 Analysis at $\max q\alpha$

The same procedure has been followed for the $\max q\alpha$ analysis. This condition may be critical because the aerodynamic forces are proportional to $q\alpha$. Some criticalities need to be addressed: the model used to estimate the winds is a piecewise function of h , thus $q\alpha$ curve presents net changes in the behaviour as time of flight increases.

Moreover, according to Reference [6], the maximum value of $q\alpha$ for a real launcher should not exceed 168 kPa · deg, thus the estimated value obtained with the implemented model of 350 kPa · deg may overestimate the load conditions, as expected. This discrepancy may be due to both the overestimation of AOA and the absence of control logic in the analysed case. Typically, the vehicle tends to align to the wind in order to relieve aerodynamic loads, accepting to lose precision in orbital insertion [6]. A summary of intermediate results for the $\max q\alpha$ condition is reported in Table 18, while more detailed explanation of the wind modelling and graphical representation are present in Appendix K.

h [km]	ρ [kg/m ³]	M [-]	n_x [g_0]	v [m/s]	q [kPa]	α [deg]	δ [deg]
13.00	0.27	2.53	1.42	746	60.30	4.83	4.87

Table 18: Data @ $\max q\alpha$

At MECO condition, only compressive axial loads have been computed, given the absence of wind gusts. The same has been done in the case of re-entry burn, given that the theoretical framework applied for shears computations is no longer valid. Finally, in the clamping case only shears and bending loads have been evaluated under the hypothesis of negligible axial loads. The reader is referred to Appendix J for these analysis results.

2.6.3 Structural analysis

The task of structural analysis is to select the materials and calculate the thickness of the primary structure, ensuring that the launcher can withstand all phases of the launch. In the present discussion, it is noted that the thrust structure, although part of the primary structure, has not been sized but only its mass has been estimated through MER. This is because it would require a more in-depth level of mathematical analysis than the current stage that the project allows.

In the case study, the structure is divided into two subcategories:

- Non-pressurized structure, including the first stage skirt, the interstage, the second stage skirt, the forward skirt and the fairing.
- Pressurized structure, consisting of the first and second stage tanks.

As explained in Section 2.6.1, the pressurized structure provides a significant structural advantage: the internal pressure generates a force that counteracts the loads to which the launcher is subjected.

The first step in structural analysis is the selection of materials. In modern rockets, the use of composite materials in sandwich-type structures is increasingly common due to the advantages in terms of mass reduction, especially for the unpressurised structure [6]. However, in this discussion, it was decided to use only isotropic materials. This choice is motivated by the fact that anisotropic materials exhibit a greater variety of failure modes compared to isotropic ones and would require a level of analysis beyond the conceptual stage of the project [33]. Additionally, thermal considerations both during re-entry and under cryogenic conditions, would pose significant challenges in the case of structures made from composite materials [6].

The material selection process led to the choice of the Al-Li 2195 alloy, which offers numerous advantages over other aluminium alloys. In particular, it stands out for its superior specific properties, good workability, competitive production costs, and good performance at cryogenic temperatures [34]. For a more detailed analysis of the material selection, the reader is referred to Appendix L. The mechanical properties of the Al-Li 2195 alloy are provided in Table 19.

σ_y [MPa]	σ_u [MPa]	E [GPa]	ν [-]	ρ [kg/m ³]
517	552	71	0.33	2720

Table 19: Mechanical properties of Al-Li 2195

The second step of the analysis involved calculating the thickness of the structure. Initially, the loads acting on each section of the LV during the most critical phases of the flight were determined, as described in Section 2.6.1. Subsequently, for each critical conditions, the required thicknesses were calculated to ensure that the structure can withstand axial, shear, and hoop loads, as well as resist buckling instability, the latter proving to be the most restrictive condition.

By solving the implicit Equations 28 and 29, applicable to cylindrical shapes, and Equations 30, 31, 32, applicable to conical and frustum shapes, such as the interstage and the nose (which was approximated as a cone), it was possible to calculate the structural thickness. For the mathematical procedure the reader is referred to Appendix M.

It should be noted that the sizing was performed considering the yield limit, as it was decided not to exploit the plastic regime of the materials to maintain a more conservative estimation and allow for reusability of the first stage. In particular the first stage must be reusable without replacing primary parts, in order to reduce the launcher refurbishment costs. Additionally, a factor of safety (FS) of 1.4 was applied [6]. This value represents the ratio between the maximum loads the structure can sustain and those estimated during the preliminary phase. The application of the FS is necessary to account for the approximations in the mathematical models used and to provide a margin of safety against unforeseen overloads.

The final structure was designed by selecting the maximum thicknesses taking into account each phase of the flight. These values are presented in Table 20. The mission condition imposing the highest loads on each section, thereby determining the wall thickness, corresponds to max $q\alpha$. A detailed breakdown of the thicknesses calculated for each launch phase is provided in Appendix M.

	Fairing	F.S.	LOX st ₂	RP1 st ₂	S. st ₂	Int.	LOX st ₁	RP1 st ₂	S. st ₁
t [mm]	1.4	1.6	2.1	2.2	1.9	2.1	2.8	2.5	1.8

Table 20: Launcher wall thickness

The final step of the structural analysis involved calculating the masses of the primary structure, which had previously been estimated using MER. The results are presented in Table 21.

	MER	Preliminary design
Stage 2 [kg]	225.625	148.517
Stage 1 [kg]	460.633	417.364

Table 21: Mass of the primary structure calculated using MER and preliminary design

Additionally, the structural indices hypothesized during the initial phase of the project were checked. The data in Table 22 show that the initial estimates are in good agreement with the values obtained through statistical approaches and preliminary sizing of the tanks and primary structure. The discrepancies fall within the typical margin of error for the preliminary phases of projects [35], confirming the reliability of the initial assumptions.

	Initial Estimation	Refinement
ε_{s1}	0.120	0.104
ε_{s2}	0.140	0.137

Table 22: Initial estimate of the structural index and the calculated value with preliminary design

Although the error results to be contained, the initial estimation of ε_{s1} appears to be overestimated. This outcome aligns with the conservative design choices outlined in Section 2.1. The GLOM of the system is finally estimated to be 20316 kg.

2.7 Aerodynamics

The aerodynamic design process begins with the preliminary definition of the shape relying on market data: during the initial phase particular attention is posed to defining $\frac{l}{d}$ ratio of the overall body and nose shape, together with possible lifting surfaces configurations. In this phase the possibility of implementing a lifting-body solution is considered but then discarded for two main reasons. From references of airborne launchers such as Pegasus XL [9] and Launcher One [10] approximate values of the maximum dynamic pressure exceed 21 kPa: beyond this value, benefits of lifting shapes are minimal or negligible. Enhanced lift performance of such geometries can turn to be advantageous over those phases distant from the q_{max} condition still representing a significant portion of the atmospheric cruise. Nevertheless, lifting bodies cross sections magnify the structural complexity of the vehicle since the structural relief of pressurized internal elements can be exploited only partially, thus impacting on global mission costs and compromising the ROI. Consequently, conventional circular section has been chosen as reference geometry of the launcher. The fineness ratio of the vehicle was preliminary set to a value of 12 inspired by the aforementioned airborne vehicles data, in order to define the rough aerodynamic and geometrical properties. The f_b has been progressively updated to 11.35 through successive iterations to include configuration necessities.

A custom code has been implemented for the estimation of aerodynamics performances of the launcher over the modelled flight phases. Air properties at the altitude station are computed according to the International Standard Atmosphere model through `atmosisa` MatLab® function. The reader is referred to Subsection 2.7.2 for detailed information about the retrieved results and code validation.

2.7.1 Nose

The Haack Series nose shapes are mathematically derived with the purpose of minimizing drag [36]. In particular, the Haack-Von Karman ogive minimizes drag for a given length and diameter. The results reported in Reference [37] indicate that the Von Karman profile presents low drag over most of the Mach number range, especially within the transonic and high supersonic regime, making this solution suitable for our airborne purposes.

Note that the Haack series nose cones are not perfectly tangent to the body at their base; however, the discontinuity is usually so slight as to be imperceptible. Likewise, the Haack nose tips do not come to a sharp point but are slightly rounded, offering advantages in terms of both shock tip detachment and thermal loads relief. Moreover, the Von Karman shape allow the fairing to be more space efficient in terms of envelope volume where to locate the payload with respect to well known conical profile,

representing the best compromise between aerodynamic performance and enclosed volume capacity.

The fineness ratio of the nose f_n has been iteratively set to 2 in order to guarantee reduced drag resistance and sufficient space for payload allocation as well. The nose length refinement process has been based upon the minimum volume required to house a 400 kg payload mass extrapolated from the literature of similar nominal payload capacity launch vehicles. Table 23 includes the main parameters ruling the envelope volume to payload mass ratio considered for the nose sizing roughly esteemed from the literature.

	Envelope volume [m ³]	Ref payload mass [kg]	$\frac{V_{env}}{m_{pay}}$ [m ³ /kg]
Pegasus	2.212	280	$7.9 \cdot 10^{-3}$
Launcher One ⁷	4.355	500	$8.7 \cdot 10^{-3}$
Electron	1.210	200	$6.1 \cdot 10^{-3}$

Table 23: Envelope volume to payload mass ratio of existing launch vehicles [9, 10]

As can be seen from the reported values the aforementioned ratio tends to increase with the payload mass to be installed. Nonetheless the considered pool of data is too restricted to extrapolate a significant trend. Consequently, a ratio of $8 \cdot 10^{-3}$ has been taken as reference since it is closer to the Pegasus' whose nominal payload mass roughly match the requirements one. Considering 400 kg of payload mass the minimum volume to be ensured for payload results to be 3.2 m². Further considerations about the payload space management can be found in Section 2.5.

2.7.2 Aerodynamic coefficients

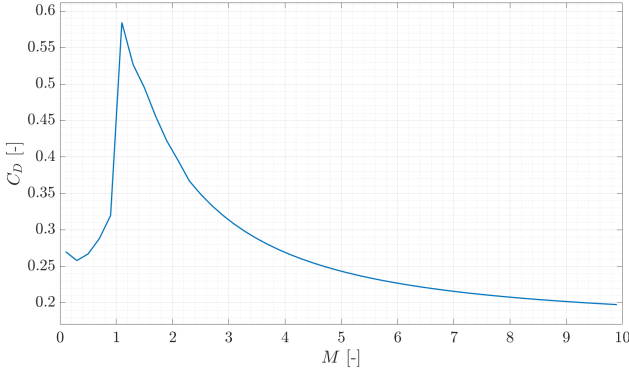
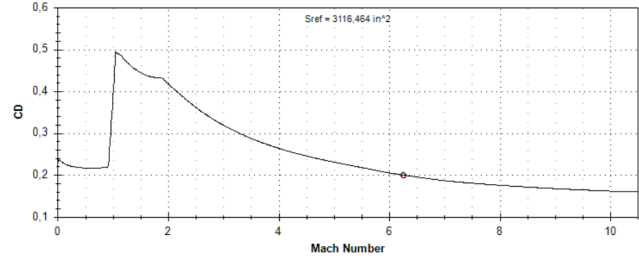
The Jorgensen method [38, 39, 40] represents a valuable theory for the preliminary estimation of the launcher aerodynamic performances, even considering complex shape geometries, for a wide range of angles of attack. It follows a component build-up approach where the various contributions of the single elements such as the nose, fuselage, and wings are considered singularly and summed up together, accounting for mutual regions interaction thanks to correction factors. Moreover, the method adapts to subsonic, transonic and supersonic regime combining intuitive fluid dynamics theories with experimental results, making it well-suited for preliminary design stages or for analysing conventional missile and projectile shapes such the presented one.

Even if the aforementioned approach results to be fairly accurate for the overall coefficient computation, it does not allow to distinguish from single normal force coefficient of the components. This information, instead, is crucial for the launcher structural sizing. For this reason, it is decided to integrate other estimation models to size the aerodynamic behaviour of specific elements such as fins, nose and skirt, especially for what concerns the C_N prediction. The Jorgensen method still remains the reference approach for the computation of the body alone geometry normal coefficient since its suitability for body of revolution with variable cross section such as a multi stage launcher [38]. Detailed theories and relations exploited for code implementation are reported in Appendix N.

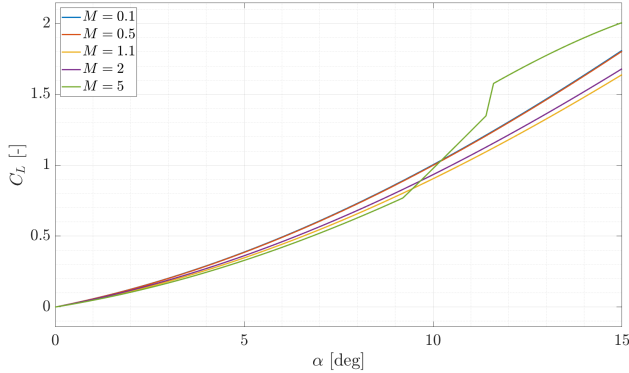
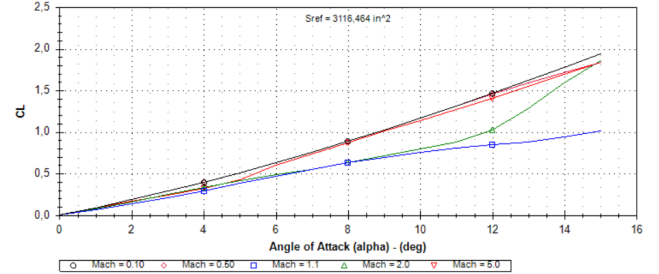
The aerodynamic coefficients computer has been validated comparing the results with RASAero II software estimations. RASAero is a versatile tool employed for aerodynamic analysis of model rockets able to produces reliable simulations for space launch vehicles as well. More about the software documentation can be found in Reference [41].

Figure 14 and 15 shows how the implemented algorithm matches quite accurately the values returned by RASAero. The main differences between the illustrated C_{D0} trends can be imputed to base pressure modelling through Gabeaud theory. This approximation implemented in our algorithm is based upon the assumption of void behind a cylindrical blunt body that leads to an overestimation of the effective base pressure drag during flight condition. Nevertheless, since the present work aims to recreate a concept design phase, a conservative esteem is preferable in order to account for certain sizing margins.

⁷Launcher One maximum weight capacity has been considered since the same envelope configuration is employed for all types of payload.

(a) Custom code C_{D0} (b) RASAero C_{D0} Figure 14: C_{D0} comparison

With regards to C_L graphs, the carried out comparison has been limited to small angles of attacks since both the aforementioned software and the in-house code retrieve some of the components C_N through models presenting the same validity restriction.

(a) Custom code C_L (b) RASAero C_L Figure 15: C_L comparison

The implemented code tends to exceed the overall lift coefficient prediction within transonic flow regime, showing higher accuracy for subsonic supersonic Mach values. Likely, this is due to the fact that the Jorgensen method bases C_N estimation on interpolation of experimental values of cross flow drag coefficient C_{d_n} of a two-dimensional cylinder taking into account the increment of drag resistance typical of transonic conditions [40], as can be seen from the slope discontinuities at $M = 5$. Nonetheless, this flight phase represents a small section of the whole atmospheric cruise, marginally influencing the mission accomplishment.

2.7.3 Tail fins

Four fins are placed at the rear end of the first stage with the aim of improving the stability of the launcher as further reported in Section 2.8. A clipped-delta shape is chosen to grant higher structural robustness and reduced drag compared to other fin geometries [42] while the shape of the airfoil is set to a modified double wedge to add strength and stiffness to the section while still retaining high aerodynamic efficiency in supersonic flows [43]. A geometrical representation of the fin can be found in Appendix Section N.4.

The fins contribution to the launcher aerodynamics is firstly modelled according to thin airfoil theory as described in Reference [8]. While the results obtained prove already satisfactory when compared to those obtained through RASAero, further refinements are applied to enhance accuracy and account for the geometric characteristics of the fins.

To this end, an improved computation methodology is introduced, following Barrowman approach both for subsonic and supersonic flows [44]. A detailed description of both the adopted approaches is reported in Appendix N. The difference in results is highlighted in Figure 16.

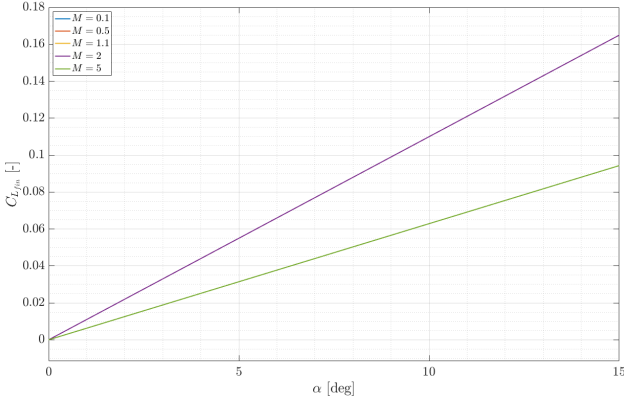
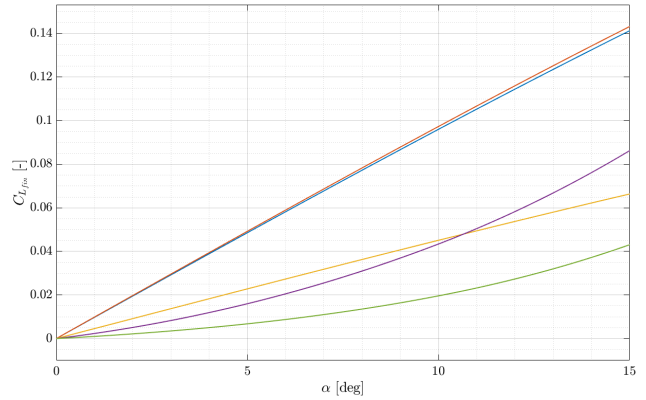
(a) First iteration fin C_L (b) Second iteration fin C_L

Figure 16: Comparison in first and second iteration results

It's possible to observe that the results obtained applying thin airfoil theory collapse onto the same plot line for almost all values of Mach number while Barrowman's approach allows to better capture the behaviour of the fins in the different velocity regimes and overall provides a more accurate evolution of the aerodynamic coefficients for varying values of angle of attack.

Finally, to incorporate the contribution of the fins into the computation of the total aerodynamic forces, an interference factor is introduced to account for the mutual interaction between the body and the fins. The fins' effect is then included as follows: the total lift is calculated by considering the contributions of two fins, while the total drag is computed by accounting for the combined effects of all four fins.

2.8 Static stability and control

The launcher center of pressure is mainly ruled by the tail fins geometrical properties presented in Section 2.7.3, that have deliberately been undersized to obtain an intrinsically unstable configuration. The manoeuvrability of such a launch vehicle does not appear to require particularly unstable conditions since the manoeuvres to be accomplished during the flight phase do not present steep curvatures. Nevertheless, an airborne launcher configuration of this kind allows to obtain a non-null pitch-up angle thanks to a spontaneous rotation occurring between the launcher detachment and the end of the free-fall phase. This initial launcher orientation results to be closer to an equilibrium configuration to be guaranteed at engine ignition in order to match the initial flight-path angle $\gamma_0 \approx 0$ deg and reconnect to the retrieved optimal trajectory. On the other hand, launcher control feasibility must be ensured and verified over critical flight phases. Detailed analyses of the aforementioned cases are presented in the following sections.

The vehicle's stability assessment was conducted using RASAero II software, which estimates the center of pressure position (c_p) based on Rogers' modified Barrowman theory. As stated in Reference [41], this model produces a more accurate body normal force slope $C_{N\alpha}$ at low angles of attack by accounting for the influence of the body cylinder, the fins interference factor and body viscous crossflow using the Jorgensen Method for the forward movement of the rocket center of pressure with angle of attack. As for the aerodynamic coefficient prediction, the software integrated model is limited to low values of α for all the flight regimes. Moreover, the forward movement of center of pressure at high supersonic to hypersonic Mach numbers is predicted up to Mach 5.

These various considerations led to further research on the active control authority strategies to be adopted. Movable surfaces effectiveness has been preliminary examined through straightforward computations based on the lift coefficient increment given by their deflection. According to Reference [45], considering a tail fin flap which chord length is 0.25 of the fin chord and a deflection angle of 20 deg around its hinge, the fin lift increases up to 10%. This result proves to be definitely insufficient to counterbalance the launcher fuselage destabilizing aerodynamic moment. The effectiveness of lateral thrusters can instead progressively decrease due to the c_m shift towards the nose if placed in forward locations and would require dedicated gas generators. For these reasons, a TVC appears to be an optimal choice to guarantee proper control authority and its feasibility has been studied in Section 2.8.2.

2.8.1 Static stability margin

The data extrapolated through RASAero for each Mach condition up to $M = 5$ have been interpolated to retrieve a c_p shifting trend⁸ over the atmospheric cruise. Altitudes and Mach number at each station are computed according to the reference trajectory discussed in Section 2.3. These values have been then compared to the center of mass shift over time to retrieve the static margin variation during atmospheric flight. Figure 17 illustrates these parameters evolution over time from engine ignition.

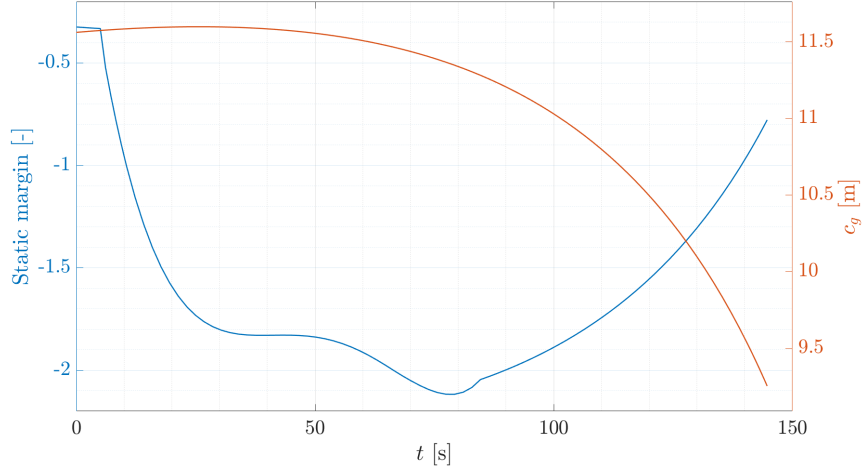


Figure 17: Center of mass and static margin shift over atmospheric flight

Excluding the maximum dynamic pressure point where the contribution of aerodynamic forces is maximum, the graphs underlines another critical point for stability assessment occurring at approximately 79 s when the static margin reaches its lowest value.

2.8.2 Equilibrium and stability assessment

Detailed analysis of equilibrium configurations over the most critical flight condition has been carried out through a point 3-DOFs representation. Three relevant points are identified over the trajectory path: engine ignition where high values of α occur, at $\max q$ where aerodynamic forces can increase dramatically and at minimum static margin condition where lift moment can result to be unbalanced. Specifically, vertical and moment equilibrium has been imposed to retrieve the required value of TVC gimbal tilt δ and angle of attack α to ensure launcher steadiness along the vertical direction and about the pitch axis. In reality, the pitch-up manoeuvre should dictate a vertical acceleration of the launcher as well as a rotation of its reference axis. However, this requires a more detailed analysis of the system slow loop control that has been left as an open point for further design phase assessments. Table 24 illustrates results obtained from the non-linear system of equations describing equilibrium. Further considerations about the implemented equations and reference parameters are presented in Appendix O.

	Engine ignition	Max q	Min static margin
α_{eq} [deg]	27.2	4.92	3.18
δ_{eq} [deg]	1.13	4.63	1.68

Table 24: Equilibrium values for gimbal tilt angles and angles of attack

As shown, δ remains contained within acceptable operability limits for all the critical flight conditions [6]. It is necessary to remark that both aerodynamic coefficients and c_p result accurate within limited range of α , thus leading the equilibrium condition at engine ignition to be roughly predicted with increased error margins. The equilibrium conditions retrieved have then been perturbed, considering typical wing gusts velocities at each point altitude [6] altering the angle of attack and consequently provoking a destabilizing effect. A new thrust deflection angle is required to avoid the pitch angle to diverge irreversibly. Table 25 includes δ_{pert} values to guarantee the equilibrium together with the time-to-double t_{double} which

⁸ c_p for Mach values higher than 5 is considered constantly equal to $c_p|_{M=5}$.

characterizes the response time of the control system in such perturbed cases.

	Engine ignition	Max q	Min static margin
α_{pert} [deg]	45.7	8.66	4.19
δ_{pert} [deg]	2.42	9.95	2.37
t_{double} [s]	1.3	0.66	1.3

Table 25: Perturbed AOA and relative δ required to avoid rotation with associated time-to-double

It is necessary to remark that gusts were considered perpendicular to the launcher axis over each configuration, generating the maximum α deflection in order to obtain conservative esteems. Nevertheless, it is unlikely that gusts orientation would match exactly the hypothesised cases. Also under such perturbations, δ remains within TVC typical operability range preserving some room for additional deflection to correct the launcher orientation. However, the $maxq$ seems to require particularly steep deflection angles, dangerously approaching their limit value. From this point of view, the implementation of other effectors such as lateral thruster or movable aerodynamic surfaces can relieve this margin. Moreover t_{double} stays above 0.5 s, confirming that the TVC system does not require enhanced performance response time [6].

2.8.3 Free-fall pitch-turn

As shown in Table 24, the initial equilibrium angle of attack coinciding with the pitch angle proves to be quite high. A stable configuration would hinder the rotation leading the launcher to orient its axis towards the velocity direction bringing the engine to ignite at an improper orientation. The implemented instability, instead, aids the launcher pitch-turn during the 5 s free-fall phase which duration has been set considering similar airborne launcher operations [9, 10].

Considering typical Boeing-767 maximum climb angles that can be derived from aircraft datasheet values, an admissible pitch-up angle of 13.5 deg has been considered at launcher detachment [3, 46]. Right after the detachment, a carrier evasive manoeuvre needs to be performed⁹. A 3-DOFs simplified model, including rotational and translational equations of motions, has been implemented to simulate the free-fall dynamics starting from the aforementioned initial condition. The outcome of this analysis is presented in Figure 18.

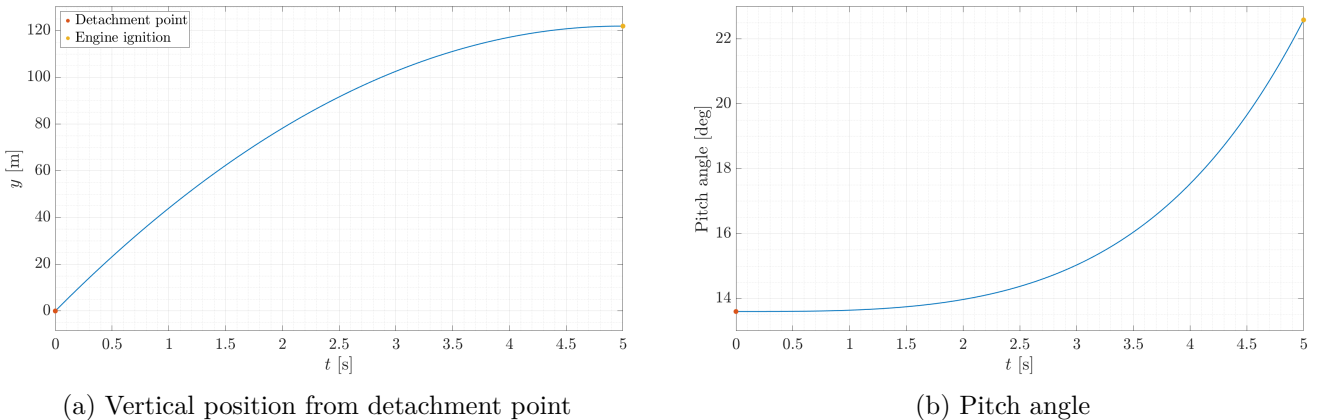


Figure 18: State parameters variation during the free-fall

Graph 18b shows how the designed fins configuration allows to obtain a desired pitch-turn to approach the initial equilibrium condition as close as possible without overshooting the required pitch-angle value. On the other hand, the presented results must be considered approximative since the considered c_p has been extrapolated within the Rogers' corrected Barrowman model α validity range. Most likely, a more complete and accurate trajectory analysis would lead to other optimized path, requiring different stability configuration. Nonetheless, the investigated launcher condition represents a valuable solution to optimize the free-fall phase without compromising the trans-atmospheric flight as well.

⁹The design of this manoeuvre has not been carried out. Nevertheless, considering such an aircraft typical flight envelope [47], it can be reasonably considered accomplishable.

3 Sensitivity analysis

3.1 Uncertainty population

A Monte Carlo simulation is performed to assess the variability in the insertion performances. The first step is to define the variables affected by a statistical uncertainty modelled following a Gaussian distribution. Initially a large survey on a total of 7 parameters is conducted: the initial release conditions (v_0 , h_0 , γ_0) and of some of the energetic terms (I_{sp1} , I_{sp2} , m_{prop1} , m_{prop2}). The statistical values of 3σ required to generate these populations are set to have a range of 2% for the propellant masses, 0.5% for the specific impulses, 5 m/s for the initial velocity, 3 deg for the initial pitch angle and 250 m.

σ_{v_0} [m/s]	σ_{γ_0} [deg]	σ_{h_0} [m]	$\sigma_{I_{sp1}}$ [s]	$\sigma_{I_{sp2}}$ [s]	$\sigma_{m_{prop1}}$ [kg]	$\sigma_{m_{prop2}}$ [kg]
1.67	$1.745 \cdot 10^{-2}$	83.33	0.5383	0.5600	98.76	9.11

Table 26: Standard deviations expressed as a percentage of the mean value

The uncertainty in the release condition is relevant but difficult to be estimated without a real control system needed to properly simulate the free-fall manoeuvre. In addition a second problem arises when the number of variables is increased; limiting the population size is necessary to achieve a computationally viable code. For this reason the first analysis is conducted on a small population of only 10 elements for each variable for a total of 10^7 terms initially created and then shuffled to monitor the method's convergence. In a later stage of the analysis a second study is conducted only on the energetic terms allowing for a larger population to be kept into consideration. This leads to a better-behaving solution in terms of achieving a smaller standard deviation in the insertion errors.

3.2 Orbit insertion accuracy

Energetic analysis In the case with the larger population of 55 elements, the mean errors and standard deviations are within reasonable bounds due to the fact that the initial release conditions are fixed to nominal values found in the optimization process. The mean values of the Monte Carlo are close to the target ones and the amplitude of the curve resembles a Gaussian-like distribution. However the standard deviation on the error of the final height still exceeds the threshold of 10 km in the precision tolerance.

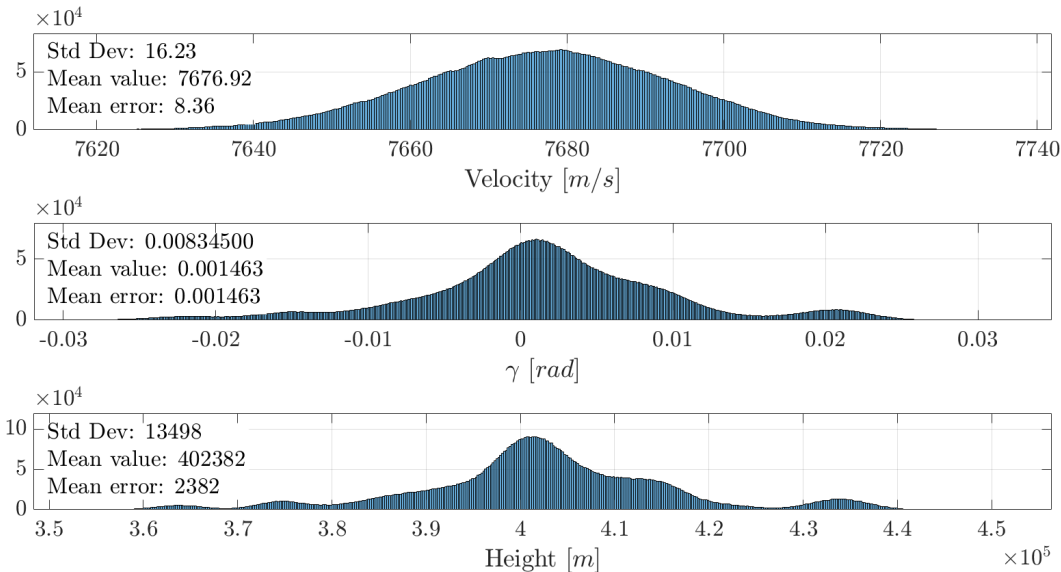


Figure 19: Monte Carlo energetic analysis results

General analysis The size of the population can significantly influence the observed standard deviation in the results. When the population size is small, the selected sample may not adequately represent the probability distributions of the parameters, increasing the chance that a single outlier or extreme value will cause a disproportionate effect on the statistical measures. Contrarily, as the population size

increases, the sampling distribution of the estimator approaches the true distribution, thereby reducing the impact of random fluctuations and leading to more accurate estimates of both the mean and the standard deviation. Thus, enlarging the population size generally improves the robustness of the results, enhancing their reliability and reducing the overall variability introduced by the parameters.

Increasing the population size could mitigate this issue to some extent, although introducing additional parameters inherently increases overall variability. In particular, the parameters v_0 , h_0 and γ_0 appear to significantly worsen data dispersion, especially given that no closed-loop control mechanism is implemented at this initial stage of the project.

As a consequence, the mean error is larger than anticipated, as the simulation results are highly sensitive to variations in the initial conditions. Moreover, the mean values deviate from the intended targets, indicating that the current population is too small to approximate the expected Gaussian distribution of the errors.

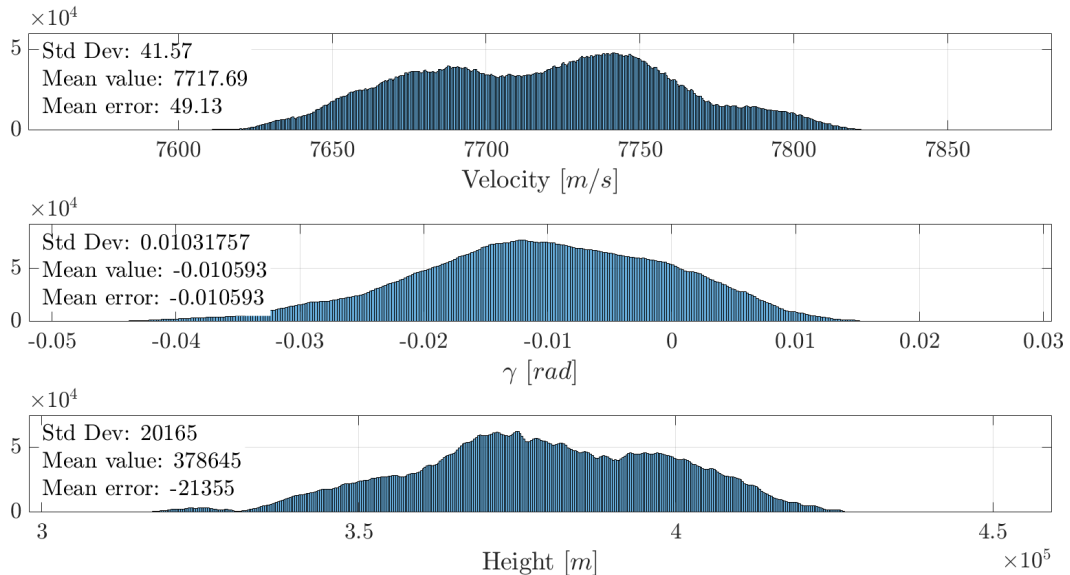


Figure 20: Monte Carlo general analysis results

4 Further developments

4.1 Trajectory advancement

A further development in the trajectory design should keep into consideration more precise models of the atmosphere along with aerodynamic coefficients interpolated at each height and Mach number to create a more realistic environment. However, this would lead to a computationally heavier code which could be a relevant issue without having the necessary computational power at disposal. Additionally, it would also be beneficial to transition to a higher DOFs model considering a non-planar problem to represent the out-of-plane correction of the initial velocity due to Earth's rotation. Finally, within this new framework, thrust vectoring can be exploited to achieve better manoeuvrability, along with a non-null AOA. This approach addresses the assumption of ideal control with a fixed $\dot{\gamma}$ by incorporating an actual dynamics ruling the rotation on the pitch axis.

4.2 Thermal analysis during Re-entry phase

During the re-entry phase of a reusable first stage launcher, the vehicle undergoes significant thermal and aerodynamic stresses. The retro-propulsion manoeuvre is a crucial step to decelerate the vehicle and mitigate the thermal flux and mechanical loads caused by interaction with the atmosphere.

Below are the main parameters and findings influencing thermal protection design, along with optimization strategies based on numerical studies from existing literature.

The key parameters influencing thermal stress are altitude and Mach number during engine reignition,

material properties and wall thickness, engine configuration and plume dynamics. Their analysis along with strategies for optimization are discussed in detail in Appendix P.

For the next design phase the following steps should be performed:

1. Conduct CFD simulations to refine predictions on heat flux distributions, including effects of turbulence and afterburning.
2. Evaluate TPS (thermal protection system) materials for high-temperature regions, prioritizing low density and high thermal stability.
3. Test alternative engine configurations to optimize plume dynamics and reduce thermal loads on sidewalls.

4.3 Re-entry

In a more advanced level of design, a tight control on the boostback phase must be considered especially regarding the throttle and the orientation of the stage during the firing. Moreover, the timing of the second burn must be carefully considered, as the window of maximum effectiveness appears to be quite narrow. Another critical factor to consider in the future is the shock transmitted to the structure during the impact with water. The re-entry phase has been designed to withstand accelerations up to 6 g, it is essential to verify that this requirement is also met during this stage. Paper [18] suggests that with a velocity of 9.7 m/s and an inclination of 10 deg, peak landing loads below 6 g might be achievable. However, these results pertain to a different class of launch vehicles, so a more detailed and specific analysis will be necessary in future studies.

4.4 Aerodynamics and control

As mentioned in Sections 2.7.2 and 2.8, the tools employed for aerodynamic performance estimation and stability analysis exhibit a limited range of validity in terms of AOA. Nevertheless, these tools have been utilized to analyse the free-fall dynamics and the engine ignition phase, where the pitch-turn results in particularly steep inclinations of the launcher axis with respect to the wind, even without considering gusts. Furthermore, the shift in c_p with variations in angle of attack cannot be predicted using the Barrowman model, at least for values of $\alpha > 10$ deg [44]. Consequently, the conclusions drawn at this stage are somewhat inaccurate and should be refined using alternative models. The Jorgensen theory remains a reliable starting point for body aerodynamic considerations, as its validity extends to high α . However, the aerodynamics of lifting surfaces, such as tail fins, require a far more complex physical framework to be accurately seized. To enhance aerodynamic predictions in terms of both performance and center-of-pressure accuracy, CFD analyses should be conducted in subsequent phases of the project, once the launcher geometry has been finalized.

With regard to control authority, the launcher instability has been shown to be manageable even during the most critical flight phases. However, such a configuration will require additional precautions and further development, as control requirements must be more stringent. For example, TVC alone does not allow for corrections during the free-fall phase, necessitating the implementation of other types of control effectors to ensure sufficient control authority over this mission segment. Furthermore, neither slow control loop dedicated to optimal flight path chase nor the fast control loop for stabilizing purpose have been properly designed in this preliminary phase. Nonetheless, the point equilibrium and stability analysis showed no particularly sensitive conditions, leading to reasonably conclude that the implementation of vertical and angular acceleration provided by control system should not introduce criticalities.

Lastly, tail fins geometric properties has been inspired by typical pre-existing cases [42, 10] and have not been assessed in terms of stresses and other aeroelastic phenomena such as flutter. Consequently, their shape may have to be corrected by considering the output of a more accurate structural analysis, once more details about materials and structural configuration will be available.

5 Conclusion

The output of the conceptual design is the first draft of the launch vehicle. With a gross lift off mass of 20316 kg and a length of 18.16 m the system is capable of bringing 250 kg of payload to a 98° SSO exploiting in-house designed LOX-RP1 engines in a two stage to orbit configuration. The trajectory design allows for a first stage separation at 87.3 km altitude and 2.9 km/s velocity, throughout a multi-stage optimization simple shooting problem. The recoverability of the first stage required a boost back before opening the parachute, to limit the loads on the structure. Through the design the most critical flight loads have been analysed in order to size the primary structures, with $\max q\alpha$ being the most demanding condition. A custom code has been developed for the aerodynamic coefficients computation, providing accurate results when compared with available commercial softwares. Four tails fins ensure a controllable configuration over the critical flight phases, including also TVC contribution. Given the size of the LV the possibility of being carried by the selected aircraft has been assessed.

A Monte Carlo analysis has been performed to asses orbit insertion accuracy through uncertainties propagation. ROI has been validated via preliminary cost analysis, while market readiness in 4 years via TRL roadmap for the engine and considering COTS components.

5.1 Criticalities

The primary criticality of the mission lies in the exclusion of Earth rotational velocity from the trajectory simulation. Since the LV will be released at a higher longitude than 55°52'19"N, the Earth rotation contribution has a maximum value of $v_{\oplus} = 260$ m/s, thus minor changes in the LV configuration and masses are expected in order to match the updated energetic requirement. Additionally, the trajectory will have to be further refined and verified accounting for a more detailed estimation of the C_D . Finally, a more comprehensive thermal analysis must be integrated to accurately model conditions during the re-entry phase.

Regarding structural analysis, further refinement is required in the evaluation of buckling stability. Lastly, in successive iterations, it will be essential to establish rigorous control mechanisms for both the ascent phase (encompassing free-fall and pitch-up) and the re-entry phase.

The dedicated Section 4 has been included to address potential resolutions comprehensively.

5.2 Requirements satisfaction

As final analysis, the requirements matching is investigated here in Table 27:

Req ID	Solutions addressed	Satisfaction level
F-0001	Ensuring accelerations lower than 6 g, exploiting boost-back and parachute.	Satisfied
F-0002	Achieving high insertion accuracy and performing Monte Carlo analysis, but unrefined trajectory assumptions.	Partially satisfied
F-0003	Civil aircraft selection and pitch-up manoeuvre feasibility assessment.	Satisfied
F-0004	Tandem configuration with tail fins and stability grids.	Satisfied
F-0005	First stage recovery ensured in the ocean and second stage de-orbit manoeuvre.	Satisfied
F-0006	Evaluation of engine TRL evolution, off-the-shell components and already proven technologies.	Satisfied
F-0007	Two stage solution and recovery leg loads minimization. Expensive booster fly back can be improved.	Partially satisfied

Table 27: Requirements satisfaction

Authorship declaration

Team member	Role
Bianchini Giulia	Aerodynamics
Ceglie Francesco	Stability and control
De Carli Matteo	Launch platform, Recovery
Mapelli Michele	Cost analysis, Recovery
Paniz Alberto	Propulsion, TRL, Monte Carlo analysis
Piemonte Francesco	Staging, Configuration, Structural analysis
Piraccini Mattia	Trajectory, Monte Carlo analysis
Portantiolo Matteo	Project Manager
Proserpio Andrea	Staging, Configuration, Load analysis

A House of Quality

Figure 21 shows the starting point of the conceptual design: the House of Quality.

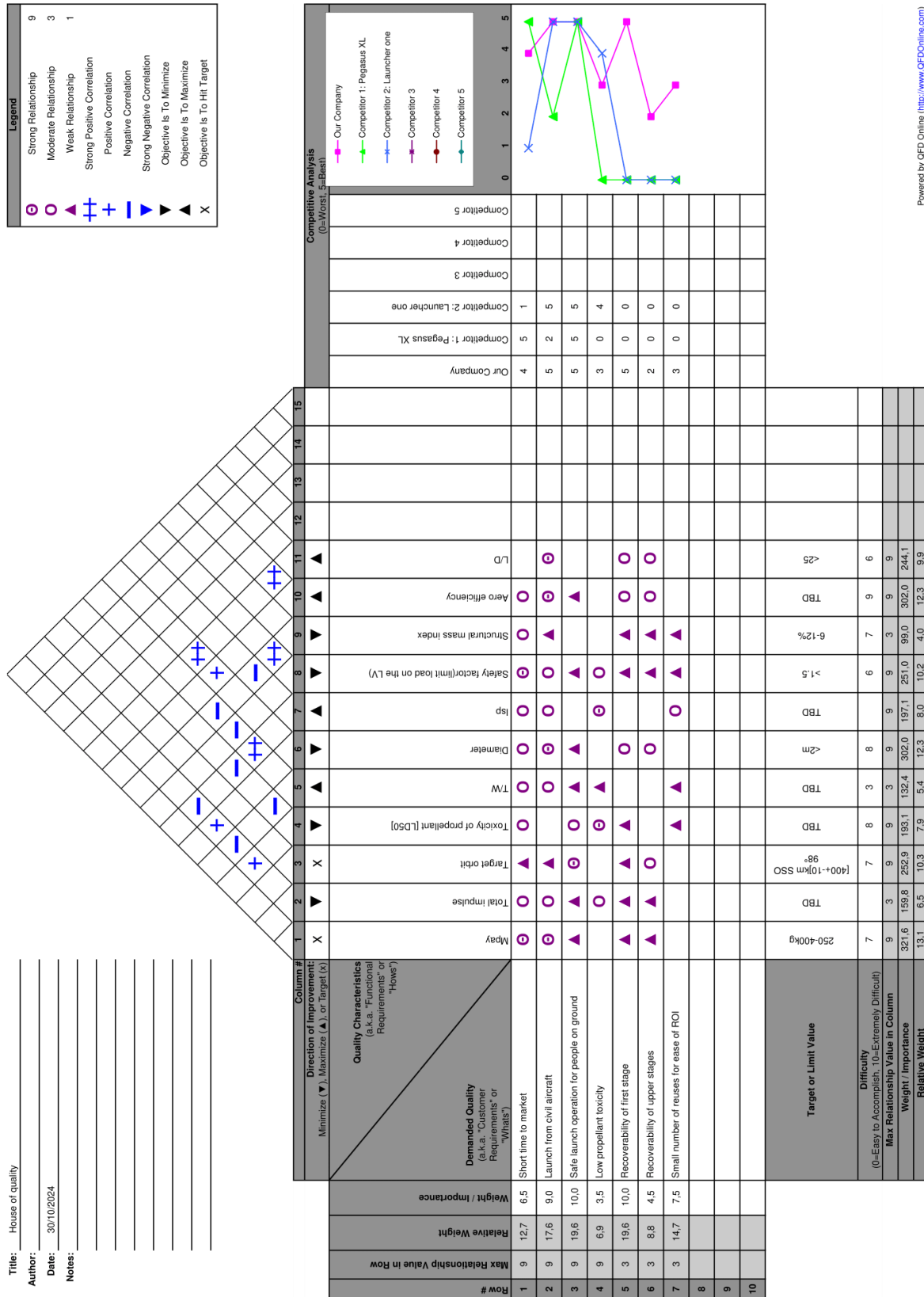


Figure 21: House of Quality

B System level requirements

Table 28 collects all the system requirements derived from the high level ones.

Req ID	System level requirement
F-0001	Stage recoverability and reusability shall be considered for the first stage
D-STR-0001	The stage shall be designed with materials and structural components that can endure multiple flight cycles
E-STR-0002	The stage's thermal protection system shall allow critical components to withstand peak temperatures encountered during ascent, re-entry, and landing with minimal damage
E-STR-0003	Other stages should be recoverable and reusable and should sustain thermal and mechanical loads during the re-entry
M-STR-0004	The recovery system shall be reliable
D-STR-0005	Redundancy of the recovery system should be taken into account
M-STR-0006	The recovery systems shall be able to ensure a touchdown velocity below 10m/s
V-STR-0007	Verification of successful recovery shall be performed after each launch to guarantee that the damage sustained by the stage remains within prescribed limits
L-0001	First stage and recovery shall be designed to require minimal operations for rapid turnaround and re-launch readiness
L-0002	The recovery shall be designed to ensure the recovered stages land in a controlled, accessible location
F-0002	Launcher shall be capable of bringing payload to LEO orbit
M-0001	Orbit insertion accuracy shall have an uncertainty of maximum 10km
M-0002	The system shall be capable of bringing max 400kg of payload mass
M-0003	The system shall be capable of bringing at least 250kg of payload mass on a 400 km SSO 98 deg orbit
M-0004	Launcher shall be capable of performing a pitch-up maneuver
M-0005	Last stage shall be re-ignitable to ensure accuracy
P-0001	The fairing internal space shall be compatible with the payload volume
D-0001	The last stage shall be capable of releasing the payload safely in space
D-STR-0008	The launcher shall avoid critical stresses/accelerations/vibrations that can damage the payload ($a_{max} = 5g$ from customer need)
F-0003	The system shall be airborne from civil aircraft
P-0002	The system dimensions shall be compatible with the carrier
P-0003	The system shall have wet mass compatible with the carrier
D-0002	The carrier and the launcher trajectories shall comply with the airspace regulations of the countries interested by the mission
M-0006	The aircraft shall be able to perform a safe evasive manoeuvre
E-STR-0009	The launcher shall withstand all operational mechanical stresses, including vibrations and accelerations, that may be experienced during takeoff, flight, and release phases from the carrier
I-0001	The launcher deployment system shall be reliable and shall be designed to minimize impact on the carrier's stability and flight dynamics during and after launch
F-0004	The launcher shall be in a tandem configuration
I-0002	Stage separation shall be reliable
M-0007	The second stage shall be able to ignite

Req ID	System level requirement
D-0003	First stage engines shall provide 323s of specific impulse, second stage engines shall provide 336s of specific impulse
M-0008	After separation, the first stage shall return to Earth
M-0009	After separation, the other stages should return to Earth within a time limit
D-0004	Every stage should be optimized for its operating altitude
D-0005	Stages should be designed to minimize the overall mass
D-0006	Stability should be ensured for all the stacks, with particular focus on the detachment of stages
D-0007	The first stack shall be aerodynamically stable
F-0005	The operations shall be safe for people on ground
M-0010	The ascending phase shall avoid inhabited regions
M-0011	The system shall be designed to avoid the risk of debris impact on populated areas in case of in-flight anomalies
D-0008	Trajectory re-entry shall end in a target area within a certain accuracy
D-0009	Self-terminating procedure shall be taken into account in case of trajectory control lost
D-0010	Procedures to ensure the system safety in case of launch delay shall be implemented
D-0011	The launcher should be designed to minimize potential toxic substance release
D-0012	The trajectory should include predefined emergency landing paths that prioritize safety over densely populated areas
F-0006	The system shall include technologies that allow acceptable time to market
L-0003	Off-the-shelf components shall be favorite
L-0004	TRL level of common components applied to new context shall be reassessed
O-0001	The chosen components should be available from different manufacturers
O-0002	The design process should be flexible to changes in the availability of the components
F-0007	The system shall include technologies that allow acceptable number of reuses to breakeven
M-0012	The recovery systems shall be driven by small number of reuses for ROI
D-0013	The recovery system shall maximize the number of reuses
L-0005	Refurbishment costs shall be lower than production or purchase costs
O-0003	The operational cost for landing operation shall be minimized
L-0006	The transportation and maintenance costs shall be minimized
V-0001	The testing cost shall be minimized
D-0014	The main engine reusability shall be prioritized
D-0015	Expensive component reusability shall be prioritized
D-0016	The turnaround time shall be minimized
O-0004	The recovery operations shall be as fast as possible
V-0002	The design should consider full compatibility with the recovery vehicle
L-0007	Maintenance operations shall be properly programmed
O-0005	The design shall allow fast and easy maintenance operation
E-0001	The design shall provide good protection from external contaminants
D-0017	The safety margin should be increased to grant reliability at each flight

Table 28: System level requirements

C Functional tree

Figures 22 and 23 describe the whole functional analysis.

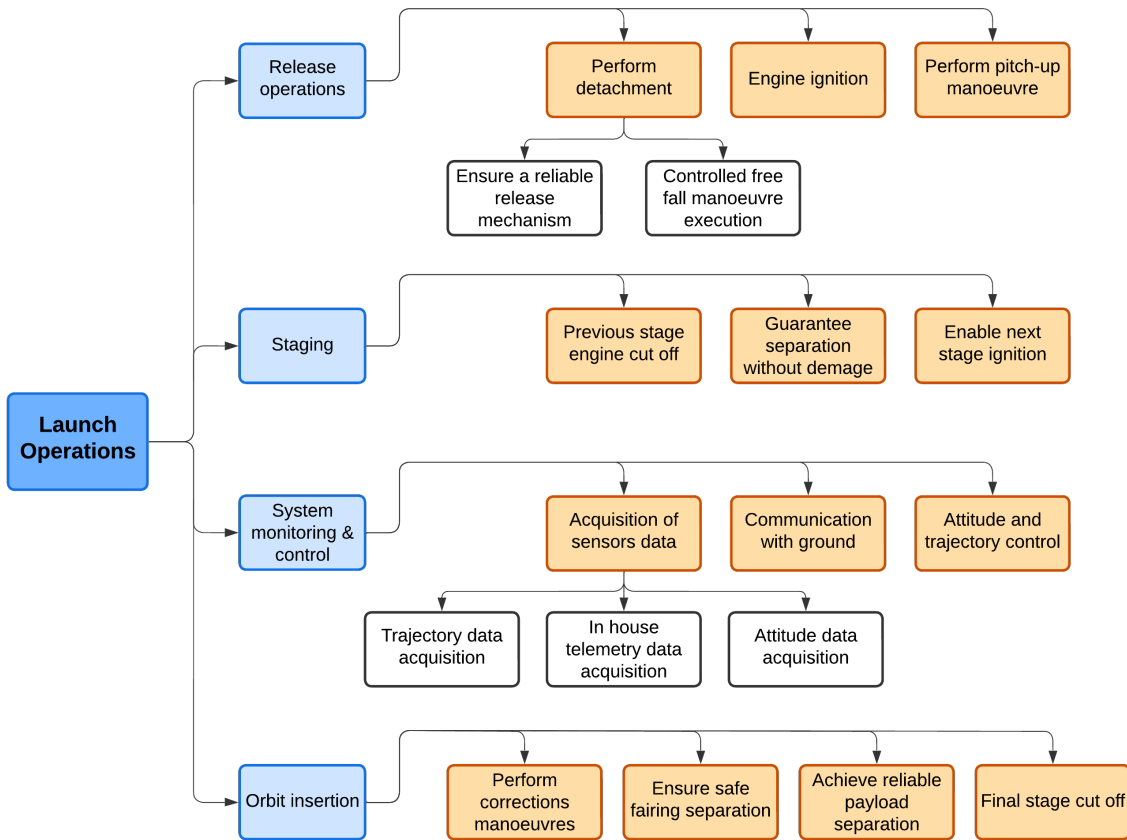


Figure 22: Launch operations functional tree

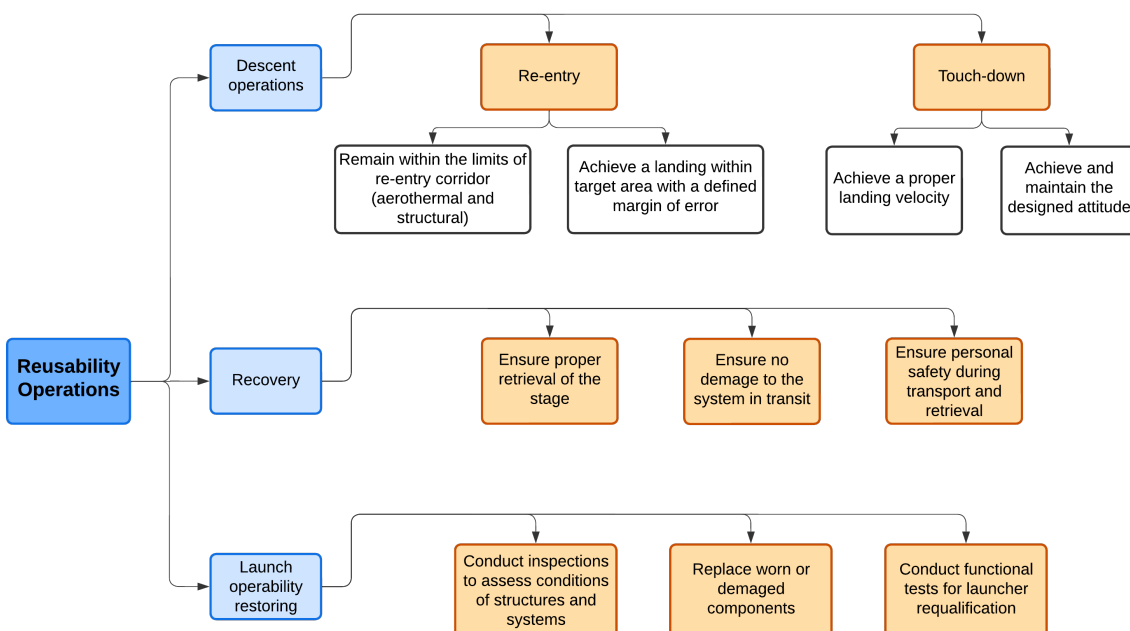


Figure 23: Recovery operations functional tree

D Regenerative Cooling

In regenerative cooling, the most popular cooling solution in bi-liquid engines, the fuel acts as a coolant in cooling channels around the combustion chamber. Using the thermodynamic properties of the flow inside the combustion chamber provided by CEA, a preliminary sizing of the regenerative cooling cycle was conducted. The primary unknown in this process is the convective heat transfer coefficient between the flow and the engine walls. To determine this value, various models and empirical correlations were evaluated.

For steady conditions and assuming a one-dimensional cooling jacket model, the heat transfer balance is expressed as shown in Equation 11.

$$Q_{hg,w} = Q_w = Q_{w,c} \quad (11)$$

where $Q_{hg,w}$ is the heat flux from the hot gas to the wall, Q_w is the heat flux through the wall, and $Q_{w,c}$ is the heat flux from the wall to the coolant flow. The convective wall heat flux, $Q_{hg,w}$, is given by the Equation 12.

$$Q_{hg,w} = h(T_{aw} - T_w) \quad (12)$$

where T_{aw} is the adiabatic wall temperature (or recovery temperature) and T_w is the wall temperature at the hot-gas side.

For the combustion chamber, the Gnielinski correlation shown in Equation 13 was used to calculate the Nusselt number [48].

$$Nu = \frac{\frac{f}{8}(Re - 1000)Pr}{1 + 12.7\sqrt{\frac{f}{8}}(Pr^{2/3} - 1)} \quad (13)$$

where f is the Darcy friction factor, Re is the Reynolds number, and Pr is the Prandtl number. The Reynolds number was calculated as shown in Equation 14.

$$Re = \frac{\rho v d}{\mu} \quad (14)$$

where ρ is the density, v the velocity, d the hydraulic diameter, and μ the dynamic viscosity. The velocity was determined using the Mach number and the speed of sound from CEA. The adiabatic wall temperature, T_{aw} , is expressed as shown in Equation 15.

$$T_{aw} = T \left(1 + r \frac{\gamma - 1}{2} M^2 \right) \quad (15)$$

where M is the Mach number, T the free stream temperature, γ the specific heats ratio, and r the recovery factor, related to the Prandtl number as $r = Pr^{1/3}$.

To calculate the Darcy friction factor, both the Petukhov and Konakov relations were considered [48]. The Petukhov relation, shown in Equation 16, was ultimately selected, as it provided better continuity between the Gnielinski model for the combustion chamber and the Bartz model used for the nozzle.

$$f = (1.82 \log(Re) - 1.64)^{-2}. \quad (16)$$

The convective heat transfer coefficient in the combustion chamber was calculated using Equation 17.

$$h = \frac{Nu k}{D_c} \quad (17)$$

where k is the thermal conductivity of the fluid and D_c the hydraulic diameter of the chamber. Assuming a constant T_{aw} for the chamber, the heat flux was calculated using these relationships.

In the nozzle, the Bartz model shown in Equation 18 was used to estimate the local convective heat transfer coefficient [49].

$$h = \left[\frac{0.026}{(D^*)^{0.2}} \left(\frac{\mu^{0.2}}{Pr^{-0.6} c_p} \right)_0 \left(\frac{P_c}{c^*} \right)^{0.8} \left(\frac{D^*}{r_c} \right)^{0.1} \right] \left(\frac{A^*}{A} \right)^{0.9} \sigma \quad (18)$$

where:

- $(\cdot)_0$ represents stagnation conditions
- h = convective heat transfer coefficient
- μ = dynamic viscosity
- c_p = specific heat
- Pr = Prandtl number
- c^* = characteristic velocity
- D^* = throat diameter, taken here as the hydraulic diameter
- r_c = throat radius of curvature, taken as 0.1 in. here
- A^* = cross-sectional area at the nozzle throat
- A = cross-sectional area at a given point along the nozzle
- σ = correction factor for heat transfer distribution shown in Equation 19

$$\sigma = \frac{1}{\left[\frac{1}{2} \frac{T_{wg}}{T_{0g}} \left(1 + \frac{k-1}{2} M^2 \right) + \frac{1}{2} \right]^{0.8-2\omega} \left(1 + \frac{k-1}{2} M^2 \right)^{0.2\omega}} \quad (19)$$

where:

- M = local Mach number
- T_{wg} = hot side wall temperature
- T_{0g} = hot gas stagnation temperature
- $\omega = 0.6$ for diatomic gases (assumed to be correct here).

The Rao nozzle was divided into smaller sections, and properties were converted to imperial units to match the model. An iterative process was conducted to evaluate the wall temperature and the convective coefficient for each segment, since $\frac{A^*}{A}$ and σ need to be evaluated at each coordinate along the nozzle. The axial heat conduction is neglected in all the models, both for the combustion chamber and the nozzle.

The regenerative cooling cycle uses only the fuel, assumed to be stored at 180 K, with cooling channels beginning at the nozzle's divergent section where the expansion ratio reaches 10, addressing the critical throat cooling requirements. The preliminary analysis focused mainly on the throat region, which experiences the maximum heat flux.

In figure 24 is shown the temperature profiles along the engine axis.

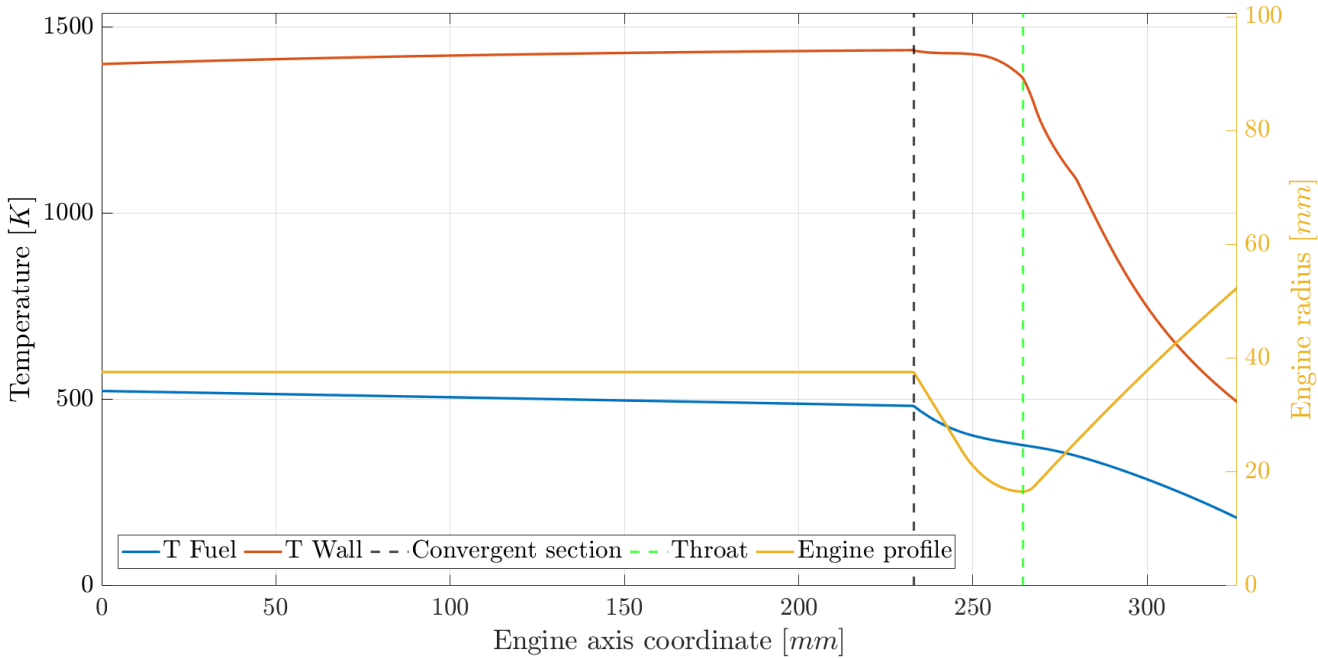


Figure 24: Temperature profiles along the engine axis

D.1 Thermal Barrier Coating

The results showed that the mass flow rate was sufficient to cool the chamber and nozzle. To ensure feasible wall temperatures, a $400 \mu\text{m}$ thermal barrier coating and an Inconel combustion chamber manufactured via additive manufacturing were considered.

Zirconia-Yttria Thermal Barrier Coatings (TBCs) are widely utilized in high-temperature applications such as aerospace and rocket engines due to their excellent thermal insulation properties and durability. These coatings consist primarily of Zirconium Dioxide (ZrO_2), stabilized with Yttrium Oxide (Y_2O_3) at concentrations typically between 6-8% by weight, forming Yttria-Stabilized Zirconia (YSZ) [50, 51].

One of the key advantages of $\text{ZrO}_2 - \text{Y}_2\text{O}_3$ TBCs is their low thermal conductivity, which ranges from approximately 1.0 to 2.5 $\text{W/m} \cdot \text{K}$ at 1000°C, depending on porosity and structural characteristics [51]. This property makes them highly effective at protecting underlying materials from extreme thermal environments. Additionally, their coefficient of thermal expansion (approximately $10.3 \times 10^{-6}/\text{K}$) is compatible with many superalloys such as Inconel, minimizing thermal stress and improving durability [52]. These coatings can operate at temperatures up to 1200°C for prolonged periods and withstand short-term exposures as high as 1400°C, making them suitable for the harsh environments encountered in rocket engines and gas turbines [53].

The mechanical properties of YSZ TBCs, such as a hardness of approximately 10-12 GPa and a density of 5.6-6.0 g/cm^3 , combined with a controlled porosity of 10-20%, enhance their thermal insulation capability and resistance to thermal shock [51, 53]. The porous microstructure not only lowers thermal conductivity but also provides strain tolerance, making these coatings suitable for applications involving repeated thermal cycling [54].

Given their ability to protect against extreme heat, oxidation, and corrosion, $\text{ZrO}_2 - \text{Y}_2\text{O}_3$ TBCs are integral to the performance of rocket engines, protecting combustion chambers and nozzles while enhancing their reusability and longevity [52, 51]. Furthermore, their application aligns with the increasing demands for cost-effective and sustainable aerospace technologies [50, 53].

E TRL Roadmap and Gantt chart

Using different guidelines and literature sources [55, 56, 57, 58], it was possible to create a detailed roadmap to guide each step of the TRL qualification process. This roadmap lays out a clear path for advancing through the TRL milestones from initial concept and early reviews to rigorous, full-scale testing. Each phase of development, testing, and refinement is informed by proven methods and recognized best practices. The only assumption made is the timeline that structures these activities. In order to have a time driven schedule for the engine development, the roadmap has been distributed through 4 years and not divided in Phases. The steps nominally included in Phase 0 and A, considering also the Preliminary Requirements Review (PRR) and System Requirements Review (SRR), have been assumed as already satisfied by the requirements set by the mission.

E.1 Year 1: Preliminary Development (TRL 1-3)

Months 1-3: Basic Principles and Conceptualization

- Identify Critical Technology Elements (CTEs) and define Key Performance Parameters (KPPs).
- Conduct a literature review to ensure state-of-the-art compliance.
- Develop and document conceptual designs for first and second-stage engines.
- Initiate feasibility studies for regenerative cooling and thrust chamber dynamics.
- **Milestone:** Conduct Preliminary Design Review (**PDR**):
 - Validate CTEs selection and initial design concepts.
 - Review feasibility studies and ensure alignment with TRL 1-3 requirements.

Months 4-6: Analytical and Experimental Proof of Concept

- Technology Selection:
 - Evaluate different turbopump configurations (e.g., centrifugal vs. axial) based on required flow rates, pressures, compatibility with propellants, efficiency, operational reliability. Take into account also COTS turbopump.
 - Compare injector types (e.g., pintle, coaxial, or swirl injectors) through CFD simulations and literature to optimize atomization quality and combustion stability.
 - Analyze regenerative cooling strategies (e.g., channel vs. film cooling) for thermal efficiency and manufacturability.
 - Select chamber materials and coatings to withstand thermal and chemical stresses.
- Create analytical models for:
 - Injector performance.
 - Combustion chamber thermodynamics.
 - Regenerative cooling heat transfer.
- Conduct small-scale laboratory experiments validating basic principles for selected technologies.
- Document results and adjust models based on initial experimental feedback.

Months 7-12: Breadboard Development

- Design and Fabrication:
 - Design low-fidelity breadboard components based on selected technologies. Starting from fabricating prototype injectors and turbopumps (if not COTS) using scalable techniques. Then design regenerative cooling channels for breadboard testing.
 - Procure materials and set up laboratory equipment for breadboard assembly.
- Testing:
 - Conduct initial thrust and combustion stability tests under ambient pressure.
 - Evaluate and refine regenerative cooling system efficiency.
 - Document failures, iterate on designs, and refine analytical predictions.

E.2 Year 2: Component and Subsystem Validation (TRL 4-5)

Months 13-18: Laboratory Testing of Breadboard

- Expand tests to simulate relevant environments:
 - Introduce higher pressures and temperatures to emulate operational conditions.
 - Analyze combustion efficiency and specific impulse (Isp).
 - Identify life-limiting mechanisms and failure modes.
- Update test results to improve brassboard designs.
- **Milestone:** Conduct Critical Design Review (CDR):
 - Validate breadboard test results.
 - Approve designs for scaling to brassboard level.

Output: Refined designs ready for brassboard development.

Months 19-24: Brassboard Development

- Design and Fabrication:
 - Scale breadboard designs to medium fidelity (brassboard) with realistic support elements.
 - Improve manufacturing techniques for precision and material compatibility.
- Testing
 - Test individual brassboard components (injector, nozzle, and combustion chamber) in relevant temperature and pressure environments.
 - Begin scaling studies to predict performance at full scale.
- Validate the physics of life-limiting mechanisms and potential failure modes.

Output: Ready-to-build high-fidelity prototypes.

E.3 Year 3: Prototype Development and System Integration (TRL 5-6)

Months 25-30: High-Fidelity Prototypes

- Prototype Design:
 - Develop high-fidelity prototypes, focusing on scaling issues and operational reliability.
 - Incorporate realistic cooling channels, chamber geometries, and injector configurations.
- Fabrication:
 - Production of components.
 - Use advanced manufacturing techniques (e.g., additive manufacturing for cooling channels) for flight-representative components.
 - Post-process and quality-check fabricated parts (especially for additive manufactured parts).
- Testing:
 - Conduct hot-fire tests of individual components in conditions approximating operational environments.
 - Simulate pressure cycles to evaluate structural integrity and fatigue resistance.
- **Milestone:** Conduct Qualification Review (QR):
 - Ensure prototypes meet performance requirements and are ready for system integration.

Months 31-36: System-Level Testing

- Assemble engine subsystems for integrated tests. Combine injector, combustion chamber, nozzle, and cooling systems. Test with full propellant flow rates and pressures.
- Validate performance metrics:
 - Specific impulse, thrust, thermal efficiency, and regenerative cooling effectiveness.
 - Check compatibility with operational interface requirements for the rocket stage.
- Begin troubleshooting and optimization based on test data.

Output: Fully integrated engine ready for operational testing.

E.4 Year 4: Flight-Ready Qualification (TRL 7-8)

Months 37-42: Operational Testing

- Conduct full-scale, high-fidelity engine tests:
 - Perform extended hot-fire tests to simulate actual mission profiles (e.g., varying throttle settings).
 - Test system durability under vibration and thermal cycling conditions mimicking launch environments.
- Begin flight-like demonstrations:
 - Test integration with rocket stage systems (e.g., tanks, avionics).
- **Milestone:** Conduct Flight-Readiness Review (**FRR**):
 - Review operational testing results.
 - Verify readiness for qualification and certification testing.

Months 43-46: Qualification Testing

- Test campaign:
 - Test for maximum performance envelopes.
 - Evaluate behaviour under extreme environmental conditions (e.g., thermal, vacuum, acoustic vibrations).
 - Conduct life testing to confirm engine longevity over multiple cycles.
- Develop production-ready blueprints and perform final design optimizations if needed.

Months 47-48: Flight Readiness and Certification

- Finalize engine configuration for production.
- Obtain certifications for commercial flight readiness from relevant authorities.
- Conduct a demonstration flight using the engine in operational conditions to achieve TRL 9.
- Document results and begin preparing for serial production.

Output: Flight-proven engine ready for serial production.

All the **Milestones** setted for this roadmap are:

- **PDR** ensures initial design aligns with requirements. (Month 3)
- **CDR** validates readiness for scaling up to the brassboard phase. (Month 18)
- **QR** confirms that prototypes are ready for full-system integration. (Month 30)
- **FRR** guarantees the system is ready for operational testing and certification. (Month 42)

In order to have a clear roadmap, the Acceptance Review (AR) and Operational Readiness Review (ORR) was omitted and considered performed with the QR.

After the FRR, a Launch Readiness Review (LRR) shall be performed, immediately prior to launch.

In Figure 25 is reported a Gantt chart representing all the steps required for the certifications.

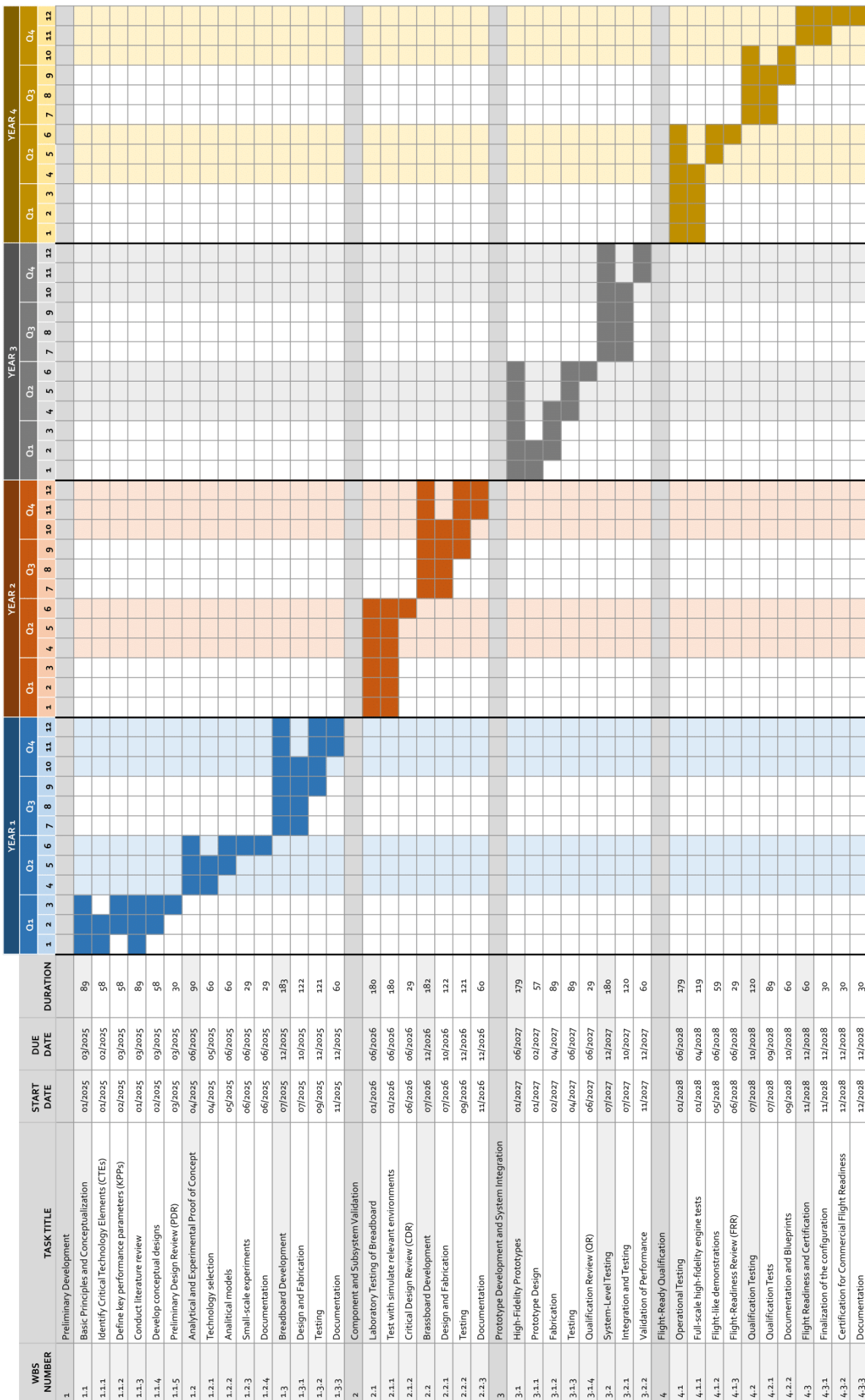


Figure 25: Gantt Chart Engine TRL Qualification

F Detailed model ruling the trajectory

The equation of motion (Equation 20) of a 2-DOF point mass model assumption, with a frame of reference set to be coincident with the centre of a non-rotating windless Earth, and the evaluation of its characteristic parameters (Equation 21) are presented below:

$$\begin{cases} \frac{dv}{dt} = \frac{T}{m} \cos(\delta) - \frac{D}{m} - g \sin(\gamma) \\ \frac{d\gamma}{dt} = \frac{v \cos(\gamma)}{R_{\oplus} + h} + \frac{T \sin(\delta)}{mv} + \frac{L}{mv} - \frac{g \cos(\gamma)}{v} \\ \frac{dh}{dt} = v \sin(\gamma) \\ \frac{d\chi}{dt} = \frac{v \cos(\gamma)}{R_E + h} \end{cases} \quad (20)$$

where:

$$\begin{cases} L = \frac{1}{2} \rho v^2 A C_L \\ D = \frac{1}{2} \rho v^2 A C_D \\ g = \frac{g_0}{(1 + \frac{h}{R_{\oplus}})^2} \end{cases} \quad (21)$$

F.1 Optimization approach

The optimization is carried out as a shooting problem exploiting the built-in Matlab® function called '*fmincon*'. The problem can be further divided into:

- **Objective function:** initially set to be coincident with Δv_{losses} (Equation 22):

$$J = \Delta v_{drag} + \Delta v_{gravity} \quad (22)$$

and then modified to be a weighted (only on γ_f) sum of the insertion errors (Equation 23):

$$J = \left(v_f - \sqrt{\frac{\mu}{r_f/1000}} \cdot 10^3 \right) + (\gamma_f \cdot 5 \cdot 10^4) + (h_f - 400 \cdot 10^3) \quad (23)$$

- **Variables:**

- v_0, γ_0, h_0 : release conditions after the free-fall manoeuvre.
- t_{b1}, t_{off}, t_{b2} : time duration of the different sections of the trajectory which do not have to coincide to the time required to burn all the propellant on board.
- $\Delta\gamma$: variation of the flight path angle during the first leg.
- Δm_{prop2} : additional propellant mass applied on the second stage.

- **Equality constraints:**

- $v_f = \hat{v}_f$: the circular orbital velocity at the target radius $v_f = \sqrt{\mu/(R_{\oplus} + h_f)} = 7.669$ km/s.
- $\gamma_f = \hat{\gamma}_f$: has to be zero in order to correctly match a circular orbit.
- $h_f = \hat{h}_f$: set by the requirements at 400 km.

- **Inequality constraints:** the height and velocity at the staging condition are limited by the recovery requirement. Upper boundaries for this parameters are defined progressively lowering them until a feasible solution was reached in order to contain the reentry loads.

- $v_{staging}$: the speed at staging condition is set to be lower than 3000 m/s.
- $h_{staging}$: likewise the maximum height to perform this operation is defined as 90 km.

G Trajectory with updated payload mass

The states of the system are evaluating starting from the same initial conditions as for the nominal case but with a different payload mass of $m_{pay} = 400$ kg (Figure 26).

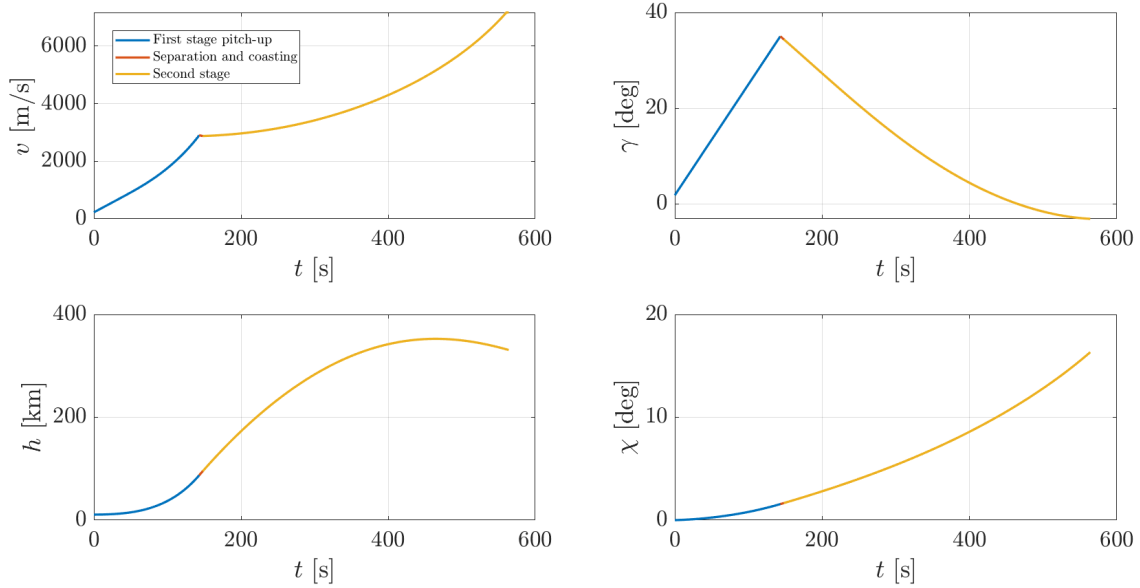
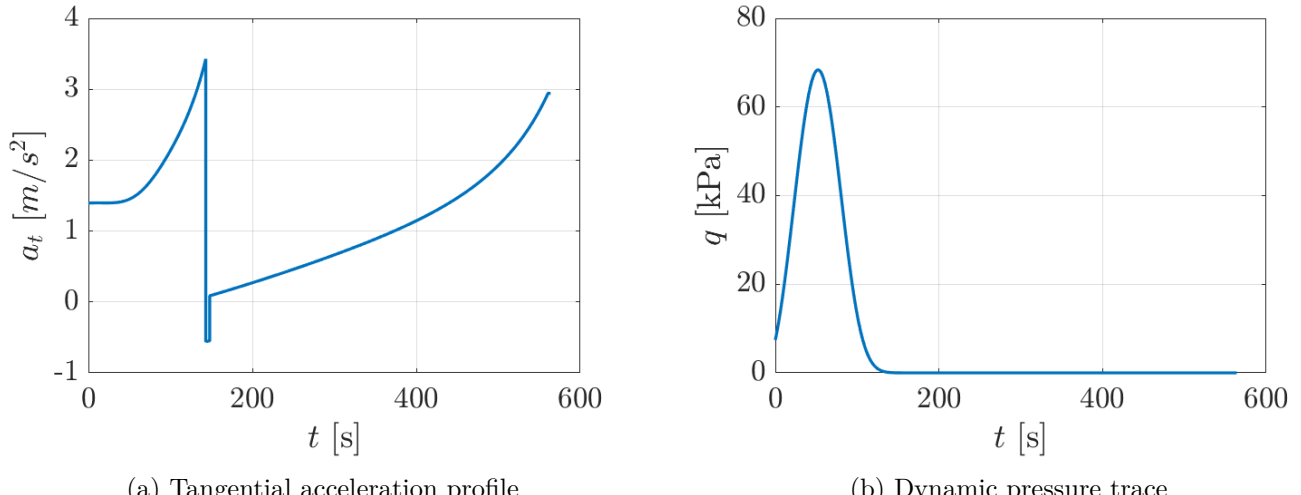


Figure 26: Trajectory with 400 kg payload mass

In addition, the tangential acceleration and the dynamic pressure are computed and shown in Figure 27).



(a) Tangential acceleration profile

(b) Dynamic pressure trace

Figure 27: Main loads acting during the trajectory with 400 kg payload mass

H Re-entry

A detailed evaluation of landing strategies is provided:

- **Return To Launch Site (RTLS):** Used by Falcon 9 and Super Heavy, RTLS involves multiple rotation maneuvers and boost-backs to reverse the flight direction and reduce loads. Despite its effectiveness, RTLS requires substantial fuel reserves, making it unsuitable for weight-sensitive designs.
- **DownRange Landing (DRL):** In DRL, the lower stage lands vertically on a downrange platform, typically at sea. This minimizes re-entry loads but requires precise platform placement.
- **Fly-Back (FB):** After separation, the stage uses aerodynamic lift and air-breathing engines to return to the landing site. This method relies on wings and additional propulsion systems, increasing design complexity.
- **In-Air Capturing (IAC):** Under development in the European FALCon project, IAC involves a towing plane capturing the stage mid-air and towing it back to a runway. This eliminates the need for additional fuel but requires complex towing mechanisms and precise coordination. A roadmap predicts achieving TRL 6 by the decade's end [59] (see Figure 28).

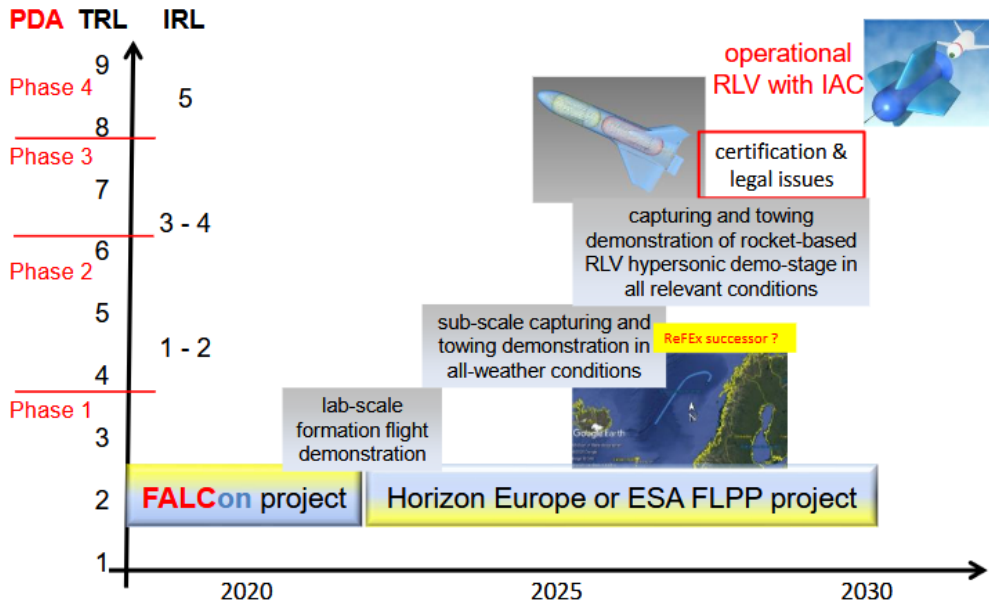


Figure 28: Development Roadmap major system demonstrations for “In-Air-Capturing” [60].

- **Splashdown:** Involves water landings with parachutes, minimizing additional fuel requirements and hardware complexity. While saltwater exposure poses challenges to reusability, solutions like protective sleeves and hardware coatings (e.g., NASA’s solid boosters and Rocket Lab’s Electron [61]) mitigate damage. Historical patents also describe methods to shield critical components from impact and corrosion [17].

Figure 29 shows the results of the first stage re-entry simulation.

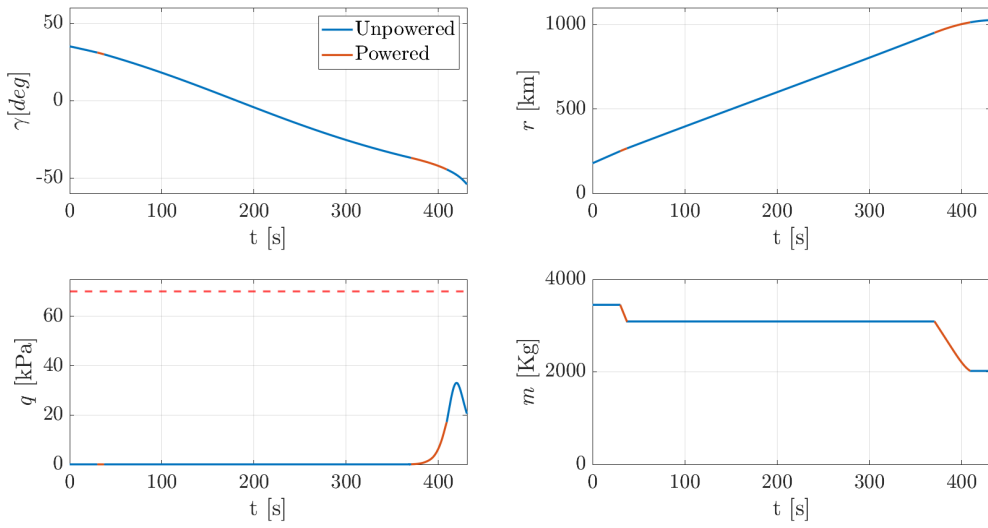


Figure 29: Boostback re-entry trajectory

The results of the first stage parachute deployment simulation are presented in Figure 30.

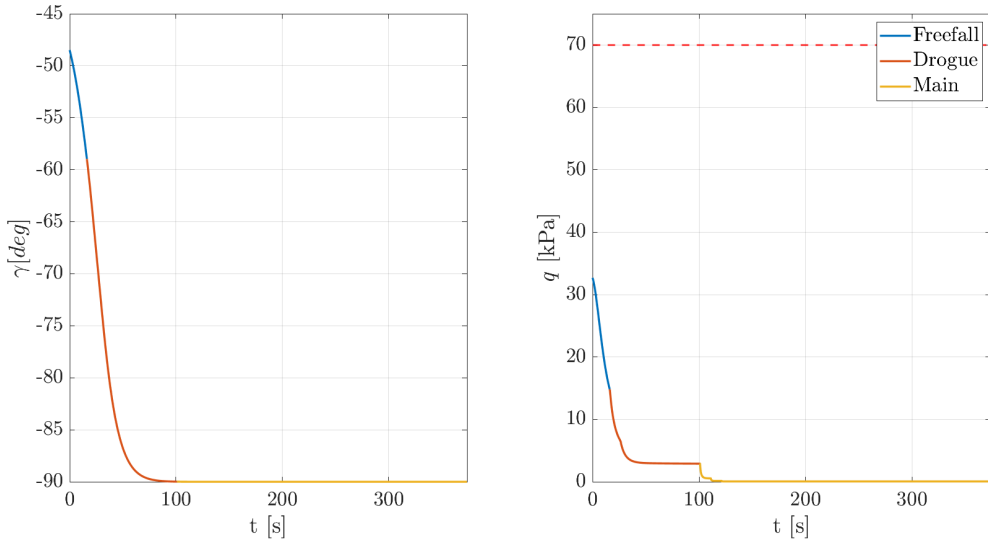


Figure 30: Parachute re-entry trajectory

I MER and LV discretization results

In Table 29 the output of the statistical relations used for the mass estimation of the LV components are reported. In Table 30 the centre of gravity and mass of the discretized segment of the LV can be instead appreciated in different flight conditions.

Component	Statistical Relation [6]	Mass [kg]
LRE first stage	$TW_1 \cdot g_0 \cdot m_{01} \cdot (7.81 \cdot 10^{-4} + 3.37 \cdot 10^{-5} \cdot \sqrt{\epsilon_1}) + 59$	346
First skirt	$A_{env} \cdot 13.3$	107
Thrust structure 1 _{st} stage	$2.55 \cdot 10^{-4} \cdot T/W_1 \cdot g_0 \cdot m_{01}$	75
Avionics	typical value for small LV	75
Interstage	$A_{env} \cdot 13.3$	164
First stage Gimbal	$N_{eng} \cdot 237.8 \cdot (\frac{TW_1 \cdot g_0 \cdot m_{01}}{N_{eng} \cdot P_{cc}})^{0.9375}$	7
Second skirt	$A_{env} \cdot 13.3$	42
Forward skirt	$A_{env} \cdot 13.3$	42
LRE second stage	$TW_2 \cdot g_0 \cdot m_{02} \cdot (7.81 \cdot 10^{-4} + 3.37 \cdot 10^{-5} \cdot \sqrt{\epsilon_2}) + 59$	86
Thrust structure 2 _{nd} stage	$2.55 \cdot 10^{-4} \cdot TW_1 \cdot g_0 \cdot m_{01}$	6
Electrical wiring	$1.43 \cdot L$	51
Payload adaptor	$0.0755 \cdot m_{pay}^{max} + 50$	80
Fairing mass	$4.95 \cdot A_f^{1.15}$	103
LOX insulation	$1.12 \cdot A_{LOX}$	37

Table 29: MER results

	S1	S2	S3	S4	S5	S6	S7	S8	S9	LV
m_i [kg] @ ignition	445	126	2.127	1.020	144	650	10.297	4.878	749	20.436
C_g^i [m] @ ignition	3.30	4.30	5.34	6.61	7.29	8.42	11.60	15.48	17.56	11.49
m_i [kg] @ max $q\alpha$	445	126	2.127	1.020	144	650	7.927	3.765	749	16963
C_g^i [m] @ max $q\alpha$	3.30	4.30	5.34	6.61	7.29	8.42	12.24	15.78	17.56	11.57
m_i [kg] @ max q	445	126	2.127	1.020	144	650	7.017	3.337	749	15625
C_g^i [m] @ max q	3.30	4.30	5.34	6.61	7.29	8.42	12.43	15.91	17.56	11.54
m_i [kg] @ meco	445	126	2.127	1.020	144	650	1187	600	749	7058
C_g^i [m] @ meco	3.30	4.30	5.34	6.61	7.29	8.42	13.34	16.45	17.56	9.29
m_i [kg] @ recburn	-	-	-	-	-	650	1187	600	749	3186
C_g^i [m] @ recburn	-	-	-	-	-	0.25	4.63	7.74	8.85	0.58 ¹⁰

Table 30: C_g^i and m_i @ different flight conditions

¹⁰ C_g positions are expressed starting from the nose of the LV. In the case of recovery burn event, the LV 1_{st} stage is already separated, thus the new reference point is at the beginning of the 1_{st} stage itself.

J Loads computations results

The computed loads for different flight conditions are reported through this section. Given the discretization of the launch vehicle, the forces are concentrated and not distributed, in the centre of mass of each segment and on the centre of pressure of the nose, skirt and fins for the aerodynamic forces. Each concentrated force creates a discontinuity in the load diagram. Axial loads at each section are computed summing up the contribution of the inertial loads, weights and Drag, under the hypothesis of null angle of attack [6], which will be relaxed for the shears and bending moment computations. Shears are computed considering a non null AOA for $\max q\alpha$ as visible in Figure 31, while in clamping condition they are due to the LV own weight when constrained under the carrier. As first guess only two connection points have been considered, modeling as two forces normal to the body axes. The actual reaction forces distribution in clamping condition is much more complex, but for a preliminary analysis it has not been analysed further. Results are reported in Figure 32.

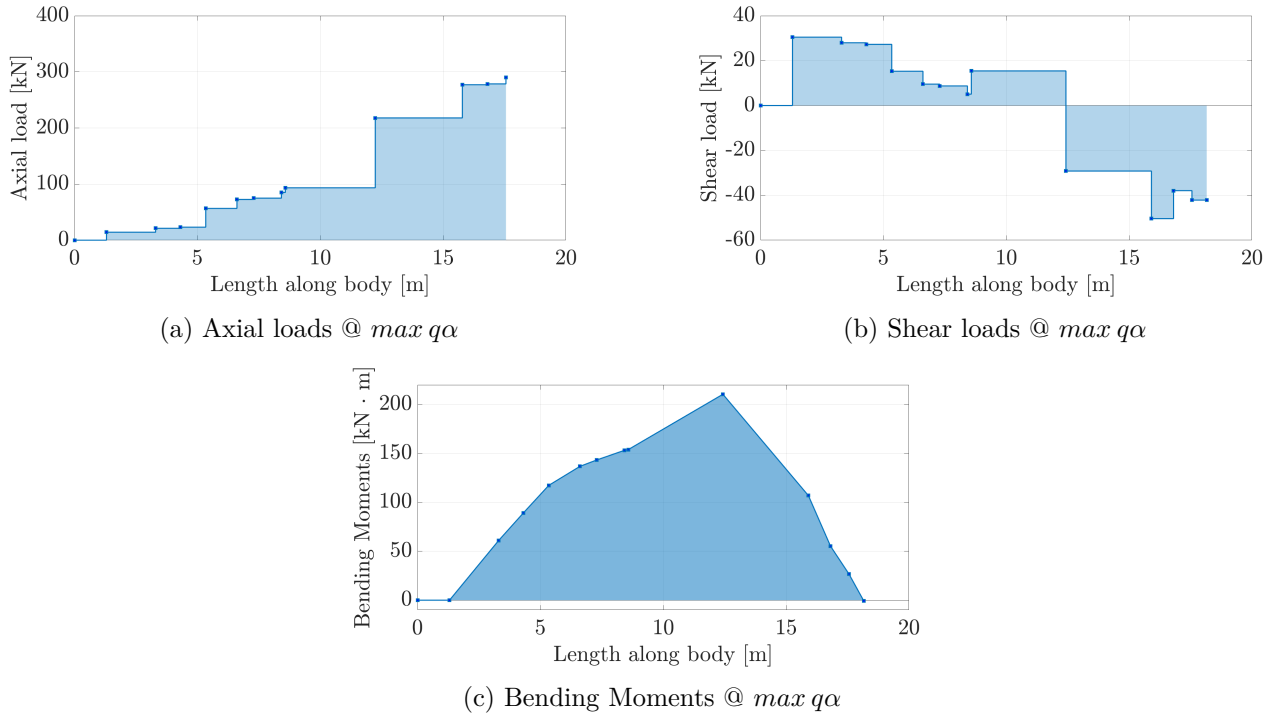


Figure 31: Load analysis @ $\max q\alpha$

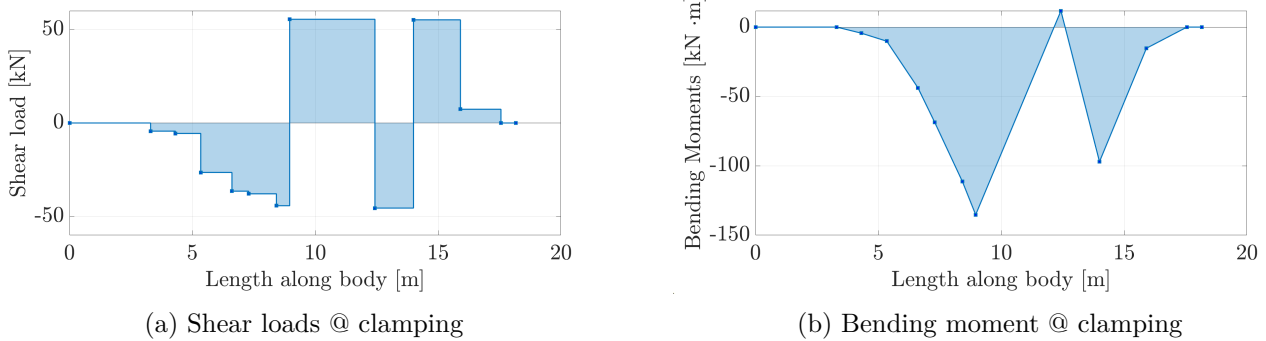


Figure 32: Load analysis @ clamping

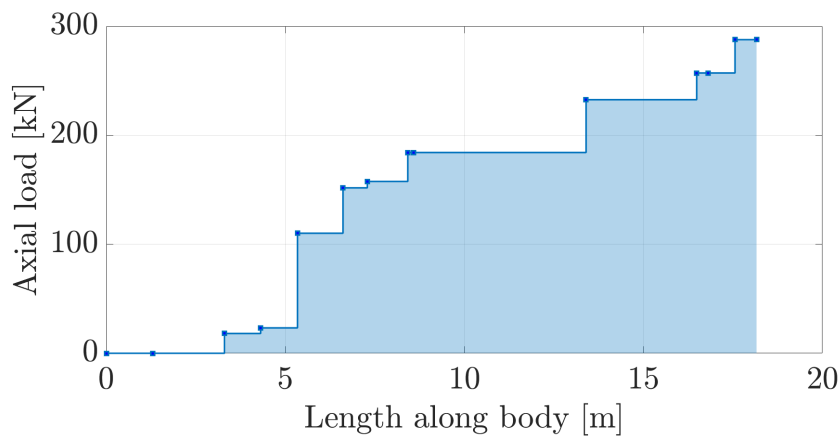
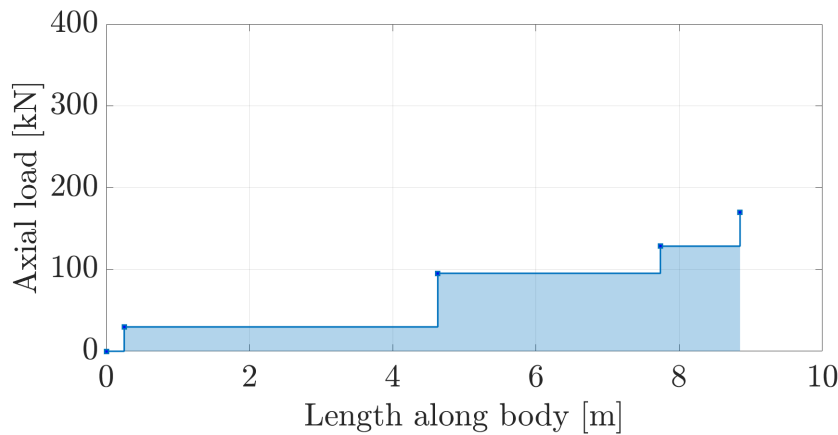
Figure 33: Axial load @ *meco*

Figure 34: Axial load @ Recovery

Looking at Figures 33 and 34, it's noted that at MECO condition, the axial loads felt by the primary structure of the second stage is much higher with respect to previous flight conditions. This is expected since the axial acceleration is higher, about 4 g, and the mass remains the same. Additional shocks right after separation have not been analysed, but they may caused local failures in the structures, thus they must be taken into account in a refined analysis.

The axial loads at recovery boost-back are much smaller with respect to previously analysed cases. This is expected since the mass is much lower, thus even if acceleration are strong (about 6 g) the actual forces felt by the structure are lower. The value of the axial load at 18.16 m length is equal to 160 kN which match the thrust level of the engine during the boost-back. Finally, it's emphasized that the reported length in Figure 34 is coherent with the one of the first stage.

K Wind modeling

As stated in Section 2.6, the wind gauges have been modelled using an experimental correlation [6] that for clarity is reported below in Equation 24.

$$v_{wind} = \begin{cases} 6.9288 \cdot h_{km} + 9.144 & \text{if } h_{lm} < 9.6 \\ 76.2 & \text{if } 9.6 < h_{km} < 14 \\ 76.2 - 8.9474 \cdot (h_{km} - 14) & \text{if } 14 < h_{km} < 20 \\ 24.384 & \text{if } h_{km} > 20 \end{cases} \quad [\text{m/s}] \quad (24)$$

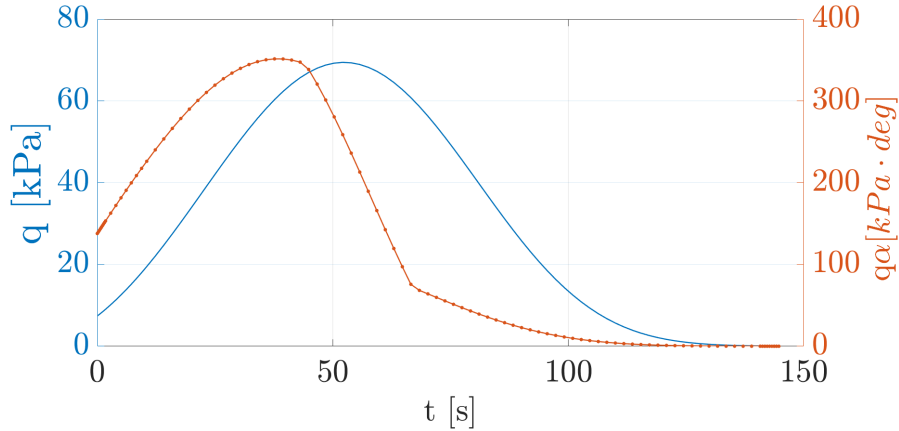


Figure 35: Evolution of $q\alpha$

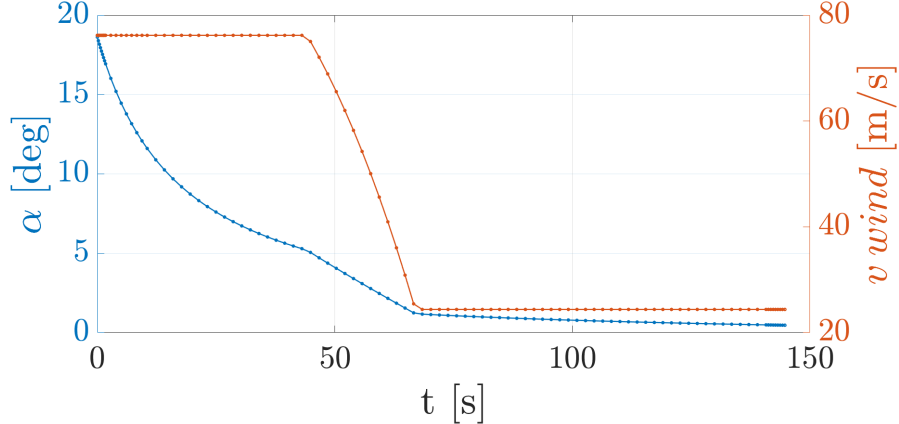


Figure 36: AOA and wind speed

In Figure 35 it's possible to appreciate the trend of $q\alpha$ with respect to $\max q$. The results are strongly conditioned by the assumptions made in the wind speed modeling:

- AOA assumes high values at the beginning, when the launch vehicle speed is still relatively low. It progressively decreases together with the wind speed as time, thus altitude, increases.
- The LV stability at the beginning of the flight will be a critical point to address in further developments, since strong gauges may cause a high AOA.
- According to the trend visible in Figure 36, the peak of $q\alpha$ happens in the first leg of the flight, where the atmosphere is denser and AOA is still high.

L Material Analysis

During the initial phase of material selection, a literature review highlighted a growing trend in the aerospace sector where many companies are shifting from aluminium alloys to composite materials with particular interest in sandwich structures. These solutions offer numerous advantages, including a high strength-to-weight ratio and faster manufacturing processes. However, they also present significant drawbacks, such as limited fatigue resistance, poor thermal resistance and a tendency to develop cracks when exposed to cryogenic propellants [6].

In unpressurised sections of rockets, such as skirts, intertanks, and interstages the absence of internal pressure, which is an important structural advantage as described in Section 2.6.1, must be compensated by optimized structural design that integrates skins and stringers. This approach increases structural strength without significantly increasing overall thickness, providing a mass-saving advantage while maintaining the ability to withstand loads and resist buckling instability.

In modern rockets, unpressurised isotropic structures are increasingly being replaced by composite sandwich panels. These panels offer significant advantages in terms of bending stiffness and buckling resistance. They are composed of two laminates, typically made of composite material, separated by a honeycomb core, usually made of aluminium alloy. For example, separating the two laminates by a thickness six times that of a single laminate results in bending stiffness 18 times higher than simply bonded laminates, with a mass increase limited to 20% (note: this example assumes a face sheet density 15 times higher than the core, in line with typical values) [6].

The main challenges with sandwich structures involve the interfaces. Due to the low density of the honeycomb core, these areas are less effective at handling concentrated loads. The most common strategy to address this issue is to increase the core density at the interface points, while still maintaining higher efficiency compared to traditional structures. Although the use of composite materials is well-established in dry structures, many companies are exploring the possibility of using them for tanks as well. A significant example is the Launcher One rocket, which uses carbon fiber tanks, including for LOX.

Despite the clear advantages of adopting composite materials, in the conceptual design of the LV it has been decided to use isotropic materials exclusively [6] for the reasons explained in Section 2.6.

The isotropic materials commonly used in launch vehicles are:

- Al 6XXX series: these alloys offer high strength, good machinability, and low costs. However, their main drawbacks include a high coefficient of thermal expansion, galling issues, and poor corrosion resistance. They are typically used for structures like trusses, stringers, and brackets.
- Al 7XXX series: this series is characterized by high mechanical strength, good fatigue resistance, and corrosion resistance. However, it has a high coefficient of thermal expansion and is prone to embrittlement. These alloys are used in highly stressed structures.
- Titanium alloys and Inconel-based materials: these are used in regions requiring high thermal resistance and insulation, but they have significant limitations in terms of machinability and costs.

For tanks, aluminium alloys in the 2XXX series are among the most commonly used, particularly the 2219 and 2014 alloys, which are often employed for cryogenic solutions. Recently, the aluminium-lithium alloy Al-Li 2195 has been the subject of extensive studies and tests, with the goal of replacing the more common 2219 alloy. NASA, in particular, has launched a program to raise the TRL of cryogenic tanks made of Al-Li 2195 to level 6 [34]. This alloy offers several advantages compared to other aluminium alloys, including:

- Greater isotropy and reduced fatigue crack growth.
- Improved cryogenic ductility.
- Higher strength and fracture toughness, especially under thermal excursions.
- A high strength-to-weight ratio, thanks to its high specific strength, high modulus, and low density, resulting in significant mass savings.

Due to these advantages, the Al-Li 2195 alloy has been chosen for the primary structure of the LV, proving to be an optimal solution for enhancing reusability and reducing overall mass.

M Mathematical procedure for calculating wall thickness

The primary structure of a launch vehicle refers to the portion of the structure designed to withstand the main loads experienced throughout its operational life. These include axial, shear, hoop loads, and bending moments, ensuring mechanical integrity during transport, launch, and flight. The first step in structural analysis is to compute the loads generated under the most critical conditions, as described in Section 2.6.1. Subsequently, for each section of the LV, it is necessary to calculate the minimum thickness required for the structure to withstand compressive, shear, and hoop loads, using Equations 25, 27, 26.

$$t_{req_axial} = \frac{FS}{\sigma_{allow}} \cdot \left[\frac{P}{2\pi R} + \frac{M}{\pi R^2} - \frac{R}{2}(p + \rho g_0 n_x h) \right] \quad (25)$$

$$t_{req_hoop} = \frac{FS}{\sigma_{allow}} R(p + \rho g_0 n_x h) \quad (26)$$

$$t_{req_shear} = \frac{FS F_b}{2\pi R^{\frac{1}{2}} \sigma_{allow}} \quad (27)$$

where:

- t_{req_axial} = Required thickness to withstand axial load.
- t_{req_hoop} = Required thickness to withstand hoop load.
- t_{req_shear} = Required thickness to withstand axial shear.
- σ_{allow} = Yield strength of the material.
- P = Axial load.
- M = Bending moment.
- F_b = Shear force.
- R = Radius of the cylinder.
- p = Pressure.
- n_x = Acceleration in g_0 .
- h = Height of the propellant column.

After verifying resistance to these loads, it is essential to assess buckling resistance. Buckling is a structural instability phenomenon that occurs when a component under compression exceeds a critical load, leading to sudden deformation. Detailed analysis of this instability would require advanced mathematical modeling and experimental validation, which exceed the conceptual level of this design phase. For an initial estimation of wall thicknesses that ensure buckling resistance, empirical formulas can be used [6]. For cylindrical shapes, such as the tanks of the first and second stages, skirts, and forward skirts, implicit Equations 28 and 29 can be applied. These formulas differentiate between pressurized sections, like tanks, and non-pressurized sections. For truncated cone shapes, such as the interstage, implicit Equations 30, 31 and 32 are recommended.

In the LV under analysis, the nose of the LV can be approximated as a conical shape for structural evaluations. It is noted that for conical geometries, where $r = 0$, Equation 32 loses physical validity, as M_{cr} becomes null, resulting in no solution. While it is possible to proceed without considering the bending moment, this would underestimate the acting loads. Therefore, for the nose, it was decided to approximate it as a cylinder with a diameter equal to the cone base and integrate it with the cylindrical base of the fairing.

The interstage, as shown in Figure 12 consists of a cylindrical section and a truncated cone section. These are dimensioned using Equations 32 and 28, respectively. The cylindrical section at the base requires a greater thickness than the truncated cone section. To provide a uniform thickness across the interstage, the thickness of the entire section is determined by the requirements of the cylindrical base.

$$\sigma_{b_unpress} = \frac{FS \cdot P}{A} + \frac{FS \cdot M \cdot R}{I} = \left[9 \cdot \left(\frac{t}{R} \right)^{0.6} + 0.16 \cdot \left(\frac{R}{L} \right)^{1.3} \cdot \left(\frac{t}{R} \right)^{0.3} \right] \cdot \frac{E \cdot t}{R} \quad (28)$$

$$\sigma_{b_press} = \frac{FS \cdot P}{A} + \frac{FS \cdot M \cdot R}{I} = \left[9 \cdot \left(\frac{t}{R} \right)^{0.6} + 0.16 \cdot \left(\frac{R}{L} \right)^{1.3} \cdot \left(\frac{t}{R} \right)^{0.3} + \min \left\{ \begin{array}{l} 0.191 \cdot \frac{P}{E} \cdot \left(\frac{R}{t} \right)^2 \\ 0.229 \end{array} \right\} \right] \cdot \frac{E \cdot t}{R} \quad (29)$$

$$P_{cr} = 0.33 \cdot \frac{2 \cdot \pi \cdot E \cdot t^2 \cos(\alpha)^2}{\sqrt{3 \cdot (1 - \nu^2)}} \quad (30)$$

$$M_{cr} = 0.41 \cdot \frac{2 \cdot \pi \cdot E \cdot t^2 \cos(\alpha)^2 \cdot r}{\sqrt{3 \cdot (1 - \nu^2)}} \quad (31)$$

$$\frac{FS \cdot P}{P_{cr}} + \frac{FS \cdot M}{M_{cr}} = 1; \quad (32)$$

where:

- $\sigma_{b_unpress}$ = Critical buckling stress for non-pressurized cylindrical shape.
- σ_{b_press} = Critical buckling stress for pressurized cylindrical shape.
- I = Moment of inertia of the cylinder.
- t = Thickness.
- L = Length of the cylinder.
- P_{cr} = Critical Axial Load for buckling in a frustum shape.
- M_{cr} = Critical bending moment for buckling in a frustum shape.
- α = semivertex Angle of the frustum shape.
- r = Minor radius of the frustum.
- ν = Poisson's ratio.

It is noted that a factor of safety was applied during the sizing process. This is necessary to account for approximations introduced by the mathematical models used and to ensure resistance to unforeseen overloads.

Table 31 presents the thicknesses of all sections, determined for the various phases of the mission.

	Fairing	F.S. st ₂	LOX st ₂	RP1 st ₂	S. st ₂	Int.	LOX st ₁	RP1 st ₂	S. st ₁
<i>maxq</i> [mm]	1.3	1.4	1.9	2.0	1.7	1.8	2.5	2.3	1.7
<i>maxq_a</i> [mm]	1.4	1.6	2.1	2.2	1.9	2.1	2.8	2.5	1.8
<i>MECO</i> [mm]	0.001	0.002	1.2	1.4	1.2	0.12	1.8	1.8	1.7
<i>recovery</i> [mm]	-	-	-	-	-	2.1	2.8	2.5	1.8
<i>Clamping</i> [mm]	0.009	0.021	1.3	1.6	1.6	1.9	0.67	0.779	0.779

Table 31: LV wall thickness with respect to phase

It is noted that thickness values have been included even below the typical manufacturing limit of 0.5 mm for aluminium alloys [6]. This is done to better highlight the theoretical values required at each phase of flight.

N Aerodynamic coefficients

The following section aims to present the integrated formulas and relations ruling the estimation of the launcher aerodynamic coefficients. A consistent part of the implemented computational approach follows the Jorgensen method [38, 39, 40] including other models able to predict specific components performances within a certain margin of accuracy at the same time.

N.1 Axial force coefficient

The axial force coefficient is computed according to Jorgensen as the product between the coefficient at $\alpha = 0$ and a term accounting for the angle of attack as illustrated in Equation 33.

$$C_A = C_{A_{\alpha_0}} \cos^2(\alpha) \quad (33)$$

The zero-angle-of-attack term is composed of three contributions: wave, base, and skin friction contributions as shown in Equation 34.

$$C_{A_{\alpha_0}} = C_{A_w} + C_{A_{sf}} + C_{A_b} \quad (34)$$

Moreover, the final C_A retrieved has been increased of 10% to account for parasitic drag contributions. The pressure wave contribution given by the nose is greatly dependent on the shape of the nose itself. In the case of a Haack-Von Karman nose, the value of the contribution is computed through Equation 35 [62].

$$C_{A_w}^{nose} = C_0 \left(\frac{C_0}{C_3} \right)^{\log_4(f_n+1)} \quad (35)$$

Where C_0 is the pressure coefficient of a blunt cylinder with its axis aligned to the flow, f_n is the fineness ratio of the nose, and C_3 is extrapolated from experimental data [37], representing the pressure coefficient of a Von-Karman shape with slenderness ratio equal to 3. This result is then scaled onto the A_{ref} reference surface corresponding to the cylindrical base area of the launcher first stage by multiplying the nose wave pressure coefficient by $\frac{A_{nose}}{A_{ref}}$ where A_{nose} represents the base area of the nose shape.

The shoulder contributes to the overall axial wave pressure coefficient as well. Its value can be extrapolated from the wave pressure coefficient for conical nose shapes expressed by Linnell-Bailey correlation [39] and illustrated in 36.

$$C_{A_w}^{shoulder} = \begin{cases} 0.8 \sin^2(\theta_s) & \text{if } M \leq 1, \\ \frac{4 \sin^2(\theta_s)(2.5 + 8\beta \sin(\theta_s))}{1 + 16\beta \sin(\theta_s)} & \text{if } M > 1, \end{cases} \quad (36)$$

Where θ_s is the equivalent cone aperture angle. This coefficient is rescaled considering the shoulder base exposed area, thus multiplying it by $\frac{d_{us}^2 - d_{ds}^2}{d_{ref}^2}$ containing the upstream and downstream skirt diameter.

The base contribution is computed using the Gabeaud formulation for the base pressure coefficient during supersonic cruise, while an empirical approximation is applied for subsonic regime [62] and shown in Equations 37 and 38.

$$C_{p_b} = \frac{2}{\gamma M^2} \left\{ \left(\frac{2}{\gamma + 1} \right)^{1.4} \left(\frac{1}{M} \right)^{2.8} \left[\frac{2\gamma M^2 - (\gamma - 1)}{\gamma + 1} \right] - 1 \right\} \quad (37)$$

$$C_{A_b} = \begin{cases} 0.12 + 0.13M^2 & \text{if } M \leq 1 \\ -C_{p_b} & \text{if } M > 1 \end{cases} \quad (38)$$

The γ value is assumed constantly equal to 1.4 since it is mainly dependent from the gas composition that preserves up to the Von-Karman line. The axial base pressure coefficient needs to be rescaled upon

the effective application area excluding from the base area A_b the overall exit area of the nozzle A_e by multiplying C_{A_b} for $\frac{A_b - A_e}{A_{ref}}$.

The skin friction contribute is obtained through semi-empirical correlations [62] as detailed in Equation 39.

$$C_f = \begin{cases} 1.48 \times 10^{-2} & \text{if } Re < 10^4 \\ \frac{1}{(1.50 \ln(Re) - 5.6)^2} & \text{if } 10^4 \leq Re < Re_{crit} \\ 0.032 \left(\frac{R_s}{l}\right)^{0.2} & \text{if } Re \geq Re_{crit} \end{cases} \quad (39)$$

Where C_f is the skin friction coefficient over a flat surface of length l coinciding with the length of the whole cylindrical body, while R_s is the approximate roughness height of the surfaces set to $5 \mu\text{m}$, assuming an optimally spray-painted surface [62]. The critical roughness Reynolds number can be computed thanks to Equation 40.

$$Re_{crit} = 51 \left(\frac{R_s}{l}\right)^{-1.039} \quad (40)$$

Moreover C_f value is corrected through compressibility correction factors as illustrated below in Equations 41.

$$C_{f_c} = \begin{cases} C_f (1 - 0.1M^2) & \text{if } M < 1, \\ \max \left\{ \frac{C_f}{1+0.18 \cdot M^2}, \frac{C_f}{(1+0.15 \cdot M^2)^{0.58}} \right\} & \text{if } M \geq 1. \end{cases} \quad (41)$$

At the end, the overall axial contribution can be expressed through Equation 42.

$$C_{A_{sf}} = C_{f_c} \frac{\left(1 + \frac{1}{2f_b}\right) A_{wet}}{A_{ref}} \quad (42)$$

Where f_b is the fineness ratio of the launcher body, A_{wet} is the overall wetted area. The results are reported in Figure 38 and Figure 37.

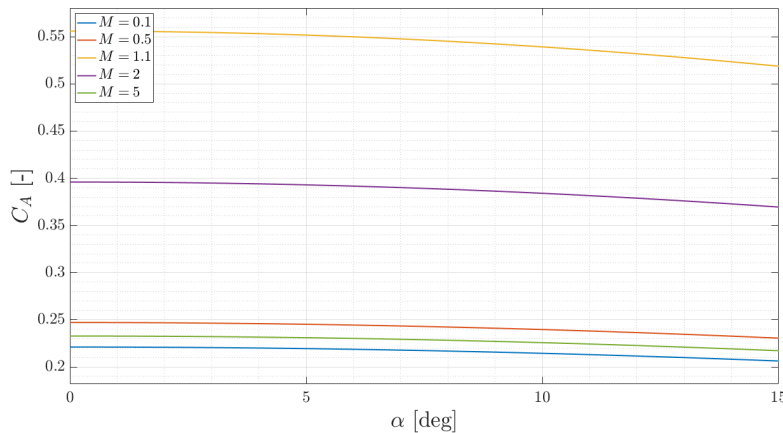


Figure 37: Axial force coefficient

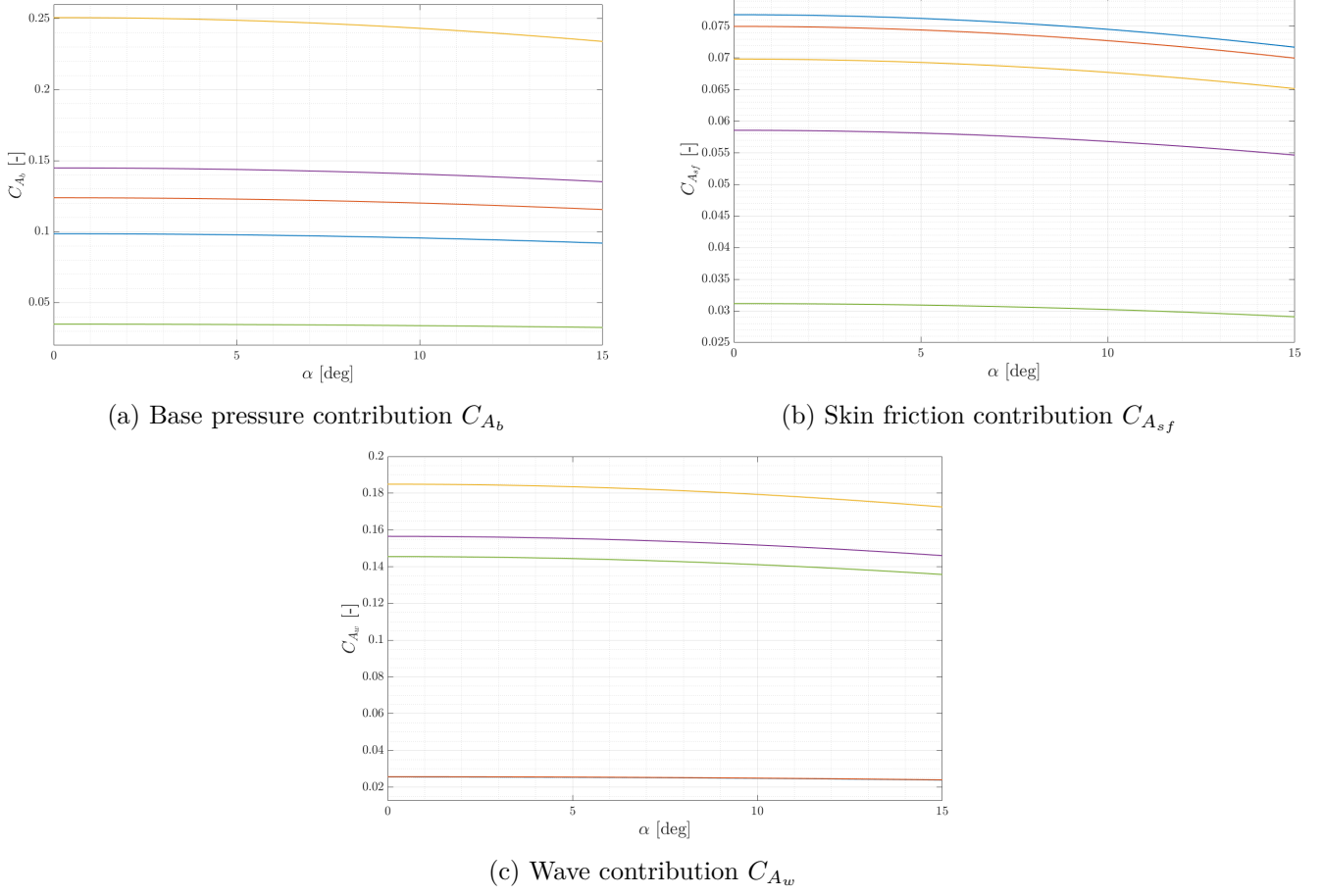


Figure 38: Axial coefficient components

N.2 Body normal force coefficient

The normal force coefficient is again computed according to Jorgensen theory [39] for the cylindrical elements of the body through Equation 43.

$$C_N = \frac{A_b}{A_{ref}} \sin(2\alpha) \cos\left(\frac{\alpha}{2}\right) \left(\frac{C_N}{C_{N_0}}\right)_{SB} + \eta C_{d_n} \frac{A_p}{A_{ref}} \sin^2(\alpha) \left(\frac{C_N}{C_{N_0}}\right)_{Newt} \quad (43)$$

A_b and A_p represent respectively the launcher base cylindrical area and planar area, α is the angle of attack. The experimental coefficients $\left(\frac{C_N}{C_{N_0}}\right)_{SB}$ and $\left(\frac{C_N}{C_{N_0}}\right)_{Newt}$ are ratios of the normal-force coefficient for the body of non-circular cross section to that for the equivalent body of circular cross section derived respectively from slender body and Newtonian theory. These are set to unity as the section of the launcher is constantly circular and the contribution of the fins will be accounted for with the component build-up approach. The cross-flow drag coefficient C_{d_n} is extrapolated from experimental data by interpolation [40] while the cross-flow drag proportionality factor η is computed as illustrated in Equations 44.

$$\eta = \begin{cases} 0.05f_b + 0.52 & \text{if } M \leq 1 \\ 1 & \text{if } M > 1 \end{cases} \quad (44)$$

The nose and shoulder skirt contributions are calculated specifically for structural sizing purposes. According to reference [6] they can be retrieved as follows in Equations 45 and 46.

$$C_N^{nose} = 2\alpha \quad (45)$$

$$C_N^{skirt} = \frac{2\alpha(d_{us}^2 - d_{ds}^2)}{d_{ref}^2} \quad (46)$$

The results are reported in Figure 39.

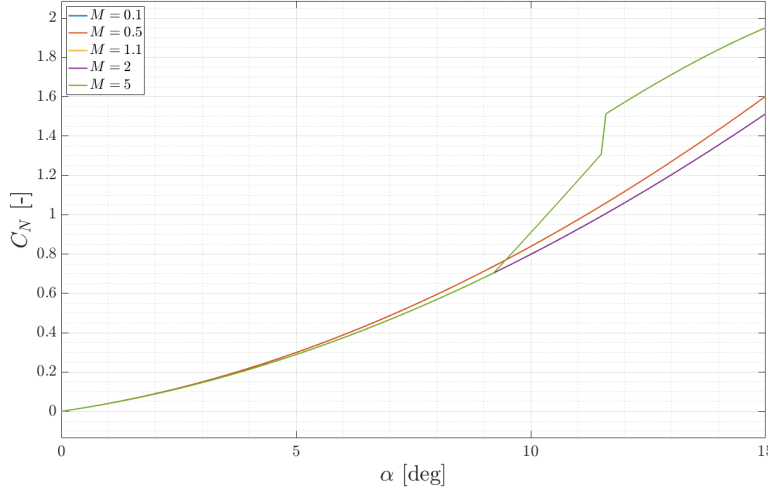


Figure 39: Normal force coefficient

N.3 Fins coefficient

The fins contribution to the overall aerodynamic coefficients is approximated according to thin airfoil theory. All the reported properties refers to one single fin unless differently specified. The normal coefficients are computed through the following Equations 47.

$$C_N^{fin} = \begin{cases} \frac{\pi}{2} \alpha AR \frac{A_{fin}}{A_{ref}} & \text{if } M \leq \left(1 + \left(\frac{8}{\pi AR}\right)^2\right)^{0.5} \\ \frac{4\alpha}{\sqrt{M^2 - 1}} \frac{A_{fin}}{A_{ref}} & \text{if } M > \left(1 + \left(\frac{8}{\pi AR}\right)^2\right)^{0.5} \end{cases} \quad (47)$$

Where AR is the aspect ratio of a couple of fins computed as the overall planar area of two fins over the wing span b , while A_{fin} is the planar surface of a single fin. Figure 40 illustrates useful fins geometrical properties that figure in previous and following relations.

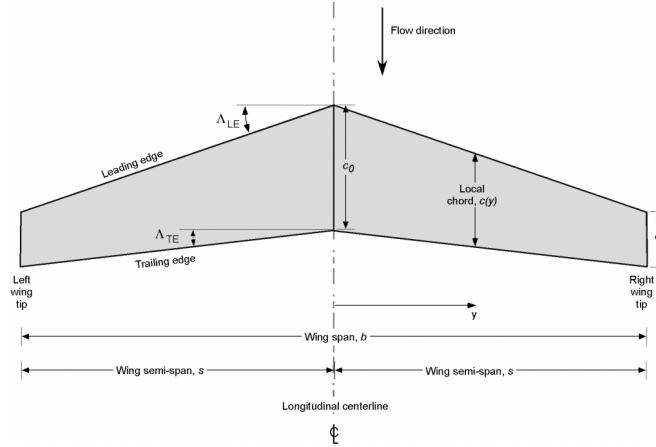


Figure 40: Wing planar section

The fins axial coefficient can be divided into two contributes: the skin friction coefficient for both subsonic and supersonic regime and the wave drag contribution to be considered when $M > 1$. The formers are illustrated respectively in Equations 48 and 49 [8].

$$C_{A_{sf}}^{fin} = 0.0133 \left(\frac{M}{q_\infty c_m} \right)^{0.2} 2 \frac{A_{fin}}{A_{ref}} \quad (48)$$

$$C_{A_w}^{fin} = \frac{1.429}{M_{LE}^2} \left[\left(1.2 M_{LE}^2 \right)^{3.5} \left(\frac{2.4}{2.8 M_{LE}^2 - 0.4} \right)^{2.5} - 1 \right] \left(\sin^2(\delta_{LE}) \cos(\Lambda_{LE}) \frac{t_{max} b}{2 A_{ref}} \right) \quad (49)$$

Where q_∞ is the free stream dynamic pressure, c_m is the mean aerodynamic chord of the fin, M_{LE} is the Mach number perpendicular to the leading edge computed as $M \cos(\Lambda_{LE})$ through leading edge sweep angle Λ_{LE} , δ_{LE} is the leading edge aperture angle, t_{max} is the airfoil maximum thickness. The overall fin axial coefficient made up of the summation of the previous mentioned is then corrected with the α variation via Equation 33 and a drag correction factor of 1.04 has been applied to account for body-fins interference [63].

An alternative model is introduced to better approximate the normal force coefficient evolution and include the effect of the airfoil shape in supersonic coefficients estimation. This improved computation methodology follows Barrowman approach both for subsonic and supersonic flows.

In subsonic conditions, the normal force coefficient of each fin is computed employing Diederich's semi-empirical method [64] according to Equations 50, 51 and 52.

$$C_{N_\alpha} = \frac{C_{N_{\alpha 0}} F_D \frac{A_{fin}}{A_{ref}} \cos(\Gamma)}{2 + F_D \sqrt{1 + \frac{4}{F_D^2}}} \quad (50)$$

$$C_{N_{\alpha 0}} = \frac{2\pi}{\beta} \quad (51)$$

$$F_D = \frac{AR}{\frac{1}{2\pi} C_{N_{\alpha 0}} \cos(\Gamma)} \quad (52)$$

where $C_{N_{\alpha 0}}$ is derived from potential flow theory with compressibility correction and F_D is Diederich's planform correlation coefficient. The axial force coefficient computation remains unchanged with respect to the initial approach as it leads to already satisfactory results (Equations 48 and 49).

Busemann's second order theory as detailed by Barrowman [44] is employed in supersonic conditions to directly compute lift and drag coefficients of the fins. According to Busemann's theory the fin is subdivided into a series of n strips along its span; for each strip the lift and drag generated are computed as sum of the contributions of each of the surfaces that compose the airfoil accounting for their orientation with respect to the free-stream as illustrated in Figure 41 through Equations 53, 54 and 55.

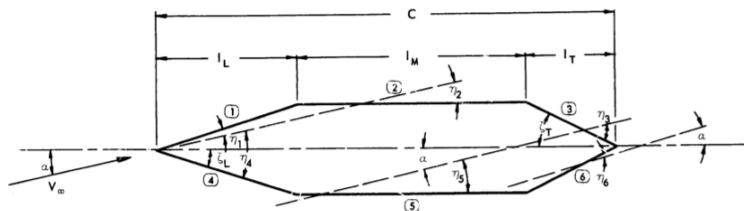


Figure 41: Fin's surfaces identification as of Reference [44]

$$C_{p_i} = K_1 \eta_i + K_2 \eta_i^2 + K_3 \eta_i^3 \quad i = 1, \dots, 6 \quad (53)$$

$$L_i = C_{p_i} q_\infty d_i \Delta y \left(1 - \frac{r_i}{2} \right) \quad (54)$$

$$D_i = C_{p_i} q_\infty n_i \Delta y \left(1 - \frac{r_i}{2} \right) \quad (55)$$

where n_i and d_i describe the geometric decomposition of each surface's length relative to the freestream flow direction. Specifically, d_i represents the portion of the surface's length that is aligned with the freestream and n_i captures the perpendicular component. The variable r_i is instead used to implement the Mach cone correction and is computed for each surface depending on the Mach cone angle μ and the intersection of each strip with the Mach cone as detailed in [44].

The contributions of each surface are then summed up to obtain the lift and drag contribution of the single strip and then the addition process is repeated along the span to compute the whole fin lift and drag coefficient as presented in Equations 56 and 57.

$$C_L^{fin} = \frac{L}{q_\infty A_{ref}} \quad (56)$$

$$C_D^{fin} = \frac{D}{q_\infty A_{ref}} \quad (57)$$

Finally, the sonic and transonic behaviour of the fins ($0.8 < M < 1.2$) is modelled separately according to shock expansion theory [65] as shown in Equations 58 and 59.

$$C_N^{fin} = \frac{2}{\pi} \alpha \cos(\Gamma) \quad (58)$$

$$C_A^{fin} = C_{A_{sf}}^{fin} \quad (59)$$

The results of this improved methodology in terms of lift coefficient are reported in Figure 16 while examples of the resulting drag coefficients are presented below in Figure 42.

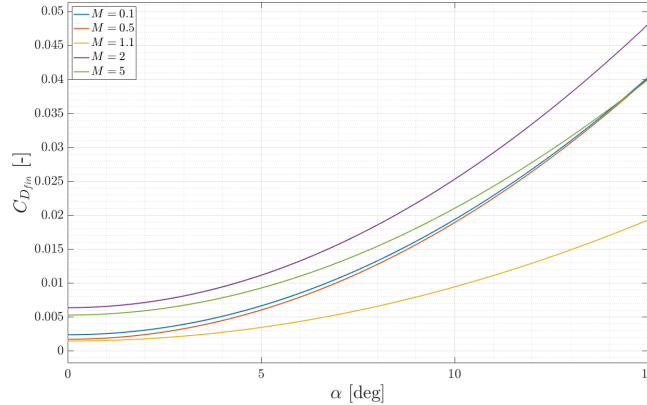


Figure 42: Fin C_D

N.4 Fins geometry

Figure 43 illustrates relevant geometrical parameters of the implemented tail fins. The measurements have to be intended in meters.

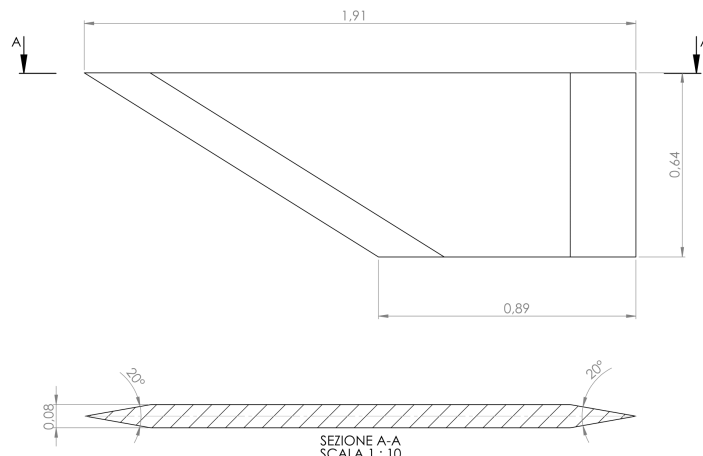


Figure 43: Tail fin geometry

O Equilibrium equations

In order to impose vertical and pitch equilibrium a 3-DOFs model has been considered. A visual illustration of forces and parameters figuring in equilibrium equations is shown in Figure 44.

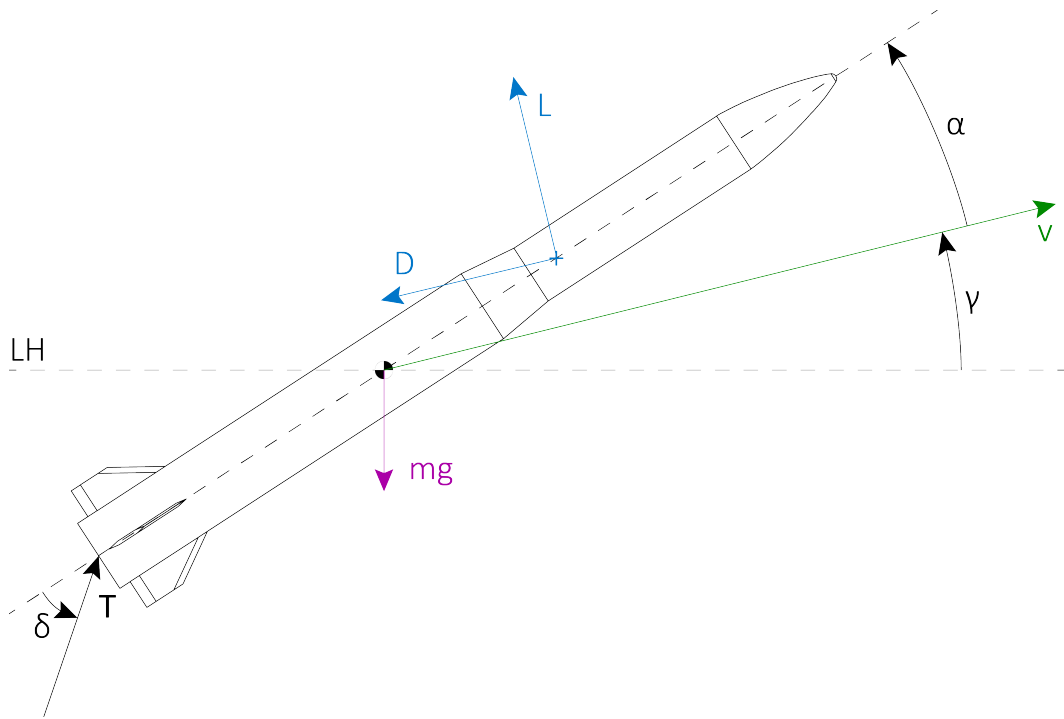


Figure 44: Launcher free-body diagram

The equations enforced to ensure the aforementioned conditions are reported in Equation 60:

$$\begin{cases} T \sin(\alpha + \gamma + \delta) - mg + qA_{ref} [C_L \cos(\gamma) - C_D \sin(\gamma)] = 0 \\ b_T T \sin(\delta) - b_{c_p} qA_{ref} [C_L \cos(\alpha) + C_D \sin(\alpha)] = 0 \end{cases} \quad (60)$$

The presented system of equations is non-linear since the aerodynamic coefficients are Mach, altitude and angle of attack dependant while the launcher mass m and the flight path angle γ refers to a specific flight condition and are plugged from optimal trajectory outputs (refer to Section 2.3).

P Thermal Analysis during the re-entry phase

The key parameters influencing thermal stresses are:

- **Altitude and Mach Number:** The study by [66] investigates a 9-engine configuration where only three aligned engines are active during retro-propulsion. Heat fluxes are evaluated at seven trajectory points with decreasing altitudes and Mach numbers (Table 32). Results indicate that at higher altitudes, the plume extends further downstream, enveloping the vehicle and causing uniform heat fluxes. As the vehicle descends, the atmospheric density increases, restricting plume spread and reducing heat flux far from the engines. At the final trajectory point, corresponding to low supersonic speeds, the plume primarily extends upstream, with the vehicle no longer enveloped in regions of high exhaust gas mass fractions. This shift explains the substantial reduction in heat flux far from the engines at trajectory point 7. Conversely, at trajectory point 1, the heat flux remains nearly uniform across the stage, as the expansive plume fully envelops the vehicle.

Point	Altitude [km]	Mach Number [-]
1	53.807	5.09
2	45.628	4.45
3	39.389	4.02
4	33.256	3.44
5	28.488	2.75
6	25.069	2.01
7	22.837	1.20

Table 32: Retro-propulsion trajectory points.

In Figure 45, the heat flux is plotted along two evaluation lines located on the rocket's surface. The first line, referred to as the *hot side*, lies on the plane that cuts through the rocket parallel to the active engine nozzles, where the heat flux is most intense. The second line, referred to as the *cold side*, is located on the plane perpendicular to the active nozzles, where the heat flux is significantly lower.

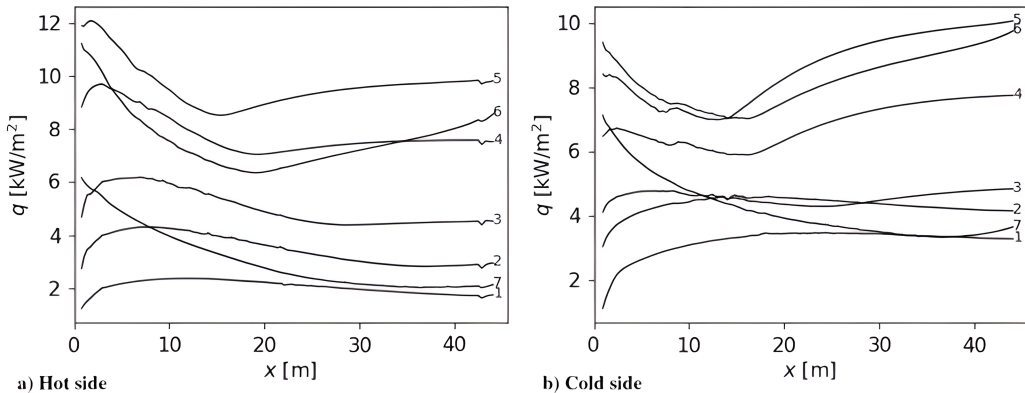


Figure 45: Heat flux at different trajectory points on two evaluation locations [66]

- **Material Properties and Wall Thickness:** Increasing the wall thickness decreases the temperature gradients, providing a higher thermal capacity (see Figure 46). Sensitivity analysis from [66] highlights that material density has the greatest influence on thermal performance, while thermal conductivity has a marginal effect due to relatively uniform heat fluxes.

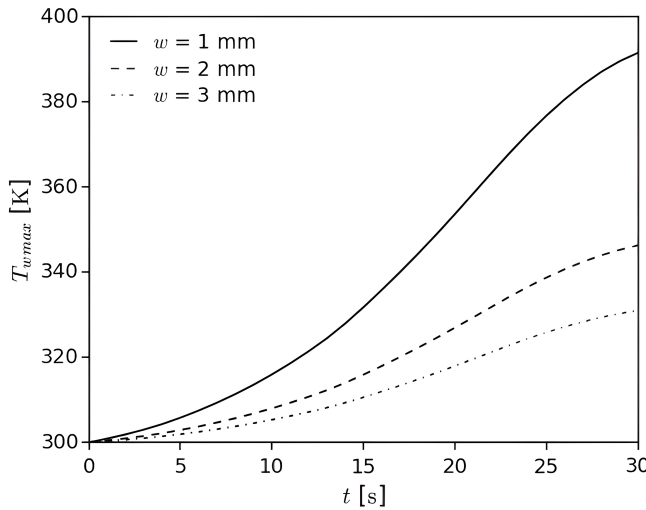


Figure 46: Change of maximum wall temperature over time for selected wall thicknesses [66]

- **Engine Configuration and Plume Dynamics:** Studies such as [67] demonstrate that nozzle configurations significantly impact heat flux distribution. Configurations with larger nozzle spacing (e.g., Mode B in Figure 47) reduce plume interactions, leading to lower peak thermal flux (171.67 kW/m^2 compared to 290 kW/m^2 of the worst configuration: Mode A). Furthermore, after-burning reactions, driven by the higher oxygen concentration in the lower atmosphere, raise the temperature in recirculation zones by 6.9–8.4%.

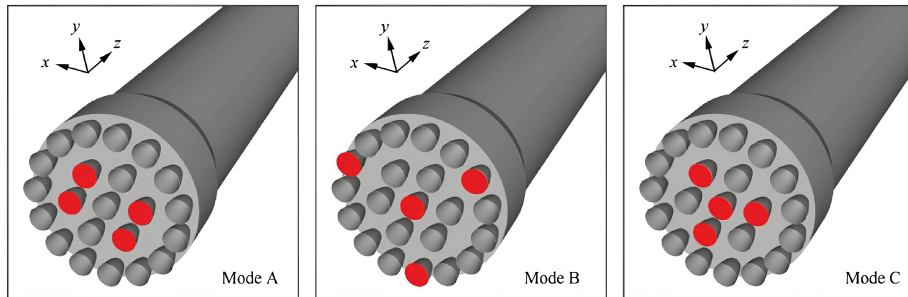


Figure 47: Three types of retro-propulsion modes [67]

References

- [1] Carlos Niederstrasser. "Small Launch Vehicles – A 2018 State of the Industry Survey". In: (2018). Email: Carlos.Niederstrasser@ngc.com, Phone: +1.703.406.5504.
- [2] Robert Tomanek and Jakub Hospodka. "Reusable Launch Space Systems". In: (). Corresponding author: Czech Technical University in Prague, Faculty of Transportation Sciences, Department of Air Transport, Horska 3, 128 03 Prague, Czech Republic. Email: tomanek@fd.cvut.cz.
- [3] Atlas Air. *767-300 BCF One-Sheet*. Accessed: 2024-12-09. 2018. URL: https://www.atlasair.com/wp-content/uploads/2018/01/767-300-BCF-One-Sheet_012418.pdf.
- [4] Shivi Kesarwani. "Polymer Composites in Aviation Sector". In: *International Journal of Engineering Research and V6* (June 2017). DOI: 10.17577/IJERTV6IS060291.
- [5] Howard D. Curtis. *Orbital Mechanics for Engineering Students*. 3rd. Oxford: Butterworth-Heinemann, 2013. ISBN: 978-0-08-097747-8.
- [6] Donald L. Edberg and Willie Costa. *Design of Rockets and Space Launch Vehicles, Second Edition*. Ed. by Joseph A. Schetz. AIAA Education Series. Reston, Virginia: American Institute of Aeronautics and Astronautics, Inc. (AIAA), 2022. ISBN: 978-1-62410-641-5.
- [7] George P. Sutton and Oscar Biblarz. *Rocket Propulsion Elements*. 10th. Hoboken, NJ: John Wiley & Sons, 2023.
- [8] Filippo Maggi. "7-Stability-Part-1". Lecture material presented at Politecnico di Milano, January, 2023. 2023.
- [9] *Pegasus User's Guide*. 8.2. Northrop Grumman Space Systems Sector. Dulles, VA, USA, 2020.
- [10] A. C. Charania et al. "LauncherOne: Virgin Galactic's Dedicated Launch Vehicle for Small Satellites". In: *30th Annual AIAA/USU Conference on Small Satellites*. Virgin Galactic. Long Beach, CA, USA, 2016.
- [11] ChemEurope. *RP-1 - Encyclopedia of Chemistry*. Accessed: 06/12/24. URL: <https://www.chemeurope.com/en/encyclopedia/RP-1.html>.
- [12] John S. Gayle and Charles H. Blakewood et al. *Preliminary Investigation of Blast Hazards of RP-1/LOX and LH₂/LOX Propellant Combinations*. Tech. rep. NASA TM-X-53240. Technical Memorandum. Huntsville, Alabama, USA: NASA George C. Marshall Space Flight Center, Apr. 1965.
- [13] Maurício Gontijo, Gustavo Alexandre Achilles Fischer, and Fernando Costa. *Characteristic Lengths of Liquid Propellant Rocket Engines and the Influence of Chemical Reactions*. Nov. 2021. DOI: 10.26678/ABCM.COBEM2021.COB2021-2105.
- [14] Dieter K. Huzel and David H. Huang. *Modern Engineering for Design of Liquid-Propellant Rocket Engines*. 370 L'Enfant Promenade, SW, Washington DC, 20024-2518, USA: American Institute of Aeronautics and Astronautics, 1992.
- [15] The Aero Blog. *The Rutherford Rocket Engine – The First Electric Rocket Engine*. <https://theaeroblog.com/the-rutherford-rocket-engine-the-first-electric-rocket-engine/>. Accessed: December 8, 2024.
- [16] NASA. *Aerothermodynamics Course*. Accessed: 2024-12-09. 2012. URL: <https://tfaws.nasa.gov/TFAWS12/Proceedings/Aerothermodynamics%20Course.pdf>.
- [17] Edward J. Hujšak. "Method and device for protecting a liquid rocket booster from impact and environmental damage to permit recovery and reuse". Pat. US4961550A. Filed: 1989-01-26; Granted: 1990-10-09. Oct. 9, 1990. URL: <https://patents.google.com/patent/US4961550A/en>.
- [18] S. A. MILLIKEN. "Feasibility of large launch vehicle recovery". In: *Journal of Spacecraft and Rockets* 2.3 (1965), pp. 311–319. DOI: 10.2514/3.28177. eprint: <https://doi.org/10.2514/3.28177>. URL: <https://doi.org/10.2514/3.28177>.

- [19] Mahendra Pratap and Swadesh Kumar. "Design and Selection Criteria of Main Parachute for Reentry Space Payload". In: *Defence Science Journal* 69 (Dec. 2019), pp. 531–537. DOI: 10.14429/dsj.69.12681.
- [20] Thomas Britting et al. "Selection Criteria for Parachutes of Student Built Rockets". In: Apr. 2022. DOI: 10.5821/conference-9788419184405.133.
- [21] Stefania Carlotti. "3-Trajectory-Part-2". Lecture material presented at Politecnico di Milano, February 15, 2024. 2024.
- [22] Northrop Grumman. *SLS Motors Fact Sheet*. 2023. URL: <https://cdn.northropgrumman.com/-/media/wp-content/uploads/SLS-Motors.pdf?v=1.0.0>.
- [23] L. M. Couch. *Drag and stability characteristics of a variety of reefed and unreefed parachute configurations at Mach 1.80 with an empirical correlation for supersonic Mach numbers*. Tech. rep. NASA-TR-R-429. Work of the U.S. Government. Public Use Permitted. NASA Langley Research Center, Hampton, VA, United States, Feb. 1975. URL: <https://ntrs.nasa.gov/citations/19750007612>.
- [24] E. K. Huckins III. *Techniques for selection and analysis of parachute deployment systems*. Tech. rep. NASA-TN-D-5619. Equations of motion for parachute deployment analysis. NASA Langley Research Center, Hampton, VA, United States, Jan. 1970. URL: <https://ntrs.nasa.gov/citations/19700005898>.
- [25] Pasquale M. Sforza. *Manned Spacecraft Design Principles*. Accessed via ProQuest Ebook Central. Elsevier Science & Technology, 2015. URL: <https://ebookcentral.proquest.com/lib/polimi/detail.action?docID=4095867>.
- [26] Casper Dek et al. "A recovery system for the key components of the first stage of a heavy launch vehicle". In: *Aerospace Science and Technology* 100 (Feb. 2020), p. 105778. DOI: 10.1016/j.ast.2020.105778.
- [27] J. Vincze. *Gemini spacecraft parachute landing system: Gemini spacecraft drogue and ringsail parachute landing system*. Tech. rep. NASA-TN-D-3496. Work of the U.S. Government. Public Use Permitted. NASA Langley Research Center, Hampton, VA, United States, July 1966. URL: <https://ntrs.nasa.gov/citations/19660020968>.
- [28] Jason Schmidt and Peter McFadden. "Reefing of Quarter Spherical Ribbon Parachutes Used in the Ares I First Stage Deceleration System". In: *20th AIAA Aerodynamic Decelerator Systems Technology Conference and Seminar*. DOI: 10.2514/6.2009-2959. eprint: <https://arc.aiaa.org/doi/pdf/10.2514/6.2009-2959>. URL: <https://arc.aiaa.org/doi/abs/10.2514/6.2009-2959>.
- [29] Grant Henson. *Materials for Launch Vehicle Structures*. Presentation. Chief Scientist. Invariant Laboratories LLC, Westlake, Ohio, 2024.
- [30] NASA. *Liquid Rocket Metal Tanks and Tank Components*. Vol. SP-8088. NASA Special Publication. Available online at: <https://ntrs.nasa.gov>. NASA, 1973.
- [31] Ltd. Showa Aircraft Industry Co. *AeroRigidTM 291A Aluminum Panel for Aircraft Interiors*. <https://showa-aircraft.co.jp>. Document # TD-003 Rev. 3. Tokyo, Japan, 2017.
- [32] R. Boyer, G. Welsch, and E. W. Collings, eds. *Materials Properties Handbook: Titanium Alloys*. Materials Park, OH: ASM International, 1994.
- [33] E.E.Gdoutos I.M.Daniel and K.A. Wan. "Failure Mode of composite sandwich beams". In: *Advanced Composites Letters Vol.11, No.3* (2002).
- [34] Davide Boiani. "Main Structural Design Consideration for Reusable Launch Vehicles". In: (2021).
- [35] David A. Di Pietro. "Techniques for Conducting Effective Concept Design and Design-to-Cost Trade Studies". In: (2015).
- [36] H. A. Crowell. "The Descriptive Geometry of Nose Cones". In: *American Journal of Physics* 33.4 (1965), pp. 271–277. DOI: 10.1119/1.1971136.

- [37] William E JR Stoney. *Transonic drag measurements of eight body-nose shapes*. Tech. rep. NACA, 1954.
- [38] L. E. Ericsson and J. P. Reding. *Prediction of static aerodynamic characteristics for slender bodies alone and with lifting surfaces to very high angles of attack*. Technical Report NASA-TM-4048. NASA Langley Research Center, 1988.
- [39] Leland H. Jorgensen. *Prediction of Static Aerodynamic Characteristics for Space-Shuttle-Like and Other Bodies at Angles of Attack from 0° to 180°*. NASA Technical Note NASA TN D-6996. Moffett Field, Calif. 94035: NASA Ames Research Center, Jan. 1973.
- [40] Leland H. Jorgensen. *A Method for Estimating Static Aerodynamic Characteristics for Slender Bodies of Circular and Noncircular Cross Section Alone and with Lifting Surfaces at Angles of Attack from 0° to 90°*. NASA Technical Note NASA TN D-7228. Moffett Field, Calif. 94035: NASA Ames Research Center, 1973.
- [41] Charles E. Rogers and David Cooper. *RASAero II Aerodynamic Analysis and Flight Simulation Program*. Version 1.0.2.0. Rogers Aeroscience. Lancaster, CA, USA, 2019. URL: <http://www.rasaero.com>.
- [42] Kishor Kumar Ukirde et al. “Aerodynamic Study of Various Fins for Missile Body”. In: *International Journal for Research in Applied Science and Engineering Technology (IJRASET) 11.XI* (2023). URL: <https://doi.org/10.22214/ijraset.2023.49235>.
- [43] Gregory L. Sloyer. *Why Should You Airfoil Your Rocket's Fins?* 2012. URL: <https://docslib.org/doc/7925467/why-should-you-airfoil-your-rockets-fins>.
- [44] James S. Barrowman. *A Computer Program for Calculating the Aerodynamic Characteristics of Fins at Supersonic Speeds*. Tech. rep. NASA TMX-721-66-162. Goddard Space Flight Center, Apr. 1966.
- [45] Piero Gili. *Appunti di Meccanica del Volo parte I*. Appunti del corso di Meccanica del Volo. Politecnico di Torino. 2023.
- [46] EASA-European Union Aviation Safety Agency. *TYPE-CERTIFICATE DATA SHEET*. 2024. URL: <https://www.easa.europa.eu/en/downloads/136365/en>.
- [47] Boeing Commercial Airplanes. *767 Airplane Characteristics for Airport Planning*. Rev I. Document Number: D6-58328, Copyright © 2023 Boeing. All Rights Reserved. Seal Beach, CA, USA: Boeing, July 2021. URL: <mailto:AirportCompatibility@boeing.com>.
- [48] Yunus A. Çengel and Afshin J. Ghajar. *Heat and Mass Transfer: Fundamentals and Applications*. 5th. McGraw-Hill Education, 2014. ISBN: 978-0-07-339818-1.
- [49] Robert J. Santoro and Sibtosh Pal. *Experimental Studies of the Heat Transfer to RBCC Rocket Nozzles for CFD Application to Design Methodologies*. Tech. rep. Propulsion Engineering Research Center and Department of Mechanical Engineering - The Pennsylvania State University - University Park - NASA, 1999.
- [50] N. P. Padture, M. Gell, and E. H. Jordan. “Thermal Barrier Coatings for Gas-Turbine Engine Applications”. In: *Science* 296.5566 (2002). DOI: [10.1126/science.1068609](https://doi.org/10.1126/science.1068609).
- [51] D. R. Clarke and C. G. Levi. “Materials design for the next generation of thermal barrier coatings”. In: *Annual Review of Materials Research* 33 (2003). DOI: <https://doi.org/10.1146/annurev.matsci.33.011403.113718>.
- [52] R. A. Miller. “Current status of thermal barrier coatings”. In: *Surface and Coatings Technology* 30.1 (1984). DOI: [https://doi.org/10.1016/0257-8972\(87\)90003-X](https://doi.org/10.1016/0257-8972(87)90003-X).
- [53] A. G. Evans, D. R. Clarke, and C. G. Levi. “The influence of oxides on the performance of advanced thermal barrier coatings”. In: *Journal of the European Ceramic Society* 28.7 (2008). DOI: <https://doi.org/10.1016/j.jeurceramsoc.2007.12.023>.
- [54] S. Bose. *High Temperature Coatings*. Elsevier, 2017.

- [55] Hirshorn Steven R., Voss Linda D., and Bromley Linda K. *NASA Systems Engineering Handbook*. NASA/SP-2016-6105 Rev2. NASA Headquarters, 2016. URL: <https://ntrs.nasa.gov/citations/20170001761>.
- [56] NASA. *Technology Readiness Level (TRL) Definitions*. https://www.nasa.gov/directorates/heo/scan/engineering/technology/technology_readiness_level. Accessed: 2024-12-08.
- [57] Air Force Space Command - Space and Missile Systems Center (SMC). *Test requirements for launch, upper-stage and space vehicles*. Accessed: 2024-12-08. 2014. URL: https://explorers.larc.nasa.gov/2019APSMEX/M0/pdf_files/SMC-S-016_05SEP2014.pdf.
- [58] Michèle Lavagna. *Space System Engineering and Operations*. Lecture material presented at Politecnico di Milano.
- [59] DLR - Deutsches Zentrum für Luft- und Raumfahrt. *Periodic Reporting for Period 2 - FALCon (Formation flight for in-Air Launcher 1st stage Capturing demonstration)*. Accessed: 2024-12-03. CORDIS - European Commission, Nov. 2022. URL: <https://cordis.europa.eu/project/id/821953/reporting>.
- [60] Martin Sippel, Sven Stappert, and Sunayna Singh. *In-Air-Capturing Development Roadmap (Update)*. Research and Innovation Action Deliverable. Deliverable Reference Number: D2.4, Issue 2, Revision 0. FALCon Project - EC H2020, Jan. 2023. URL: <https://elib.dlr.de/194602/>.
- [61] Rocket Lab. *Reusable Rockets*. URL: <https://www.rocketlabusa.com/launch/reusable-rockets/>.
- [62] S. Niskanen. “Development of an Open Source model rocket simulation software”. <http://openrocket.sourceforge.net/documentation.html>. MA thesis. Helsinki University of Technology, 2009.
- [63] G. Governale et al. “A trade-off methodology for micro-launchers”. In: *Aerospace Systems* 4 (2021), pp. 209–226. DOI: [10.1007/s42401-021-00095-w](https://doi.org/10.1007/s42401-021-00095-w).
- [64] Franklin W. Diederich. *A Plan-Form Parameter for Correlating Certain Aerodynamic Characteristics of Swept Wings*. Tech. rep. NACA-TN-2335. Technical Note. National Advisory Committee for Aeronautics (NACA), 1951.
- [65] John D. Anderson. *Modern Compressible Flow: With Historical Perspective*. 3rd. New York: McGraw-Hill, 2000.
- [66] Tobias Ecker et al. “Numerical Study on the Thermal Loads During a Supersonic Rocket Retro-propulsion Maneuver”. In: *Journal of Spacecraft and Rockets* 57.1 (2020), pp. 131–146. DOI: [10.2514/1.A34486](https://doi.org/10.2514/1.A34486). URL: <https://doi.org/10.2514/1.A34486>.
- [67] Yifei SU et al. “Re-entry rocket basic flow characteristics and thermal environment of different retro-propulsion modes”. In: *Chinese Journal of Aeronautics* 37.7 (2024). ISSN: 1000-9361. DOI: <https://doi.org/10.1016/j.cja.2024.05.001>. URL: <https://www.sciencedirect.com/science/article/pii/S1000936124001614>.